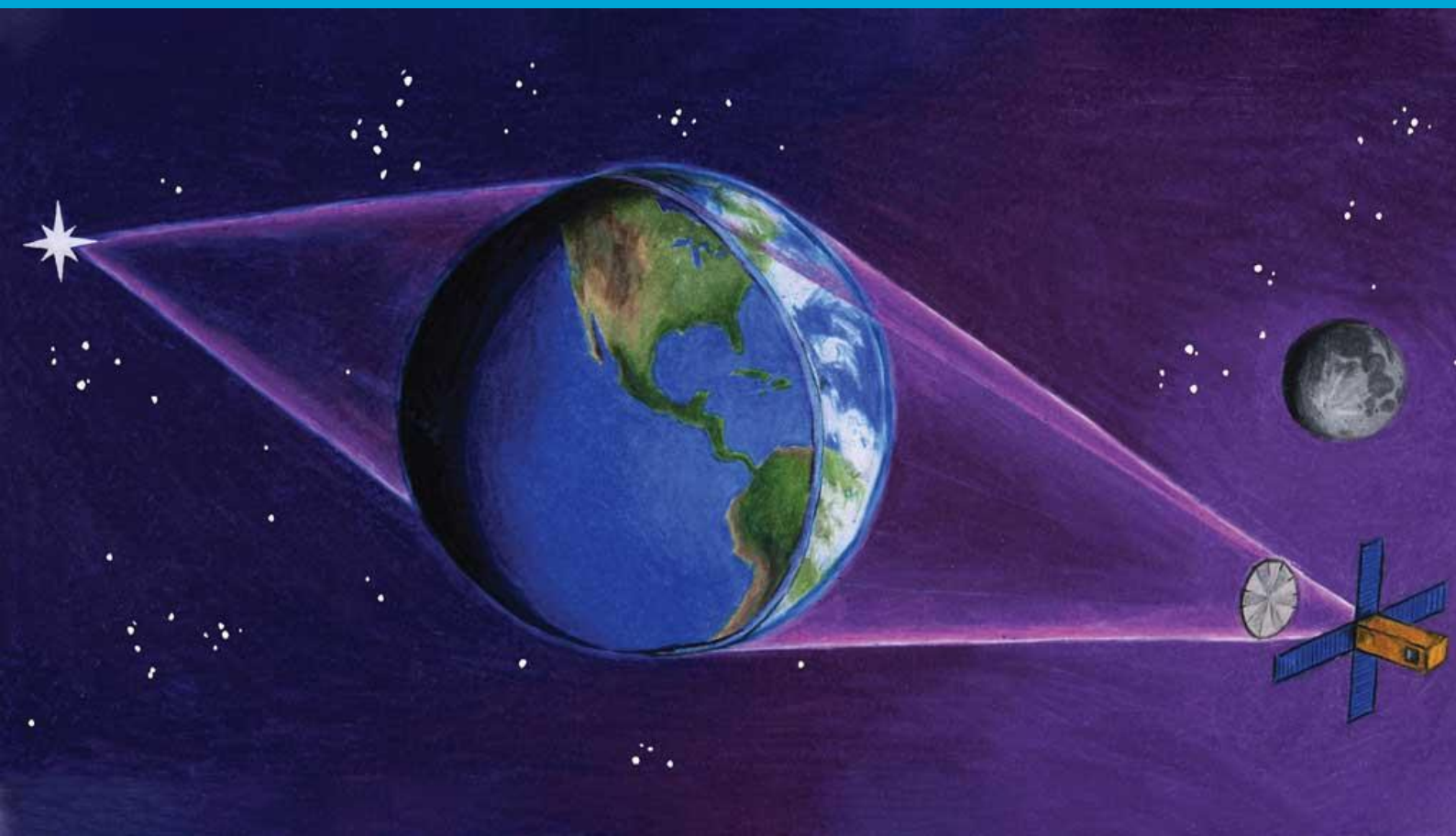


The Terrascope: Earth's Atmosphere as a Telescopic Lens

S. E. Alpert



The Terrascope:

Earth's Atmosphere as a Telescopic Lens

by

S. E. Alpert

to obtain the degree of Master of Science
at the Delft University of Technology,
to be defended publicly on Monday August 31, 2020 at 15:00.

Student number: 4939964
Project duration: November 11, 2019 – August 24, 2020
Review committee: Dr. P. M. Visser, TU Delft, supervisor
Dr. D. M. Stam, TU Delft, supervisor
Prof. dr. ir. C. Vuik, TU Delft

An electronic version of this thesis is available at <http://repository.tudelft.nl/>.

Acknowledgements

This thesis has somehow become the largest work that I have ever put together, from time invested to words written. When I include the words from this report and as well as those in my various codes (which are absent from the report, but available should you want to wade through them), it definitely surpasses all, which I suppose a good Master's thesis should. This huge work (of science and art) would not have been possible without a number of people.

Unexpectedly, I find myself thankful year after year to my high school calculus teacher, Ms. Joseph. It was in her class that I fell in love with mathematics, and her "push yourself as hard as you can" attitude and indispensable calculus notes are both with me to this day. I would not be here today had I not spent a summer doing heliophysics research in Huntsville. Sanjiv, Ron, Amy, Sabrina, and Samaiyah always treated my ideas as equal to those of any professional scientist. With their respect and encouragement, I learned that not only did I enjoy scientific research, but that I was great at it. I am indebted to Kees Vuik, who decided to take an hour-long meeting with a random student interested in the COSSE program, and by doing so, completely changed my life. Thank you to David Kipping, without whom this work would literally not be possible. He also took a chance meeting with a student and renewed my ideals about scientific collaboration. Paul and Daphne, my thesis supervisors, were a wonderfully balanced advising pair. Together, they were the right mixture of tough and motivating, detail and big picture oriented, work hard and take-a-break. We spent countless hours discussing the project, both in theory and the nitty-gritty code. They both truly cared about the research and my success, and I am very lucky to have worked with them.

On a more personal level, there's people I'd like to acknowledge. To Michael, I appreciate our ongoing help with each other's academic decisions and applications— it keeps my head on straight. In dire circumstances, I remember your line, "keep your head down, keep working". My COSSE posse, I would not have reached this point without your support; I am forever grateful that we all ended up together. To Anni and Camera, you kept me laughing and you kept me sane. My family, despite having little idea of what I'm doing, have enthusiastically supported me every step of the way. And Ben, you also began with very little understanding of my thesis, but learned it all through countless hours of reading, listening, and asking questions. You reminded me of my progress and successes when I doubted myself; you asked about my goals and congratulated me when I met them; you asked questions to make sure I knew what I was talking about; you pointed out and encouraged my strange working hours; you were understanding and helpful when all I had time to do was work; you listened to and constructively critiqued my presentations; you helped us move across a country when all I

could think about was this thesis. Your constant and unwavering support (as well as the coffee you made every morning in the last days) fueled me through all of this.

Lastly, I will do something perhaps unconventional, but which people who know me will understand. I acknowledge myself. I acknowledge that I am a smart and capable scientist who deserves the success for which I have worked hard. This thesis is a testament to that.

Shane

Contents

List of Figures	vii
1 Introduction	3
1.1 Telescopes: Their Purpose and Limits to Current Approaches	3
1.2 Kipping's Terrascope	5
1.3 Central Flash	7
1.4 Research Questions	8
1.5 Methodology	8
2 This Terrascope	9
2.1 Ray Tracing	9
2.1.1 Refraction	10
2.1.2 Gradient-Index Optics	13
2.1.3 Equations of Motion	16
2.2 Types of Codes	21
2.2.1 Single Ray	22
2.2.2 Angle Array	22
2.2.3 Thin Ring	26
2.3 Model Outputs	27
3 Atmospheric Effects	29
3.1 Earth's Atmosphere	30
3.2 Turbulence	34
3.2.1 Theory	34
3.2.2 Implementation	38
3.2.3 Results	40
3.3 Rayleigh Scattering	44
3.3.1 Theory	44
3.3.2 Implementation	46
3.3.3 Results	48
3.4 Absorption	52
3.4.1 Theory	52
3.4.2 Implementation	54
3.4.3 Results	59

3.5	Transmittance	63
3.6	Combining Effects: Point Spread Function	67
3.6.1	Theory	67
3.6.2	Implementation	68
3.6.3	Results	71
4	Discussion	77
4.1	Amplification	77
4.2	Comparison to Kipping's Work.	78
4.3	Errors	78
5	Conclusion	81
5.1	Research Answers	81
5.2	Astronomical Uses.	82
5.3	Future Work	83
	Bibliography	85
A	Appendix	91

List of Figures

1.1	A protoplanetary disk, the disk of gas and dust in which planets are formed, is imaged two years apart, with the later image in higher angular resolution. Taken by the ALMA (Atacama Large Millimeter Array) radio telescope, from 2016 and 2018 [27],[1].	4
1.2	Determining the magnification of a Galilean telescope in a drawing by Sir William Herschel. Light enters from the left and the eye-glass is on the right. Segment AB is the aperture, OQ is the focal length of the telescope, and EQ is the focal length of the eye-glass [23]	4
1.3	Diagram of the light rays inside a Newtonian reflecting telescope [31].	5
1.4	Diagram of the light rays inside a Cassegrain reflecting telescope [31].	5
1.5	Diagram of the Terrascope, with parallel light rays from the celestial object entering the Earth's atmosphere from the left, passing through, being focused by a lens, and ending at the detector. The top of the atmosphere is outlined in dashed lines to show its resemblance to a lens, such as the secondary lens. This secondary lens is not necessary for the Terrascope to function, but is shown here to highlight the similar shapes of the atmosphere and a lens. Figure not to scale.	6
2.1	Geometry of the Terrascope, not to scale. Green is the boundary of the Earth's surface, blue is the boundary of the atmosphere, and red are the same rays of light from an astronomical object. The incoming rays are always assumed to be parallel. The y-direction is vertical and the x-direction (not shown) points out of the plane of the page. In reality and in the model, the Earth and the atmosphere around it are spherical. The z-direction is the direction of light propagation. Rays are propagated from the detector on the left, which is situated at a position of $z=-L$. R is the radius of the Earth and $10H$ is the height of the atmosphere, where H is the atmospheric scale height. r is the position of the ray and r/L is the angle at which it enters the detector, in the small angle approximation.	10
2.2	The rectangular box structure represents an enclosed medium, through which a light ray is passing. The line perpendicular to the surface is called the "normal", and it is with respect to this line that the angles of incidence and refraction, θ_i and θ_r , respectively, are measured [17].	10
2.3	Setting sunlight enters the atmosphere at a higher altitude in order to avoid the slowing effects of the thicker atmosphere at lower altitudes. The resulting bent light makes it appear as if the Sun is higher in the sky than its true position below the horizon [17].	11

- 2.4 Cassini's model of atmospheric refraction. The bolder arc is the surface of the Earth and the thinner arc is the atmosphere. C is the center of the Earth, R is the radius of the Earth, O is the observer, P is where the light ray from the star enters the atmosphere, h is the height above the surface where the ray enters, and r is the ray itself. Line segment CP is the normal to the surface and atmosphere boundary. The light ray enters the atmosphere at an angle z_2 to the normal, but exits and is viewed by the observer at angle z_1 . Note that $z_1 < z_2$ because the atmosphere is denser than the vacuum of space [52]. 12
- 2.5 Similar to Figure (2.4, but with two atmospheric layers, although more are necessary to closely approximate the gradual change in atmosphere with increasing altitude. Here, O is the center of the Earth, a is the radius of the Earth, P_e is the observer, P_n is where the light ray from the star enters the atmosphere, P_{n+1} is another atmospheric shell, r_n is the height above the surface where the ray enters, and r_{n+1} is the height of the other atmospheric shell. The light ray enters the atmosphere at angle i_n , bends to e_n , enters the next shell at i_{n+1} , bends to $Z_0 - Z$ [32]. 13
- 2.6 Terrascope coordinate system showing the velocity vectors. The origin is the center of the Earth, so the starting values at the detector are negative. The red line shows a single light ray emanating from the detector and travelling towards the Earth's atmosphere. In reality, the light travels from celestial object, through Earth's atmosphere, towards the detector, but our model runs simulations in the opposite direction. A light ray is uniquely defined by its starting angle at the detector. This angle is in turn defined by its x and y components, the v_1 and v_2 values, respectively. Figures (2.7a) and (2.7b) show these components. 19
- 2.7 The x and y components of a light ray angle. 21
- 2.8 How the paths of light rays vary when traveling to detectors at different distances from the Earth. The detector is on the left; the celestial object is on the right. Green is the surface, blue is the atmosphere top, and the shades of gray represent the different distances. The farther the detector, the higher the minimum altitude that the ray reaches, or in other words, the less deep the light penetrates. Although our calculations are different from Kipping's, the results of the light rays' minimum altitude are approximately the same. For a ray of $L = 1.5 \times 10^9$ m, Kipping's Terrascope calculated the minimum altitude to be 13.7km; our Terrascope calculated 13.8km. 23
- 2.9 The angle that light bends while traveling through the atmosphere depends upon the minimum height—or depth—that it reaches. A ray which passes through lower layers of the atmosphere has a larger bending angle than a ray that remains closer to the top. This plot is shown for $L = 1.5 \times 10^9$ m. 24

- 2.10 Three dimensional diagram of the maximum and minimum angles created for the angle array Terrascope. The green and blue lines represent the Earth's surface and atmosphere, respectively. The solid red lines are light rays in the y-plane hitting the outer edge of the atmosphere in each direction (the maximum and minimum values). The dashed red lines are light rays in the x-plane doing the same. L is the adjacent length to all of the angles emanating from the detector at left. Thus, using a small angle approximation, the maximum and minimum angle in both planes is $\frac{R+10H}{L}$ and $\frac{-(R+10H)}{L}$, respectively. The angle values, α_1 for the x-plane and α_2 for the y-plane, are components of the total angle which emanates from (or, in real life, enters into) the detector. The angles between detector and Earth make a cone shape. 24
- 2.11 Shows the angular limits which compose the check performed on each light ray before it is propagated. The green solid line is the Earth's surface; green dash-dot is the triangle which defines the angle at which the light ray hits the surface. The blue solid line is the Earth's atmosphere; blue dash-dot-dot is the triangle which defines the angle at which the light ray just intercepts the atmosphere. 25
- 2.12 Graph of a Boolean matrix showing where the light rays successfully pass through the atmosphere and into the detector. If a ray never enters the atmosphere or hits the Earth, it's value is set to 0, and thus it does not appear on this plot. The resulting ring shape is due to the atmosphere's spherical shell shape. The grid is 1000-by-1000 because there are 1000 rays propagated in each direction, resulting in a total of 1,000,000 rays in the grid. Not all of them pass through the atmosphere— in this case, 20,220, or 2.02%. 25
- 2.13 Four pieces of the thin ring code corresponding to Equations (2.54), (2.55), (2.56), and (2.57). Again, green denotes the Earth's surface and blue denotes the top of the atmosphere, not to scale. The expressions on the right describe the α_2 part of the aforementioned equations; note that they are rearranged versions of the inner (green) and outer (blue) circles. Inner: $\alpha_{min}^2 = \sqrt{\alpha_1^2 + \alpha_2^2}$. Outer: $\alpha_{max}^2 = \sqrt{\alpha_1^2 + \alpha_2^2}$ 27
- 3.1 Relationship between altitude, temperature, and pressure. Density scales as pressure. Pressure units shown are millibars; one bar is defined as the pressure at sea-level. [42]. 30
- 3.2 Different types of clouds, their altitudes, and the temperature at that altitude [30]. Clouds at higher altitudes are made of ice crystals, whereas clouds at lower altitudes are made of liquid water droplets. The transparency of the cloud reveals how full of moisture it is; the more transparent, the less moisture. In particular, cirrostratus, altostratus, stratocumulus, and nimbostratus hold large amounts of moisture. 33

3.3 Undisturbed, or laminar, flow comes off the ocean and becomes turbulent once it encounters the mountain. To decrease seeing, observatories are placed not only on high altitudes (in order to look through less atmosphere), but on the first mountain ridge near the ocean (in order to get the undisturbed ocean winds) [36]. 35

3.4 From the largest scale eddy, $L_0 \sim 10\text{m}$, down to the smallest, $l_0 \sim 1\text{mm}$ [35]. . 35

3.5 Profile of a refractive index structure constant. This model is called Clear I Night, so-called because it was based on measurements taken in the desert night of New Mexico in 1993. We used the nighttime measurements because the detector would only detect light from the night side of the Earth; the day side has too much bounced light from the Sun. The model measurements were "made under fairly homogeneous meteorological conditions" [2]. These measurements and their corresponding model, compared to the other models made by the creator of Clear I Night, have more turbulence in the lower part of the atmosphere, specifically below 10km. As stated in the text, we implemented our Terrascope with elements that would be the most disruptive to test its abilities in the worst-case, yet still realistic, scenarios. 39

3.6 Plot of coherence length versus the lowest height that each light ray reaches in the atmosphere, for nine different wavelengths. This graph was made using the 'Angle Array' code. The lower the ray reaches in the atmosphere, the shorter the coherence length. This is because there is more turbulence in the lower atmosphere, as shown in Figure (3.5). Thus, when light reaches lower levels, it goes through more areas where it is bent due to the constantly changing indices of refraction. It is also because rays which reach lower in the atmosphere have a longer path through the atmosphere, so the light travels through a higher amount of turbulent air. This is shown in Figure (2.8). Additionally, for longer wavelengths, there is a weaker proportional relationship between minimum altitude and coherence length. For example, the 1000nm light rays have a longer coherence length at a lower minimum altitude than the light rays at 200nm. This relationship can be seen in Equations (3.14) and (3.12), where coherence length is proportional to wavelength. As the wavelength increases, so does the coherence length. 41

3.7 Plot of coherence length versus the distance from Earth's center to the detector, L , for nine different wavelengths. This graph was made using the 'Single Ray' code. The minimum value is the distance to the Moon and the maximum is one Hill radius. This is a stationary location between the gravitational pulls of the Sun, Earth and the Moon. This figure is consistent with Figure (3.6) because, as seen in Figures (2.8), (A.1) and (A.2), the smaller the L , the lower the minimum altitude. Thus, the same behavior observed for coherence length vs. minimum altitude would be observed for coherence length vs. L . The larger the L , the larger the coherence length, and thus the image of the celestial object behind the Earth will be higher resolution. 42

- 3.8 Plot of coherence length versus light wavelength, for five different L values. This graph was made using the 'Single Ray' code. It contains the same information as Figure (3.7), but is shown in a different way. Figure (3.7) is useful for continuous detailed behavior of coherence length as a function of L ; this one has the same usefulness as a function of λ . Following the trend lines on this graph, if we were to use even higher wavelengths, the coherence length would continue to increase. 43
- 3.9 Plot of scattering cross section versus light wavelength, shown for three different gasses and their combined effect. The higher the cross section, the more likely light will scatter off of the molecule. Shorter wavelengths of light have higher cross sections because their periods are shorter and therefore more likely to collide with a particle. This relationship is seen in Equation (3.23). N_2 and O_2 have larger cross sections than Ar because they are made of two atoms as opposed to one. The combined effect, which is made up of the other three, is mostly dominated by N_2 . The broken lines are where we used a function to estimate the wavelength ranges not covered by the literature we used. 47
- 3.10 Plot of survival probability after scattering versus the lowest height that each light ray reaches in the atmosphere, for nine different wavelengths. Graph was made using the 'Angle Array' code. The results are consistent with the pattern shown in Table (3.2), that the higher the altitude, the fewer the particles in the atmosphere. It follows that a light ray which passes through a higher minimum altitude collides with fewer particles and therefore has a higher chance of surviving its path through the atmosphere towards the detector. The relationship with respect to wavelength is consistent with that seen in the coherence length graphs; the longer the wavelength, the less likely the light ray is to scatter off a particle and the higher it's survival probability. The points in the top right of the graph are numerical artifacts due to the light rays reaching close to the artificially imposed atmosphere at $10H \sim 80\text{km}$ 49
- 3.11 Plot of survival probability after scattering versus the distance from Earth's center to the detector, L , for nine different wavelengths. This graph was made using the 'Single Ray' code. Recall how the coherence length graphs, Figures (3.7) and (3.6), are related. A smaller minimum altitude corresponds to a shorter coherence length, and since a smaller L has a smaller minimum altitude, a smaller L also corresponds to a shorter coherence length. The same is relationship is true of Figure (3.10) and this graph. A smaller minimum altitude means a lower chance of survival after scattering, and since a smaller L has a smaller minimum altitude, a smaller L also means a lower chance of survival after scattering. 50

- 3.12 Plot of survival probability after scattering versus light wavelength, for five different L values. This graph was made using the 'Single Ray' code. It better illustrates the lack of surviving rays below 400nm than Figure (3.11). The larger L and wavelength values have a higher probability of reaching the detector, similar to the trend in the coherence length plots. It appears that for larger L and wavelength, the quality of our Terrascope improves. The dip at 550nm is due to the change in O_2 scattering cross-section function seen as the broken line in Figure (3.9). 51
- 3.13 Absorption spectrum for the Earth's entire atmosphere. Gamma rays, X-rays, UV rays, mid-IR, far-IR, and long radio waves are all blocked out in the upper atmosphere. Nitrogen gas, for example, is responsible for much of the UV absorption in the 80-100nm range [47]. There is a "window" where visible and near-IR light get through and are observed from Earth: see Figure (3.14) [44] . 52
- 3.14 Absorption spectra for gases found in Earth's atmosphere, with a focus on the near-IR part of the electromagnetic spectrum. The vertical axis indicates percentage of radiation absorbed [8]. 53
- 3.15 How temperature varies with altitude, modeled using Equation (3.41). As mentioned in the beginning of Chapter 3, the ozone layer (consisting of O_3 molecules) absorbs UV light and heats up the atmosphere. This causes the temperature to increase with increasing altitude, rather than decrease with increasing altitude. This change in the function's direction is seen in the graph around 25km. . . . 55
- 3.16 Plot of O_3 absorption cross section table values versus wavelength. Each cross section is based on the wavelength of light and temperature of the system. The variation with wavelength is based on the structure of the molecule. The overall trend in this wavelength range of increasing cross section with increasing temperature means that at higher temperatures, light rays are more likely to collide with an O_3 molecule. This is due to Doppler broadening. Around 400nm and 1000-1100nm, note the widened absorption in the higher temperatures; this is an example of such broadening. 56
- 3.17 Similar to Figure (3.16), this is a plot of O_3 absorption cross section table values. However, in this figure, temperature is the horizontal axis and the wavelength is parameterized. This plot confirms that the higher wavelengths have a larger cross section. It also shows that the temperature variation is not large, but is slightly more significant for 1000nm and 400nm. Note that these two lines are the lowest cross section, and are the dips seen in Figure (3.16). 57
- 3.18 Similar to Figure (3.17), but using the altitude values in Equation (3.41) in place of the temperature. This gives a visual of how the cross sections vary with different variables. The variation is small over the atmosphere and more pronounced for different wavelengths. 58

- 3.19 Plot of survival probability after absorption versus the lowest height that each light ray reaches in the atmosphere, for nine different wavelengths. This graph was made using the 'Angle Array' code. Note that a dip occurs in most wavelengths around 20km, as dictated by Equation (3.40). This is due to the high concentration of O₃ in the Ozone layer around that altitude. The change in temperature function– the inflection point– seen in Figure (3.15) occurs at a higher altitude because it takes a sufficient amount of O₃ molecules before the behavior of the system changes. Note how, unlike for scattering survival probability, the curves for different wavelengths are not in order. That is, 600nm light (yellow) has a higher overall survival probability than 300nm light (magenta), but lower probability than 500nm light (green). This is because 600nm light has a lower absorption cross section than 300nm light, but a higher absorption cross section than 500nm light. The lower the absorption cross section, the higher the probability of survival. Following the trend of cross section dictating the wavelength order, the 400nm light (purple) can be seen near the top, just below that 1000nm light (black). 60
- 3.20 Plot of survival probability due to absorption versus the distance from Earth's center to the detector, L , for nine different wavelengths. This graph was made using the 'Single Ray' code. Similar to the corresponding scattering survival probability graph, Figure (3.11), below a certain wavelength threshold, all light is absorbed for any values of L we modeled. For scattering this is at 400nm, for absorption it is 300nm. For absorption, the 400nm light has the highest survival probability along with 1000nm light. Both of these lines are at the top of the graph. Overall, the survival probability after absorption is higher than after scattering, indicating that scattering is the stronger affect in our Terrascope scenario. 61
- 3.21 Plot of survival probability after absorption versus light wavelength, for five different L values. This graph was made using the 'Single Ray' code. It has the opposite x -axis and parameterization as Figure (3.20) to better show the detailed dependence of absorption survival probability on wavelength. In this graph, the "out of order" wavelengths in Figures (3.19) and (3.20) are seen as a dip at 600nm. The parameterized black lines also confirm what was seen in the above graph, namely, that the larger L values correspond to a lower survival probability. The wavy lines throughout are due to the absorption cross section fluctuations with temperature (and therefore with altitude and L), originally seen in Figure (3.16). 62

3.22 Plot of total transmittance versus the lowest height that each light ray reaches in the atmosphere, for nine different wavelengths. Graph was made using the 'Angle Array' code. Combining the graphs of scattering and absorption yields the line shape of former and the Ozone layer dips of the later. The 600nm (yellow) line drops the most around 22km because it begins to be strongly absorbed at that altitude. Overall, the longer wavelengths appear to transmit the most light into the detector. 64

3.23 Plot of survival probability after absorption versus the distance from Earth's center to the detector, L , for nine different wavelengths. This graph was made using the 'Single Ray' code. Here, the 600nm (yellow) line crosses the 500nm (green) line at around $L = 1.17 \times 10^9$ m. This corresponds to the minimum height where they crossed in Figure (3.22), 11km. The 600nm line will cross the 400nm (purple) line for around $L = 4.3 \times 10^9$ m. 65

3.24 Plot of total transmittance versus light wavelength, for five different L values. Graph was made using the 'Single Ray' code. As before, the general shape mirrors that of the corresponding scattering survival probability plot, but with added Ozone layer dips and wavy lines due to absorption cross section temperature fluctuations. 66

3.25 Our Terrascope set-up showing the relationship between aperture, a , and pixel size, $\frac{2\alpha_{\text{peak}}}{M}$, through the angle δ . Green and blue circles show the Earth's surface and atmosphere, respectively. Light red and dark red lines show on- and off- axis light rays, respectively. By drawing how the light shifts by δ on each side, we can calculate how the size of the detector and the size of a resolved pixel are related. From this, we estimate an effective aperture size of our Terrascope. 69

3.26 Eight different combinations of effects showing their influence on the PSF for $\lambda = 10^{-6}\text{m} = 1000\text{nm}$. Of all the wavelengths we tested in our simulations, 1000nm has the highest probability of survival and longest coherence length; hence, it is expected to also have the highest amplification after the light is subjected to all three atmospheric effects. Without effects, the amplification is approximately 35; with all affects, the amplification is approximately 10. 72

3.27 Eight different combinations of effects showing their influence on the PSF for $\lambda = 6 \times 10^{-7}\text{m} = 600\text{nm}$. Of note in these plots is that the amplification after scattering is higher than the amplification after absorption. This was predicted by the survival probability plots in which 600nm light had a higher chance of survival after scattering than absorption (for $L = 1.5 \times 10^9\text{m}$). Similar to the plots of 1000nm, when 600nm light is subjected to none of the effects, the amplification is 30. However, unlike the 1000nm plots, when 600nm light is subjected to all three effects, the amplification is effectively zero. 73

- 3.28 These are plots of the PSF for different combinations of effects for varying wavelengths. On the left are the PSFs without turbulence; on the right are those with turbulence. Note how on the right, the peaks are both much lower and wider. The widening effect is due to light being spread out. This spread also causes a lower peak height. Turbulence causes the greatest decrease in intensity, followed by scattering and then absorption. For scattering and absorption, this change in intensity depends heavily on the wavelength, but for turbulence, it does not. 74
- A.1 Graph of minimum height that a light ray travels versus the L value of that light ray. This range is the one used for all of the simulations in our research. As shown and referenced throughout this report, there is a proportional relationship between the two variables, but it is not linear. 92
- A.2 Graph of minimum height that a light ray travels versus the L value of that light ray, shown for a \log_{10} x -axis. The linear trend of this graph shows that there is a semi-log relationship between the variables h_0 and L . To reach higher values of h_0 takes much larger values of L . For example, rays with $h_0 = 80\text{km}$ correspond to $L = 10^{12}$ while rays with $h_0 = 90\text{km}$ correspond to $L = 10^{13}$ 92

Abstract

This research contains the design, modeling, and analysis of the Terrascope. This apparatus intends to use the Earth's atmosphere as a lens to bend light rays from celestial objects and focus them into a detector placed at a distance from the Earth, for example, the Moon. We develop an independent model from that of David Kipping, on whose Terrascope research this work is based. Our Terrascope model uses gradient-index optics to calculate the light bending through the Earth's atmosphere. We also model three different atmospheric effects which modify the light passing through the atmosphere: turbulence, Rayleigh scattering, and ozone absorption. Our results show that turbulence has the largest impact on the light, and, consequently, on the functioning of our Terrascope. It causes the light to spread out, decreasing the image resolution and amplification. Without atmospheric effects, our model simulations predict a maximum amplification of about 55,000, the same results as Kipping. This occurs when using a 1m detector aperture, 1.5×10^9 m detector distance, and 1000nm wavelength light. Using the same parameters, when scattering and absorption are considered, the amplification decreases by 14%. When turbulence is considered, the amplification decreases by 99.98% to a total of 10. This is much lower than Kipping's prediction of 22,500. We conclude that turbulence is the most important aspect of the Terrascope to consider in any future work. The Terrascope continues to be interesting concept for study and may have promise for observing celestial objects if a farther detector distance, longer light wavelength, and different atmosphere are considered.

1

Introduction

1.1. Telescopes: Their Purpose and Limits to Current Approaches

Since people first pointed the telescope to the sky in the 17th century, they have been making increasingly advanced instruments with which to observe celestial objects [22]. The first "spyglass" is credited to Hans Lippershey in 1608, but it is Galileo Galilei who first used the lensing properties of glass to observe outer space. Of chief importance when considering new devices are the telescopes' ability to amplify (increase light collection), resolve (distinguish different parts of the object), and magnify (make the object appear bigger compared to the naked eye). Amplification is measured as the ratio of light intensity observed when using the telescope to the light intensity without the telescope. The observed intensity depends on the number of photons (light) received, which in turn depends on the telescope's light receiving area. Of course, area is determined by diameter (the aperture). A telescope's angular resolution is proportional to the inverse of the aperture [28]. The concept of angular resolution is illustrated in Figure (1.1). Lastly, the magnification is equal to the ratio of the focal length of the telescope to the focal length of the eye-piece. The focal length of a lens depends on the material of the lens and its surroundings as well as the radius of curvature of the lens. An illustration of this is seen in Figure (1.2), where the aperture is AB and the magnification is $\frac{OQ}{EQ}$ [23].

The first type of telescope was called a "refracting telescope" (see again Figure (1.2), due to its ability to refract (bend) light rays which passed through it. Many improvements were then made upon these refractors, including: switching from spherical to hyperbolic lenses to focus rays at a single point; using achromatic lenses to avoid wavelength-dependent light splitting; and developing the tubeless aerial telescope to prevent long telescopes from collapsing in the wind [50]. The size of a refractor is inherently important, since we desire a large aperture and long focal length. However, in the late 19th century, the size of the glass lens became a limiting factor for producing more powerful telescopes. Making, polishing, and supporting ex-

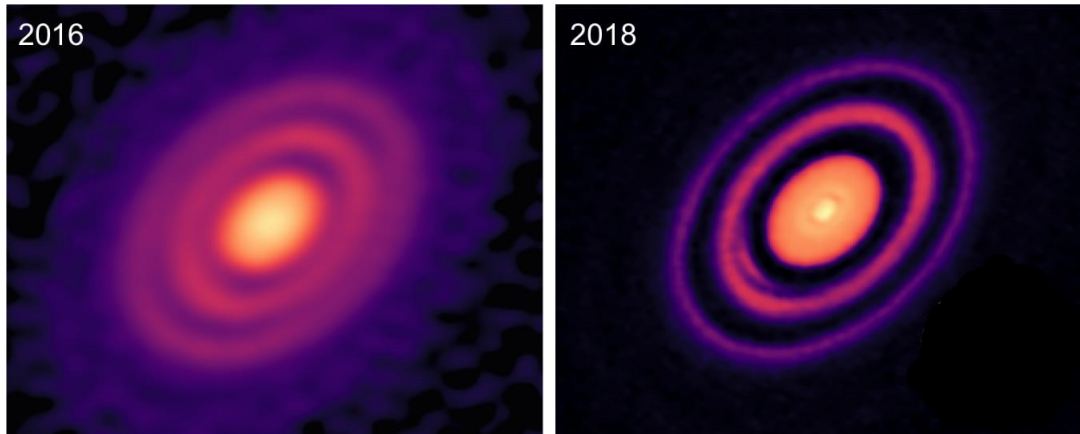


Figure 1.1: A protoplanetary disk, the disk of gas and dust in which planets are formed, is imaged two years apart, with the later image in higher angular resolution. Taken by the ALMA (Atacama Large Millimeter Array) radio telescope, from 2016 and 2018 [27],[1].

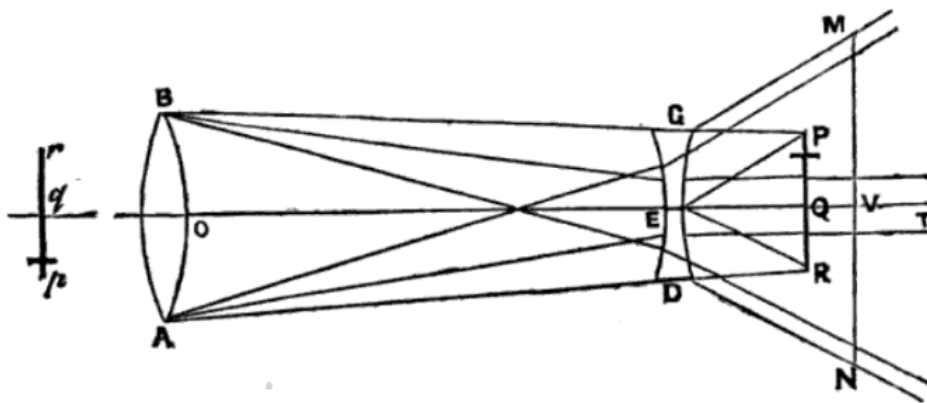


Figure 1.2: Determining the magnification of a Galilean telescope in a drawing by Sir William Herschel. Light enters from the left and the eye-glass is on the right. Segment AB is the aperture, OQ is the focal length of the telescope, and EQ is the focal length of the eye-glass [23]

tremely large pieces of glass became too difficult. The largest refractor in existence was built in 1897 at Yerkes Observatory in Wisconsin; it measures 18.9 meters long and 1.02 meters in diameter [20].

Reflecting telescopes offer an alternative to refracting telescopes and are called as such because they reflect (bounce) light rays from objects to the observer. Reflectors were developed almost concurrently with refractors; the first one was designed by Niccolo Zucchi in 1616, but faced technical implementation problems. These issues were mostly associated with the material (it was before the time of glass mirrors) such as difficulty shaping and polishing, and the material absorbing certain colors. The Newtonian telescope (Figure (1.3)), invented in 1668 by Sir Isaac Newton, and the Cassegrain telescope (Figure (1.4)), invented in 1672 by Laurent Cassegrain, are the most widely used designs today. Over time, reflectors became the telescope of choice because multiple mirrors could be used to bounce light multiple times, yielding a longer telescope focal length without a longer containing tube [50].

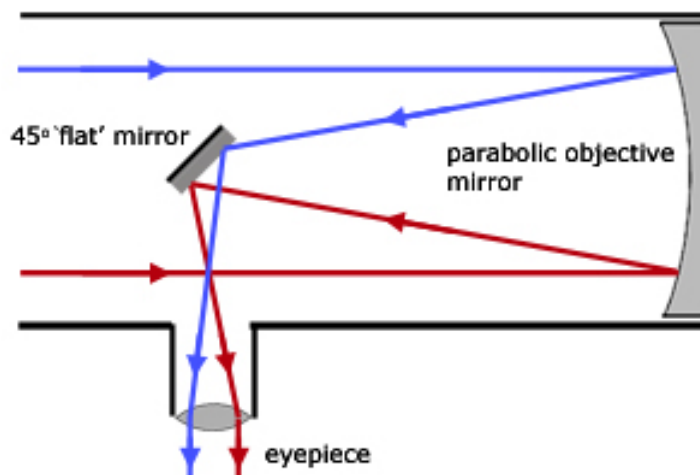


Figure 1.3: Diagram of the light rays inside a Newtonian reflecting telescope [31].

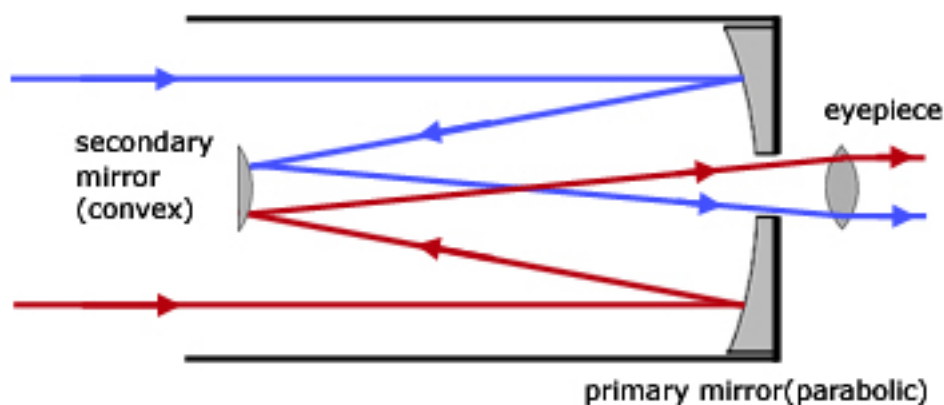


Figure 1.4: Diagram of the light rays inside a Cassegrain reflecting telescope [31].

Hundreds of years later, when humans entered the era of space travel, (reflecting) telescopes were put into space. This solved the problem of the atmosphere distorting the image of Earth-based telescopes, called atmospheric "seeing" [12]. However, larger telescopes are more costly both to make and to launch into space. The cost does not scale linearly with aperture length; rather, it scales with aperture to the 2.5 power [45]. Segmented mirror designs—those which employ multiple small mirrors joined together rather than a single giant mirror—have a slightly less drastic power law cost behavior, estimated to be to the 2.0 power [45]. As telescopes become larger in the quest for gathering more light, this scaling will soon yield telescopes with prices in the tens of billions of Euros. Thus, scientists are always searching for an alternative.

1.2. Kipping's Terrascope

In 2019, inspired by ideas to use the sun's gravitational field as a gravitational lens, David Kipping of Columbia University put forth the idea of using the Earth's gaseous atmosphere

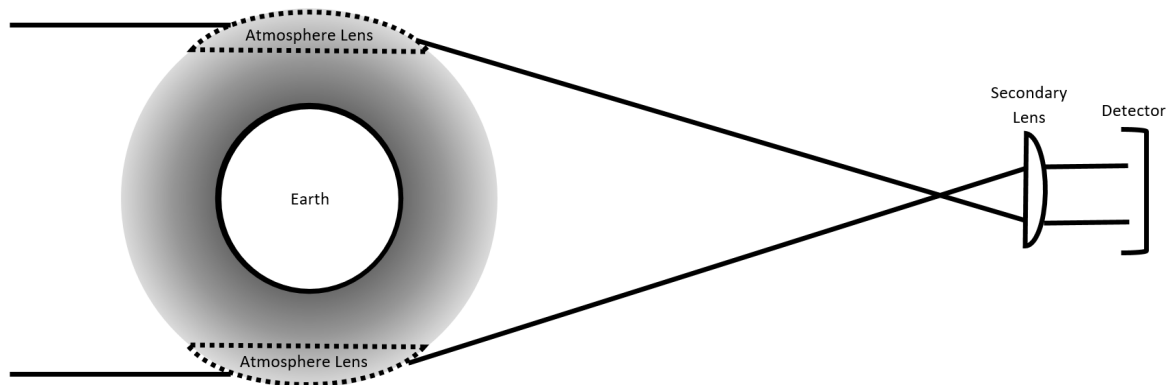


Figure 1.5: Diagram of the Terrascope, with parallel light rays from the celestial object entering the Earth's atmosphere from the left, passing through, being focused by a lens, and ending at the detector. The top of the atmosphere is outlined in dashed lines to show its resemblance to a lens, such as the secondary lens. This secondary lens is not necessary for the Terrascope to function, but is shown here to highlight the similar shapes of the atmosphere and a lens. Figure not to scale.

as an optical refracting lens [43], [28]. The premise is based on the atmosphere resembling a convex lens, thicker on the "bottom" and thinner at the "top", causing light rays which pass through to converge. A detector would then be placed at the convergence point to collect the light from the celestial objects which pass behind the Earth, and whose light is lensed. Since the concept uses the Earth's atmosphere as a natural lens, Kipping calls it the "Terrascope". A representation of the set-up is seen in Figure (1.5), where a second lens is used to aim the light into a detector (although this is not necessary).

If it works, the possible benefits of the Terrascope are: (1) the amplification would be unparalleled because a lens this large has never been used, (2) it is relatively cheap because amplification is achieved by using a pre-existing lens, and thus nothing has to be created and launched into space other than a light-gathering detector, (3) it opens doors to other solar system objects being used for similar endeavors, and (4) it has potential for use as an amplifier for sending signals into space, in addition to receiving them.

In his paper, Kipping outlines his plan for the Terrascope and walks through a proof of concept. He begins with splitting the Earth's atmosphere into concentric shells of equal height that are constant in climate over each shell. Six different temperature-pressure profiles are applied to the shells to investigate the impact of differing latitudes and seasons. Rays of light pass through the shells, refracting (bending) as they hit each consecutive shell boundary. The minimum depth each ray penetrates is recorded, along with the total bending angle, and how much material it travels through (airmass). These variables heavily depend upon where the ray first hits the atmosphere— called the "impact parameter"— and so a critical impact parameter is calculated. It ranges in value from 1.7-2.3km depending upon the temperature-pressure profile and light wavelength Kipping uses. He then sets about determining the focal point. Interestingly, because there is an upper and lower impact parameter for the top and bottom of the detector, respectively, there exists a focal line. The inner (closest to Earth) point along

this line has the highest potential amplification: closer and there is no image. The inner focus ranges in value from 200,000-350,000km, again depending upon the atmospheric profile and wavelength used. For comparison, the moon is at a distance of 384,400km [15]. The image at any given location along the focal line is a ring of lensed light. It is a ring rather than a complete image because the atmosphere is also only a ring; it is comparable to refracting light through only the outer rim of a lens and blocking the center. This ring is circularly symmetric if the celestial object is directly in line with the Earth and collecting detector, called "on-axis". If the celestial object is "off-axis", then the ring is oval shaped. Kipping takes into account the absorption of light by the particles in the atmosphere by using a transmittance model. He determines that the amount of light blocked in this manner is roughly equivalent to that of a telescope on a high mountain with excellent seeing (not much atmospheric disturbance). He accounts for clouds by using effective cloud fraction data and noting that above a certain altitude, clouds are mostly absent from the atmosphere. He determines that if the detector is placed at one Hill-sphere radius (1,500,000km), the rays only penetrate down to a height of 13.7km and only 10% of light is lost. Thus, Kipping proposes to put the Terrascope at this distance. Before calculating the final amplification, he cuts his estimate in half to account for half of the light being unusable due to the Sun's position. When the Sun is behind the Earth from the point of view of the detector, light from the Sun scattering through the Earth's upper atmosphere will cause background light that cannot be removed, thus rendering the observations during that period unusable. When the Sun is at a 90° to the detector, an occulter must be used and half of the light is unusable. The final number at which Kipping arrives is 22,500 times the amplification of the object when using a 1m detector, at a distance of 150,000,000km, for 1000nm light. For comparison, this is equivalent to using a 150m telescope in space. The Terrascope has the potential for unprecedented amplifying power, and deserves a more in-depth investigation. Such is the basis for this thesis work.

1.3. Central Flash

Although Kipping's research is the basis for our work, he is not the first to propose that an atmosphere can act as a lens to cause the amplification of light. In 1976, while studying the occultation of a star by Mars, J. L. Elliot observed a "central flash" as Mars passed in front of the star [14]. In 1977, Elliot's frequent collaborator, W. B. Hubbard, wrote about this phenomenon as a "bright central spot" and hypothesized about its amplification and potential uses [25]. In Hubbard's paper, he suggested that the bright spot could be used to form images of celestial objects, as a kind of "telescope". Using Mars' atmosphere, placing the detector a distance of 150,000,000km away, and observing at 500nm, Hubbard calculated that his "telescope" gathered as much light as a 100m conventional telescope. Hubbard's research is relevant to Kipping's and our own work; unfortunately, it did not come to our attention until shortly before our publication. However, we mention the research in our report because the findings are useful and we hope that any future work on this topic will include it.

1.4. Research Questions

The research in this thesis will explore Kipping's Terrascope in more detail, using models of the Earth's atmosphere. The main research questions and sub-questions are as follows:

- Can the Terrascope be a useful telescope, and if so, to what extent?
 - What kind of numerical model is suitable for studying the Terrascope?
 - What physical effects will diminish the quality of the Terrascope?

1.5. Methodology

The questions will be answered in the remainder of this work. This chapter served as an introduction to telescopes and Kipping's Terrascope. Chapter 2 explains the Terrascope used in this work. Chapter 3 details the results of the research, with a focus on different effects and how they vary with certain parameters. Chapter 4 discusses the final results, including a comparison to Kipping's work. Chapter 5 answers the research questions and sets a path for future work.

2

This Terrascope

The numerical Terrascope in this work is designed to model the light from stars which traverses the Earth's atmosphere, bending as it does so, and enters a light detector some distance away. In the following chapter, we will outline the methods used to develop our Terrascope and how the model itself functions. For continued reference throughout the chapter, Figure (2.1) shows the geometrical set up of this Terrascope labeled with important parameters. Although both aim to simulate the same phenomena, there are a number of differences between Kipping's model and the model developed in this research; when necessary, these differences will be explained. In this chapter, first we will explore how light is traced, starting with the foundations of optics. Next, we will describe the propagation of light rays using equations of motion. Finally, we will explain the three variations of codes used in this research.

2.1. Ray Tracing

Essential to tracing light from a celestial object, through the Earth's atmosphere, and into the detector is understanding how that light will travel. Geometric optics is a model describing light as rays or beams [10]. This model is the most useful for this research because light will be traced through different media, and the "line" of light will bend at each boundary. As Richard Feynman said in one of his lectures:

If one has an actual, detailed problem in lens design, including analysis of aberrations, then he is advised to read about the subject or else simply to trace the rays through various volumes (which is what the book tells us how to do), using the law of refraction from one side to the other, and to find out where they come out and see if they form a satisfactory image. People have said that this is too tedious, but today, with computing machines, it is the right way to do it [16].

Today, even more so than when this was said in 1961, computers are best suited to performing geometrical optics calculations. In the following section, the principles behind these optics will be explored.

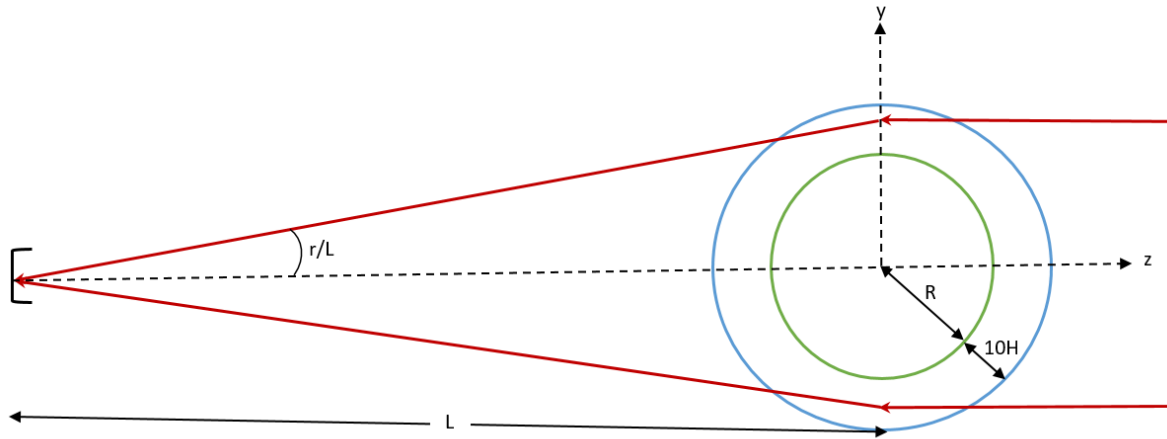


Figure 2.1: Geometry of the Terrascope, not to scale. Green is the boundary of the Earth's surface, blue is the boundary of the atmosphere, and red are the same rays of light from an astronomical object. The incoming rays are always assumed to be parallel. The y -direction is vertical and the x -direction (not shown) points out of the plane of the page. In reality and in the model, the Earth and the atmosphere around it are spherical. The z -direction is the direction of light propagation. Rays are propagated from the detector on the left, which is situated at a position of $z=-L$. R is the radius of the Earth and $10H$ is the height of the atmosphere, where H is the atmospheric scale height. r is the position of the ray and r/L is the angle at which it enters the detector, in the small angle approximation.

2.1.1. Refraction

Refraction is the phenomenon of light bending when it travels from one medium (environment) to another. Observations going back thousands of years recorded that the amount of bending is determined by the two mediums and the angle at which the light ray strikes their interface. This striking angle is called the "angle of incidence", denoted θ_i , and the bent angle is called the "angle of refraction", denoted θ_r . Simple refraction is shown in Figure (2.2). In 1621,

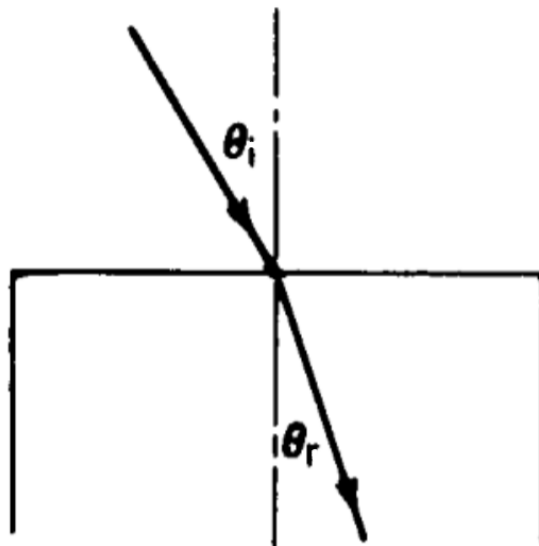


Figure 2.2: The rectangular box structure represents an enclosed medium, through which a light ray is passing. The line perpendicular to the surface is called the "normal", and it is with respect to this line that the angles of incidence and refraction, θ_i and θ_r , respectively, are measured [17].

Willebrord Snell deduced a law describing how light bends, and which took into account the angles and the medium [17]. Snell's law is as follows:

$$n_i \sin(\theta_i) = n_r \sin(\theta_r) \quad (2.1)$$

Where

- θ_i : angle of incidence, the angle inside the incident/first medium at which the light ray strikes the surface
- θ_r : angle of refraction, the angle inside the refracted/second medium at which the light ray leaves the surface
- n_i : incident medium refractive index, the number describing how fast light travels in the incident/first medium (equal to the ratio of the speed of light in a vacuum to the speed of light in the medium)
- n_r : refractive medium refractive index, the number describing how fast light travels in the refracted/second medium (equal to the ratio of the speed of light in a vacuum to the speed of light in the medium)

The practical implications of this law are as follows: when light travels from a thinner medium to a thicker medium (from where light moves faster to where it moves slower), the angle of incidence is larger than the angle of refraction, i.e. the light ray bends inward, toward the normal. When light travels from a thicker medium to a thinner medium (from where light moves slower to where it moves faster), the angle of incidence is smaller than the angle of refraction, i.e. the light ray bends outward, away from the normal. The refraction phenomenon can be explained by Fermat's Principle of Least Time, which states that light travels between points such that it takes the least possible time. When materials change, the speed of light changes accordingly, and so the light changes its path to traverse the new medium as quickly as possible [17].

An instance of refraction seen in everyday life is that of the setting Sun appearing higher in the sky than it actually is, shown in Figure (2.3). The Earth's atmosphere is thicker at lower alti-

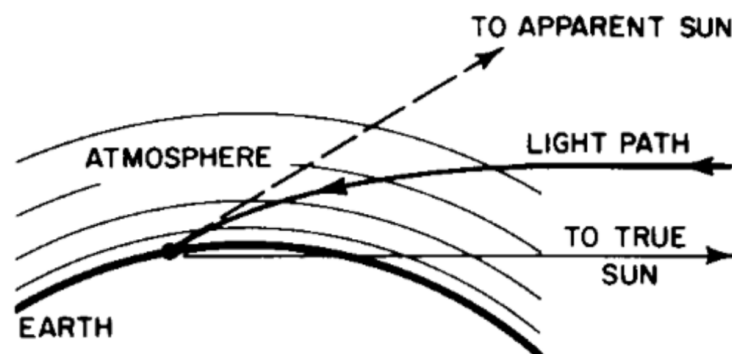


Figure 2.3: Setting sunlight enters the atmosphere at a higher altitude in order to avoid the slowing effects of the thicker atmosphere at lower altitudes. The resulting bent light makes it appear as if the Sun is higher in the sky than its true position below the horizon [17].

tudes and becomes thinner with increasing altitude. Thus, when the Sun is low on the horizon (close to setting), the light rays must travel through many layers of the thickest atmosphere at a shallow angle to arrive at someone observing the setting Sun. The speed of light is slower in thicker mediums, so to comply with the Principle of Least Time, the light instead enters the atmosphere at a higher altitude, where the atmosphere is thinner, and then travels at a steeper angle to arrive at the observer. This steeper angle at which light arrives makes it appear as if the Sun is higher in the sky than is really is. Thus, when one sees the Sun set below the horizon, it has actually already dropped behind the true horizon [17].

Astronomical refraction refers to the angular displacement of astronomical objects from their expected position due to refraction in the Earth's atmosphere [51]. This effect was discovered because the apparent positions of celestial objects differed from what they were expected to be via trigonometric computations. In 1587, Tycho Brahe used the difference in position of the Sun at the summer and winter solstices to measure astronomical refraction and calculate it for different apparent zenith angles. In 1656, Cassini improved upon this by using Snell's law; a drawing of this can be seen in Figure (2.4).

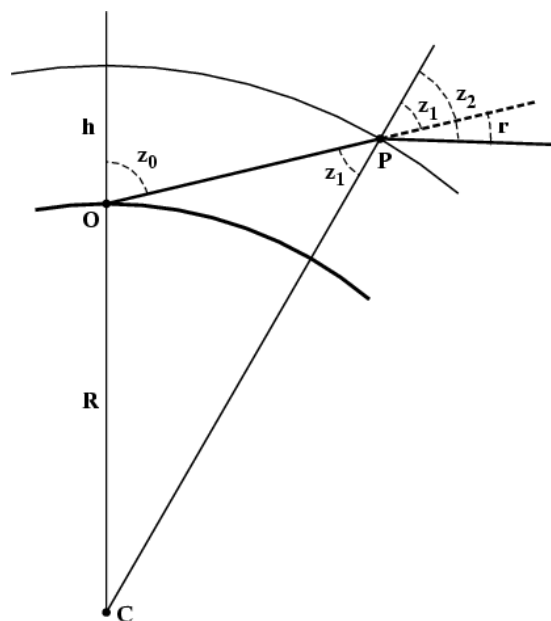


Figure 2.4: Cassini's model of atmospheric refraction. The bolder arc is the surface of the Earth and the thinner arc is the atmosphere. C is the center of the Earth, R is the radius of the Earth, O is the observer, P is where the light ray from the star enters the atmosphere, h is the height above the surface where the ray enters, and r is the ray itself. Line segment CP is the normal to the surface and atmosphere boundary. The light ray enters the atmosphere at an angle z_2 to the normal, but exits and is viewed by the observer at angle z_1 . Note that $z_1 < z_2$ because the atmosphere is denser than the vacuum of space [52].

Both Brahe and Cassini assumed that refraction only happened in one place— at the top of the atmosphere of fixed height. Later, atmospheric measurements were taken and it was discovered that the pressure and temperature change with increasing altitude. In 1669, Picard discovered that the astronomical refraction depends on temperature and in 1708, Hawksbee discovered that it also depends on density. These new insights lead to the development of

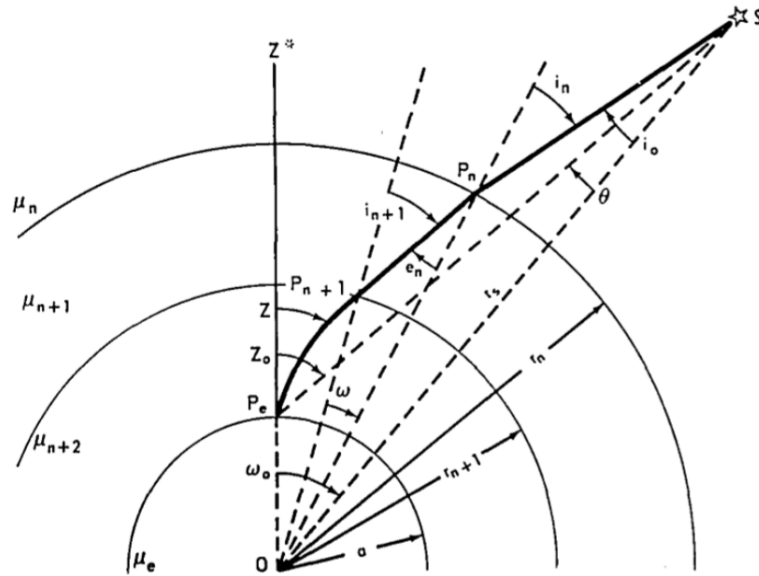


Figure 2.5: Similar to Figure (2.4, but with two atmospheric layers, although more are necessary to closely approximate the gradual change in atmosphere with increasing altitude. Here, O is the center of the Earth, a is the radius of the Earth, P_e is the observer, P_n is where the light ray from the star enters the atmosphere, P_{n+1} is another atmospheric shell, r_n is the height above the surface where the ray enters, and r_{n+1} is the height of the other atmospheric shell. The light ray enters the atmosphere at angle i_n , bends to e_n , enters the next shell at i_{n+1} , bends to $Z_0 - Z$ [32].

the concentric spherical shell model for astronomical refraction, seen in Figure (2.5). These shells are local regions where the composition, pressure, and temperature are assumed to be constant. Therefore, they also have constant refractive index [32]. As the atmospheric altitude increases, the density, and therefore the refractive index, decreases. Thus, each concentric shell has a smaller value of n . This is exactly the theory upon which Kipping's calculations are based. As was mentioned in the Terrascope section of the Introduction, it is expected that light rays from celestial objects will penetrate the atmosphere and refract through consecutive layers, where the bending angle will depend on the physical properties of the atmosphere at each layer. In our Terrascope, we take the number of shells to approach infinity, thus creating a continuous, rather than discrete, change in n . We model the change in n by using the gradient, ∇n . This technique is known as gradient-index optics and will be outlined in the following section.

2.1.2. Gradient-Index Optics

Recall from the previous section Fermat's Principle stating that light travels between points in the least possible time. We can represent the integral of this light path between points as [33]:

$$S = \int_{P_0}^P n(\mathbf{r}) ds \quad (2.2)$$

$$= \int_{P_0}^P n(x, y, z) ds \quad (2.3)$$

Where

- S : light path integral
- P_0, P : two points between which the light is traveling
- $n(\mathbf{r}) = n(x, y, z)$: refractive index as a function of coordinate position
- ds : an element of the path length

Noting that an element of the path length is equal to an element of time multiplied by the velocity, we make the substitution $ds = vdt$, yielding:

$$S = \int_{P_0}^P n(\mathbf{r})vdt \quad (2.4)$$

In order for light to travel between these points in the least possible time, we aim to minimize the integral. An integral in the form of Equation (2.4) is known as the "action", and minimizing the action is known as the Principle of Least Action. We apply this principle to the optical system at hand to define its equations of motion. We do this by deriving the Lagrangian. The action, Equation (2.4), takes the form [29]:

$$S = \int \mathcal{L}dt \quad (2.5)$$

and thus our Lagrangian is:

$$\mathcal{L}(\mathbf{r}, \dot{\mathbf{r}}) = n(\mathbf{r})v \quad (2.6)$$

$$\mathcal{L}(x, y, z, \dot{x}, \dot{y}, \dot{z}) = n(x, y, z)\sqrt{\dot{x}^2 + \dot{y}^2 + \dot{z}^2} \quad (2.7)$$

Where

- $\dot{x}, \dot{y}, \dot{z}$: derivative of position coordinates with respect to time
- v : absolute velocity

From here, we will derive the Euler-Lagrange equation:

$$\frac{d}{dt} \frac{\partial \mathcal{L}}{\partial \dot{\mathbf{r}}} = \frac{\partial \mathcal{L}}{\partial \mathbf{r}} \quad (2.8)$$

Since the time derivative of position is velocity and the velocity also has three components, we can rewrite the second term on the left hand side as:

$$\frac{\partial \mathcal{L}}{\partial \dot{\mathbf{r}}} = \frac{\partial \mathcal{L}}{\partial \mathbf{v}} = \begin{pmatrix} \frac{d\mathcal{L}}{dv_1} \\ \frac{d\mathcal{L}}{dv_2} \\ \frac{d\mathcal{L}}{dv_3} \end{pmatrix} \quad (2.9)$$

Since $\mathcal{L} = n(\mathbf{r})v$:

$$\frac{d\mathcal{L}}{dv_1} = n(\mathbf{r}) \frac{\partial v}{\partial v_1} \quad (2.10)$$

$$\begin{aligned} &= n(\mathbf{r}) \frac{\partial \sqrt{v_1^2 + v_2^2 + v_3^2}}{\partial v_1} \\ &= \frac{n(\mathbf{r})}{2\sqrt{v_1^2 + v_2^2 + v_3^2}} \frac{\partial (v_1^2 + v_2^2 + v_3^2)}{\partial v_1} \\ &= \frac{2v_1 n(\mathbf{r})}{2\sqrt{v_1^2 + v_2^2 + v_3^2}} \\ &= \frac{n(\mathbf{r})v_1}{v} \end{aligned} \quad (2.11)$$

Similarly, for the other components:

$$\frac{d\mathcal{L}}{dv_2} = \frac{n(\mathbf{r})v_2}{v} \quad (2.12)$$

$$\frac{d\mathcal{L}}{dv_3} = \frac{n(\mathbf{r})v_3}{v} \quad (2.13)$$

Thus:

$$\begin{pmatrix} \frac{d\mathcal{L}}{dv_1} \\ \frac{d\mathcal{L}}{dv_2} \\ \frac{d\mathcal{L}}{dv_3} \end{pmatrix} = \begin{pmatrix} \frac{n(\mathbf{r})v_1}{v} \\ \frac{n(\mathbf{r})v_2}{v} \\ \frac{n(\mathbf{r})v_3}{v} \end{pmatrix} = \frac{n(\mathbf{r})}{v} \begin{pmatrix} v_1 \\ v_2 \\ v_3 \end{pmatrix} = \frac{n(\mathbf{r})\mathbf{v}}{v} \quad (2.14)$$

Defining:

$$\hat{\mathbf{v}} = \frac{\mathbf{v}}{v} \quad (2.15)$$

We get:

$$\frac{\partial \mathcal{L}}{\partial \mathbf{r}} = n(\mathbf{r})\hat{\mathbf{v}} \quad (2.16)$$

As for the right hand side of Equation (2.8):

$$\frac{\partial \mathcal{L}}{\partial \mathbf{r}} = \frac{\partial n(\mathbf{r})v}{\partial \mathbf{r}} = v\nabla n(\mathbf{r}) \quad (2.17)$$

Where in the last step we have used the definition of the gradient as the partial derivative with respect to the position of a vector. Additionally, the partial derivative of v is treated as a constant because v is only a function of $\dot{x}, \dot{y}, \dot{z}$, not of x, y, z .

Finally, we formulate the gradient-index optics Euler-Lagrange equation as:

$$\frac{d}{dt} (n(\mathbf{r})\hat{\mathbf{v}}) = v\nabla n(\mathbf{r}) \quad (2.18)$$

2.1.3. Equations of Motion

In this section, we derive the equations of motion from Equation (2.18) and explain how they are implemented in our Terrascope model. First, we evaluate the left-hand side of the equation, using the chain rule in the first two steps:

$$\frac{d}{dt} (n(\mathbf{r})\hat{\mathbf{v}}) = \frac{dn(\mathbf{r})}{dt}\hat{\mathbf{v}} + n(\mathbf{r})\frac{d\hat{\mathbf{v}}}{dt} \quad (2.19)$$

$$= \left(\frac{\partial n}{\partial x} \frac{dx}{dt} + \frac{\partial n}{\partial y} \frac{dy}{dt} + \frac{\partial n}{\partial z} \frac{dz}{dt} \right) \hat{\mathbf{v}} + n(\mathbf{r})\frac{d\hat{\mathbf{v}}}{dt} \quad (2.20)$$

Note that if we again use the definition of the gradient as the partial derivative with respect to the position of a vector, then the first term of Equation (2.20) can be written:

$$\left(\frac{\partial n}{\partial x} \frac{dx}{dt} + \frac{\partial n}{\partial y} \frac{dy}{dt} + \frac{\partial n}{\partial z} \frac{dz}{dt} \right) \hat{\mathbf{v}} = (\nabla n(\mathbf{r}) \cdot \mathbf{v}) \hat{\mathbf{v}} \quad (2.21)$$

Writing and then rearranging the full Euler-Lagrange equation with the new terms:

$$(\nabla n(\mathbf{r}) \cdot \mathbf{v}) \hat{\mathbf{v}} + n(\mathbf{r})\frac{d\hat{\mathbf{v}}}{dt} = v\nabla n(\mathbf{r}) \quad (2.22)$$

$$n(\mathbf{r})\frac{d\hat{\mathbf{v}}}{dt} = v\nabla n(\mathbf{r}) - (\nabla n(\mathbf{r}) \cdot \mathbf{v}) \hat{\mathbf{v}}$$

$$n(\mathbf{r})\frac{d\hat{\mathbf{v}}}{dt} = v\nabla n(\mathbf{r}) - (\mathbf{v} \cdot \nabla n(\mathbf{r})) \hat{\mathbf{v}}$$

$$n(\mathbf{r})\frac{d\hat{\mathbf{v}}}{dt} = v\nabla n(\mathbf{r}) - \hat{\mathbf{v}}(v\hat{\mathbf{v}} \cdot \nabla n(\mathbf{r}))$$

$$n(\mathbf{r})\frac{d\hat{\mathbf{v}}}{dt} = v(\nabla n(\mathbf{r}) - \hat{\mathbf{v}}\hat{\mathbf{v}} \cdot \nabla n)$$

$$\frac{d\hat{\mathbf{v}}}{dt} = \frac{v}{n(\mathbf{r})} (\nabla n(\mathbf{r}) - \hat{\mathbf{v}}\hat{\mathbf{v}} \cdot \nabla n(\mathbf{r})) \quad (2.23)$$

Since velocity is the speed of the light ray, we define our units as $v = c = 1$, where c is the speed of light in a vacuum. Thus:

$$\frac{d\hat{\mathbf{v}}}{dt} = \frac{1}{n(\mathbf{r})} (\nabla n(\mathbf{r}) - \hat{\mathbf{v}}\hat{\mathbf{v}} \cdot \nabla n(\mathbf{r})) \quad (2.24)$$

We want a final equation in terms of the vector velocity and z -component. In the following steps, we use the chain rule, the definition of v_3 , Equation (2.15), and $v = 1$ (respectively):

$$\frac{d\mathbf{v}}{dz} = \frac{d\mathbf{v}}{dt} \frac{dt}{dz} \quad (2.25)$$

$$= \frac{d\mathbf{v}}{dt} \frac{1}{v_3}$$

$$= \frac{1}{v_3} \frac{d(v\hat{\mathbf{v}})}{dt}$$

$$= \frac{1}{v_3} \frac{d\hat{\mathbf{v}}}{dt} \quad (2.26)$$

Combining Equations (2.24) and (2.26) we arrive at:

$$\frac{d\mathbf{v}}{dz} = \frac{1}{n(\mathbf{r})v_3} (\nabla n(\mathbf{r}) - \hat{\mathbf{v}}\hat{\mathbf{v}} \cdot \nabla n(\mathbf{r})) \quad (2.27)$$

We now break this into component form and show the derivation for v_1 . We use $v_1^2 + v_2^2 + v_3^2 = 1$ to allow us to only calculate the v_1 and v_2 components, since the v_3 can be calculated from the first two. We also use different forms of the equality to make substitutions.

$$\frac{dv_1}{dz} = \frac{1}{n(\mathbf{r})v_3} \left(\frac{\partial}{\partial x} n(\mathbf{r}) - v_1 \begin{pmatrix} v_1 \\ v_2 \\ v_3 \end{pmatrix} \cdot \nabla n(\mathbf{r}) \right) \quad (2.28)$$

$$= \frac{1}{n(\mathbf{r})v_3} \left(\frac{\partial n(\mathbf{r})}{\partial x} - v_1^2 \frac{\partial n(\mathbf{r})}{\partial x} - v_1 v_2 \frac{\partial n(\mathbf{r})}{\partial y} - v_1 v_3 \frac{\partial n(\mathbf{r})}{\partial z} \right)$$

$$= \frac{1}{n(\mathbf{r})v_3} (1 - v_1^2) \frac{\partial n(\mathbf{r})}{\partial x} - \frac{v_1 v_2}{n(\mathbf{r})v_3} \frac{\partial n(\mathbf{r})}{\partial y} - \frac{v_1 v_3}{n(\mathbf{r})v_3} \frac{\partial n(\mathbf{r})}{\partial z}$$

$$= \frac{1}{n(\mathbf{r})v_3} (v_2^2 + v_3^2) \frac{\partial n(\mathbf{r})}{\partial x} - \frac{v_1 v_2}{n(\mathbf{r})v_3} \frac{\partial n(\mathbf{r})}{\partial y} - \frac{v_1}{n(\mathbf{r})} \frac{\partial n(\mathbf{r})}{\partial z}$$

$$= \frac{v_3}{n(\mathbf{r})} \frac{\partial n(\mathbf{r})}{\partial x} + \frac{v_2^2}{n(\mathbf{r})v_3} \frac{\partial n(\mathbf{r})}{\partial x} - \frac{v_1 v_2}{n(\mathbf{r})v_3} \frac{\partial n(\mathbf{r})}{\partial y} - \frac{v_1}{n(\mathbf{r})} \frac{\partial n(\mathbf{r})}{\partial z} \quad (2.29)$$

To complete the equations of motion, we must choose a suitable refractive index function, $n(\mathbf{r})$. We aim for it to represent how the refractive index, n , varies in an atmosphere. This variation is proportional to the atmospheric density. Since density exponentially decreases with increasing altitude, the same is true of refraction. Thus, we define the following function:

$$n(\mathbf{r}) = 1 + \eta_0 e^{\frac{-(\mathbf{r}-R)}{H}} \quad (2.30)$$

Where

- η_0 : refractivity at sea level
- H : scale height, defined as the distance over which values decrease by a factor of $1/e$

Since n is exponentially decreasing, using scale height is a natural choice for this type of description.

After evaluating Equation (2.30) in Equation (2.29) and similarly for v_2 , we arrive at the final equations of motion:

$$v_3 = \sqrt{1 - v_1^2 - v_2^2} \quad (2.31)$$

$$\begin{pmatrix} \frac{dx}{dz} \\ \frac{dy}{dz} \end{pmatrix} = \begin{pmatrix} \frac{v_1}{v_3} \\ \frac{v_2}{v_3} \end{pmatrix} \quad (2.32)$$

$$\begin{pmatrix} \frac{dv_1}{dz} \\ \frac{dv_2}{dz} \end{pmatrix} = \frac{-\eta_0}{H\sqrt{x^2 + y^2 + z^2}} \begin{pmatrix} v_3x - v_1z + \frac{v_2^2x}{v_3} - \frac{v_1v_2y}{v_3} \\ v_3y - v_2z + \frac{v_1^2y}{v_3} - \frac{v_1v_2x}{v_3} \end{pmatrix} \exp\left(\frac{-(\sqrt{x^2 + y^2 + z^2} - R)}{n(x, y, z)H}\right) \quad (2.33)$$

Since the refractive index is close to unity, i.e $n \sim 1$, we use this approximation in our code.

Before propagating these equations using a numerical method, an important difference between our model and Kipping's must be highlighted. Unlike in Kipping's Terrascope and the way in which the traveling light acts in nature, our Terrascope models the light from the detector to the light source (the celestial object), rather than source to detector. In our model, light rays propagate from the detector at a range of angles, into one end of the Earth's atmosphere, and exit the opposite end. We used a backwards propagation scheme because the final angle of the light entering the detector can be determined geometrically and then used to calculate all intermediate positions in the atmosphere. This is computationally cheaper to do than begin with parallel rays, pass them through the atmosphere, and end with only a fraction hitting the detector. By starting at the detector, we ensure that we only analyze rays that hit the detector, which are those of importance for determining the usefulness of the Terrascope.

Using Figure (2.1) as a reference, we see that starting light rays at the detector is numerically represented as $z_{\text{start}} = -L$, where z_{start} is the z -coordinate of the detector. To derive the x and y coordinates of the initial positions, we use Figure (2.6), which shows the coordinate system of position and velocity.

The x and y positions of the rays are initialized as follows:

$$x_{\text{start}} = \frac{v_1}{v_3}(z_{\text{start}} + L) \quad (2.34)$$

$$y_{\text{start}} = \frac{v_2}{v_3}(z_{\text{start}} + L) \quad (2.35)$$

As previously mentioned, z_{start} is normally the detector, making $z_{\text{start}} = -L$. However, we determined that the faster, and still accurate, way to propagate the rays is to start them at the

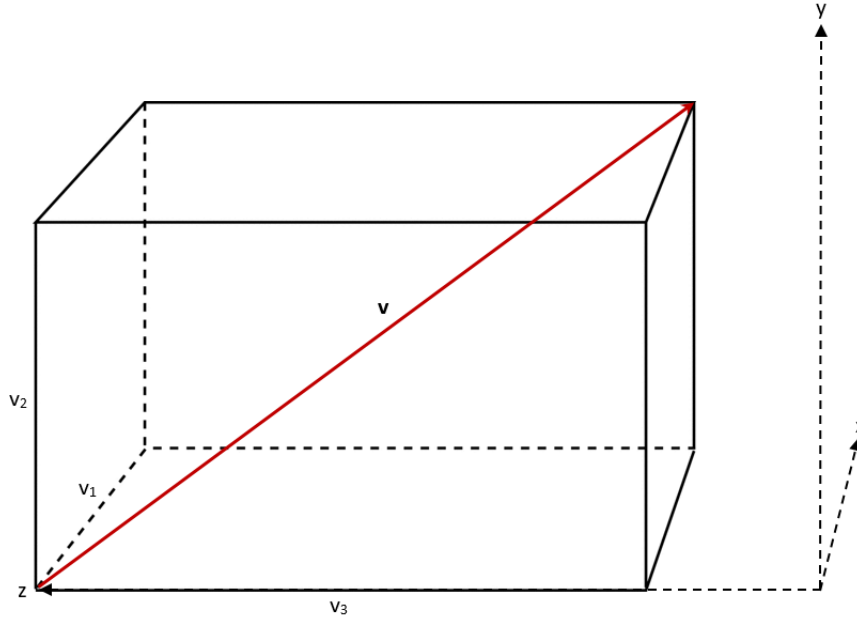


Figure 2.6: Terrascope coordinate system showing the velocity vectors. The origin is the center of the Earth, so the starting values at the detector are negative. The red line shows a single light ray emanating from the detector and travelling towards the Earth's atmosphere. In reality, the light travels from celestial object, through Earth's atmosphere, towards the detector, but our model runs simulations in the opposite direction. A light ray is uniquely defined by its starting angle at the detector. This angle is in turn defined by its x and y components, the v_1 and v_2 values, respectively. Figures (2.7a) and (2.7b) show these components.

edge of the atmosphere rather than at the detector. The edge of the atmosphere is defined as $R + 10H$, shown also in Figure (2.1). A light ray positioned at the atmosphere is defined as $\sqrt{x^2 + y^2 + z^2} = R + 10H$. The z -coordinate of this starting position is analytically calculated in the following manner:

$$\sqrt{x^2 + y^2 + z^2} = R + 10H \quad (2.36)$$

$$x^2 + y^2 + z^2 = (R + 10H)^2 \quad (2.37)$$

Now we replace x and y with Equations (2.34) and (2.35), then multiply both sides by v_3^2 to eliminate fractions:

$$\begin{aligned} \left(\frac{v_1}{v_3}(z + L)\right)^2 + \left(\frac{v_2}{v_3}(z + L)\right)^2 + z^2 &= (R + 10H)^2 \\ (v_1(z + L))^2 + (v_2(z + L))^2 + z^3 v_3^2 &= (R + 10H)^2 v_3^2 \end{aligned}$$

Factoring and rearranging terms:

$$\begin{aligned} (v_1^2 + v_2^2)(z + L)^2 + z^3 v_3^2 &= (R + 10H)^2 v_3^2 \\ (v_1^2 + v_2^2)(z^2 + 2zL + L^2) + z^3 v_3^2 &= (R + 10H)^2 v_3^2 \\ (v_1^2 + v_2^2)z^2 + (v_1^2 + v_2^2)2zL + z^3 v_3^2 &= (R + 10H)^2 v_3^2 - (v_1^2 + v_2^2)L^2 \end{aligned}$$

Using the fact that $v_1^2 + v_2^2 + v_3^2 = 1 \Rightarrow (v_1^2 + v_2^2) = 1 - v_3^2$ on the left hand side:

$$\begin{aligned} (1 - v_3^2)z^2 + (v_1^2 + v_2^2)2zL + z^2v_3^2 &= (R + 10H)^2v_3^2 - (v_1^2 + v_2^2)L^2 \\ z^2 - z^2v_3^2 + (v_1^2 + v_2^2)2zL + z^2v_3^2 &= (R + 10H)^2v_3^2 - (v_1^2 + v_2^2)L^2 \\ z^2 + (v_1^2 + v_2^2)2zL &= (R + 10H)^2v_3^2 - (v_1^2 + v_2^2)L^2 \end{aligned}$$

Add $(v_1^2 + v_2^2)^2L^2$ to each side and factor again:

$$\begin{aligned} z^2 + (v_1^2 + v_2^2)2zL + (v_1^2 + v_2^2)^2L^2 &= (R + 10H)^2v_3^2 - (v_1^2 + v_2^2)L^2 + (v_1^2 + v_2^2)^2L^2 \\ (z + L(v_1^2 + v_2^2))^2 &= (R + 10H)^2v_3^2 - (v_1^2 + v_2^2)L^2 + (v_1^2 + v_2^2)^2L^2 \end{aligned}$$

Take the square root of both sides and use the fact that $v_1^2 + v_2^2 + v_3^2 = 1 \Rightarrow v_3^2 = 1 - (v_1^2 + v_2^2)$ on the right hand side:

$$\begin{aligned} z + L(v_1^2 + v_2^2) &= \pm \sqrt{(R + 10H)^2v_3^2 - (v_1^2 + v_2^2)L^2 + (v_1^2 + v_2^2)^2L^2} \\ z + L(v_1^2 + v_2^2) &= \pm \sqrt{(R + 10H)^2(1 - (v_1^2 + v_2^2)) - (v_1^2 + v_2^2)L^2 + (v_1^2 + v_2^2)^2L^2} \end{aligned}$$

We choose the minus square root because our coordinate system is centered at the Earth and the detector is located on the left (negative) side (Figure (2.1)). Finally, we arrive at:

$$z_{start} = -L(v_1^2 + v_2^2) - \sqrt{(R + 10H)^2(1 - (v_1^2 + v_2^2)) - (v_1^2 + v_2^2)L^2 + (v_1^2 + v_2^2)^2L^2} \quad (2.38)$$

We initialize the positions using Equations (2.34), (2.35), and (2.38). We initialize the velocity using the following equation:

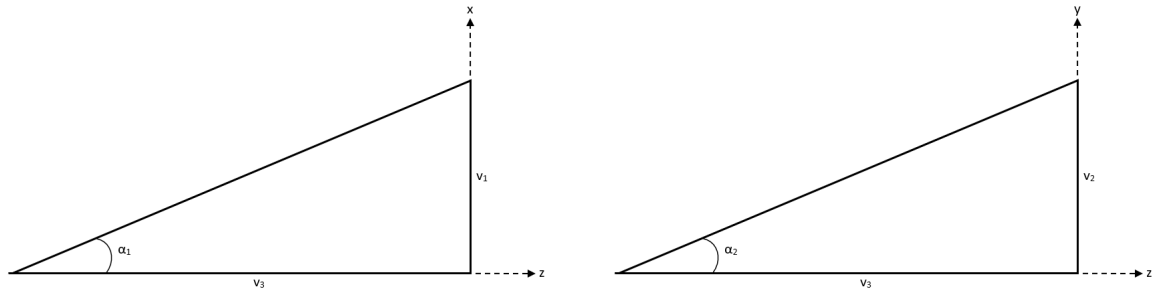
$$v_{1,2start} = \frac{-(R + 10H)}{L} \quad (2.39)$$

This comes from $v_1 = \frac{dx}{dz}$ and $v_2 = \frac{dy}{dz}$ where $dx, dy = -(R + 10H)$ is the farthest extent of the atmosphere on the left and $dz = L$ is the distance from the Earth to the atmosphere.

After setting the starting positions and velocities, we propagate light rays according to Equations (2.31), (2.32), and (2.33) by using the Leapfrog method [18]. At every step, usually defined to be some multiple of H , a check is performed to see if the ray has hit the Earth's surface or left the bounds of the atmosphere. This is performed by ensuring the ray's position, r , remains in the following bounds:

$$R < r < \frac{R + 10H}{L} \quad (2.40)$$

If r is outside the lower bound ($r < R$), then the ray has hit the surface of the Earth and will not be counted as light that enters the detector. If r is outside the upper bound ($r < \frac{R+10H}{L}$), then the ray has successfully finished its journey through the atmosphere and will be counted as a photon that entered the detector from the celestial object.



(a) Triangle showing velocity vectors used to calculate the x-direction of the angle which defines each light ray. Figure is not to scale; the angle is small enough to use the small angle approximation. Thus, $\tan(\alpha_1) = \alpha_1 = \frac{v_1}{v_3}$.

(b) Triangle showing velocity vectors used to calculate the y-direction of the angle which defines each light ray. Figure is not to scale; the angle is small enough to use the small angle approximation. Thus, $\tan(\alpha_2) = \alpha_2 = \frac{v_2}{v_3}$.

Figure 2.7: The x and y components of a light ray angle.

2.2. Types of Codes

An additional method for maximizing computational efficiency was using different codes which vary the number of light rays that propagate; each code is used for a specific purpose or output. However, all codes use the same coordinate system and method for calculating position, velocity, and angles. Figures (2.7a) and (2.7b) show how the coordinate system is broken up into triangles to calculate the light ray angles, α_1 , α_2 , starting at the detector. Note that the actual angles are much smaller than what is shown in the figure, and thus the small angle approximation applies when calculating them in the following way:

$$\tan(\alpha_1) = \frac{v_1}{v_3} \stackrel{\text{small angle approx}}{\Rightarrow} \alpha_1 = \frac{v_1}{v_3} \quad (2.41)$$

$$\tan(\alpha_2) = \frac{v_2}{v_3} \stackrel{\text{small angle approx}}{\Rightarrow} \alpha_2 = \frac{v_2}{v_3} \quad (2.42)$$

Since $v_3 \approx c = 1$, we make the further approximation:

$$\alpha_1 = v_1 \quad (2.43)$$

$$\alpha_2 = v_2 \quad (2.44)$$

These equalities are how we translate a light ray's starting angle to a starting velocity. The starting velocities are then used to propagate the ray using the equations of motion from the previous section.

The α_1, α_2 angles define a specific light ray and we can decrease the difference between each angle in order to produce a technically infinite number of rays. In practice, we propagate one to many billions of light rays, depending on the Terrascope code used. In the following sections, we give an overview of these codes.

2.2.1. Single Ray

The simplest code is that which only propagates one ray. This was necessary to visualize the path of the light and observe the effects on the path of the light by (1) the wavelength, λ , and (2) the distance between Earth and the detector, L . By using only one ray, we could vary these parameters over a wide range and the computation time would be reasonable. This would not be the case if we were to propagate millions of light rays, each for ten different wavelengths. The effect of these parameters is explored in Chapter 3.

Figure (2.8) shows how the path of a single ray varies with L , the distance between the detector and the center of the Earth. As L increases, the minimum altitude the ray reaches in the atmosphere also increases (meaning the light travels less deep in the atmosphere). As the minimum altitude increases, the total angle the ray bends, from the point of entry until the point of exit, decreases. This bending angle is calculated by subtracting the initial entry angle from the final exit angle. The relationship between bending angle and minimum ray altitude is shown in Figure (2.9). The relationship between the minimum altitude and L is explored further in Appendix A.

2.2.2. Angle Array

The second, most computationally expensive, Terrascope code is one which generates a two-dimensional array of light rays. The array contains angle values that range from one end of the atmosphere edge to the other. These extreme angles are derived by the right triangles found in Figure (2.10), where $R + 10H$ is opposite the opening angle, L is adjacent, and the light ray path is the hypotenuse. The angles are calculated as follows, again using the small angle approximation:

$$\tan(\alpha_{1,2}) = \frac{-(R + 10H)}{L} \xrightarrow{\text{small angle approx}} \alpha_{1,2} = \frac{-(R + 10H)}{L} \quad (2.45)$$

$$\tan(\alpha_{1,2}) = \frac{(R + 10H)}{L} \xrightarrow{\text{small angle approx}} \alpha_{1,2} = \frac{(R + 10H)}{L} \quad (2.46)$$

This generates the following arrays:

$$\alpha_1 = \left[\frac{-(R + 10H)}{L}, \dots, \frac{(R + 10H)}{L} \right] \quad (2.47)$$

$$\alpha_2 = \left[\frac{-(R + 10H)}{L}, \dots, \frac{(R + 10H)}{L} \right] \quad (2.48)$$

A nested for-loop goes through all combinations of angle values, generating a ray for each. Before propagating a ray, we perform a check to ensure that its initial angle will not cause it to go too low (hit the Earth's surface) or too high (never enter the atmosphere). This check is performed before propagation along the z-axis in order to save computation time. Figure (2.11) is a visual of the upper and lower limits, Equation (2.51) gives them numerically, again using the small angle approximation:

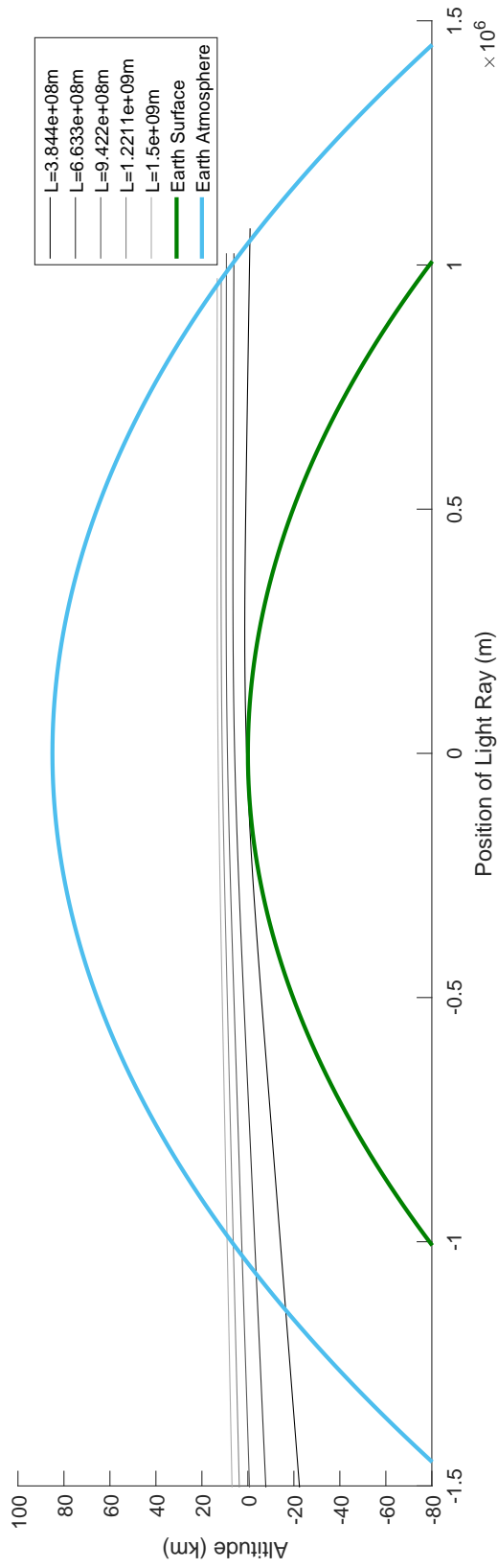


Figure 2.8: How the paths of light rays vary when traveling to detectors at different distances from the Earth. The detector is on the left; the celestial object is on the right. Green is the surface, blue is the atmosphere top, and the shades of gray represent the different distances. The farther the detector, the higher the minimum altitude that the ray reaches, or in other words, the less deep the light penetrates. Although our calculations are different from Kipping's, the results of the light rays' minimum altitude are approximately the same. For a ray of $L = 1.5 \times 10^9$ m, Kipping's Terrascope calculated the minimum altitude to be 13.7 km; our Terrascope calculated 13.8 km.

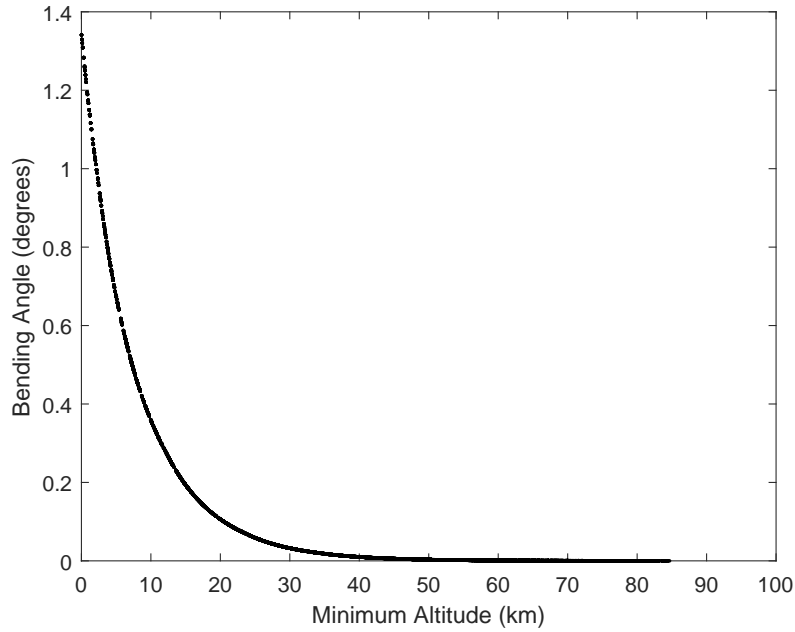


Figure 2.9: The angle that light bends while traveling through the atmosphere depends upon the minimum height –or depth– that it reaches. A ray which passes through lower layers of the atmosphere has a larger bending angle than a ray that remains closer to the top. This plot is shown for $L = 1.5 \times 10^9$ m.

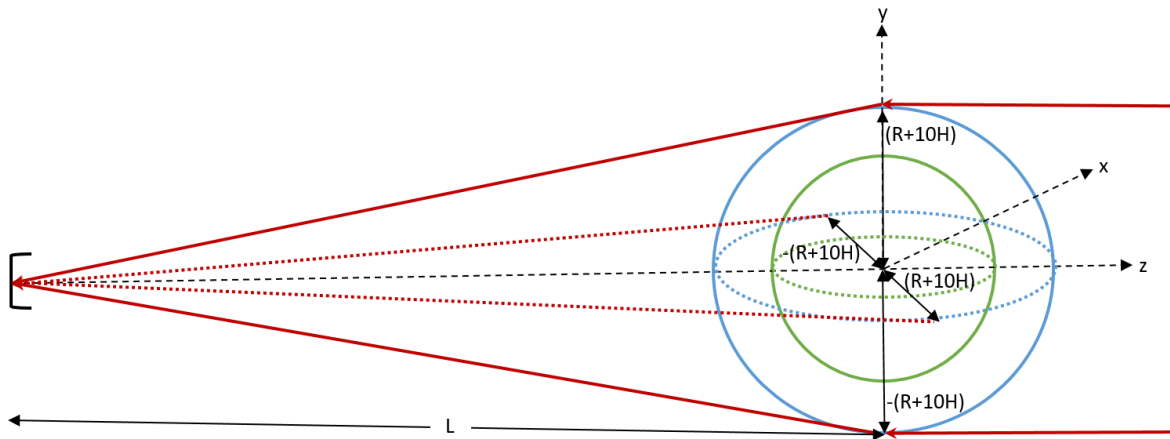


Figure 2.10: Three dimensional diagram of the maximum and minimum angles created for the angle array Terrascope. The green and blue lines represent the Earth's surface and atmosphere, respectively. The solid red lines are light rays in the y -plane hitting the outer edge of the atmosphere in each direction (the maximum and minimum values). The dashed red lines are light rays in the x -plane doing the same. L is the adjacent length to all of the angles emanating from the detector at left. Thus, using a small angle approximation, the maximum and minimum angle in both planes is $\frac{R+10H}{L}$ and $-\frac{(R+10H)}{L}$, respectively. The angle values, α_1 for the x -plane and α_2 for the y -plane, are components of the total angle which emanates from (or, in real life, enters into) the detector. The angles between detector and Earth make a cone shape.

$$\arctan\left(\frac{R}{\sqrt{L^2 - R^2}}\right) < \alpha < \arctan\left(\frac{R + 10H}{L}\right) \quad (2.49)$$

$$\arcsin\left(\frac{R}{L}\right) < \alpha < \arctan\left(\frac{R + 10H}{L}\right) \quad (2.50)$$

$$\frac{R}{L} < \alpha < \frac{R + 10H}{L} \quad (2.51)$$

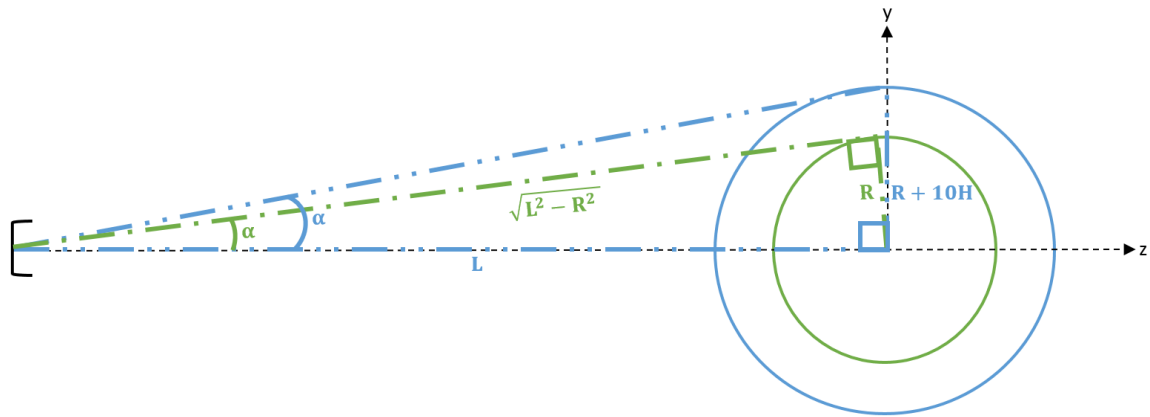


Figure 2.11: Shows the angular limits which compose the check performed on each light ray before it is propagated. The green solid line is the Earth's surface; green dash-dot is the triangle which defines the angle at which the light ray hits the surface. The blue solid line is the Earth's atmosphere; blue dash-dot-dot is the triangle which defines the angle at which the light ray just intercepts the atmosphere.

The z_{start} and α_1, α_2 values are created so that these limits should not be overstepped, but they exist as a fail-safe. When the light ray at its specific angle completes the angle limit check, it then propagates along the z -axis following the same procedure as for the single ray described in the previous section. Each ray continues until it either hits the Earth's surface or exits the atmosphere. When all the light from the lens of the atmosphere is counted, the result is a thin ring, shown in Figure (2.12). Since the result of our 'Angle Array' code is always a thin ring of

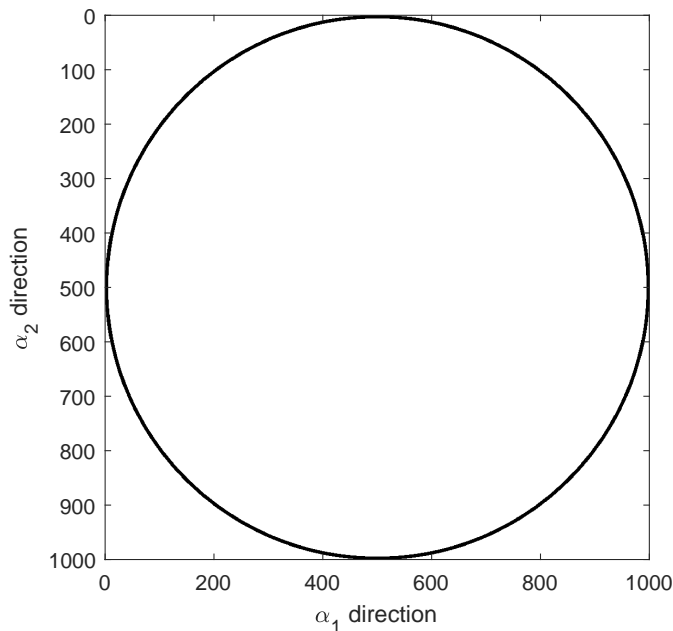


Figure 2.12: Graph of a Boolean matrix showing where the light rays successfully pass through the atmosphere and into the detector. If a ray never enters the atmosphere or hits the Earth, its value is set to 0, and thus it does not appear on this plot. The resulting ring shape is due to the atmosphere's spherical shell shape. The grid is 1000-by-1000 because there are 1000 rays propagated in each direction, resulting in a total of 1,000,000 rays in the grid. Not all of them pass through the atmosphere—in this case, 20,220, or 2.02%.

light, we constructed a code to only propagate the rays which lie in this ring. The procedure is outlined in the following section.

2.2.3. Thin Ring

The thin ring with only 2.02% of the total rays ending up in the detector confirmed that the relevant light for this code only spans a thin layer. Thus, it is computationally cheaper to analytically calculate this layer and only model those rays within it. This is achieved by breaking up the ring into four different pieces— seen in Figure (2.13)— with each piece defined by a separate section of code. In each section, first the α_1 range and then the α_2 range is specified. This range varies from the inner circle (α_{min}) to the outer circle (α_{max}). Typically, for the minimum we choose:

$$\alpha_{min} = R/L \quad (2.52)$$

which is the angle to the Earth's surface. For the maximum we choose:

$$\alpha_{max} = \frac{R + 10H}{L} \quad (2.53)$$

which is the angle to the top of the Earth's atmosphere. The four separate sections of code which describe the four different pieces are given by Equations (2.54), (2.55), (2.56), and (2.57).

$$1. \quad \alpha_1 : -\alpha_{max} \rightarrow -\alpha_{min} \quad (2.54)$$

$$\alpha_2 : -\sqrt{\alpha_{max}^2 - \alpha_1^2} \rightarrow \sqrt{\alpha_{max}^2 - \alpha_1^2}$$

$$2. \quad \alpha_1 : -\alpha_{min} \rightarrow \alpha_{min} \quad (2.55)$$

$$\alpha_2 : -\sqrt{\alpha_{max}^2 - \alpha_1^2} \rightarrow -\sqrt{\alpha_{min}^2 - \alpha_1^2}$$

$$3. \quad \alpha_1 : -\alpha_{min} \rightarrow \alpha_{min} \quad (2.56)$$

$$\alpha_2 : \sqrt{\alpha_{min}^2 - \alpha_1^2} \rightarrow \sqrt{\alpha_{max}^2 - \alpha_1^2}$$

$$4. \quad \alpha_1 : \alpha_{min} \rightarrow \alpha_{max} \quad (2.57)$$

$$\alpha_2 : -\sqrt{\alpha_{max}^2 - \alpha_1^2} \rightarrow \sqrt{\alpha_{max}^2 - \alpha_1^2}$$

After the light traverses the atmosphere, we save the final angle as a position on a two dimensional array. Since there are over one million rays for each run, we group the angles into smaller bins so that neighboring rays all take on one position. If the Terrascope successfully amplifies the light of a celestial object, then most of the rays will be concentrated at the center, constituting a point-source. Thus, we call the graph of this final outcome a Point Spread Function. It is expanded upon in Chapter 3.6.

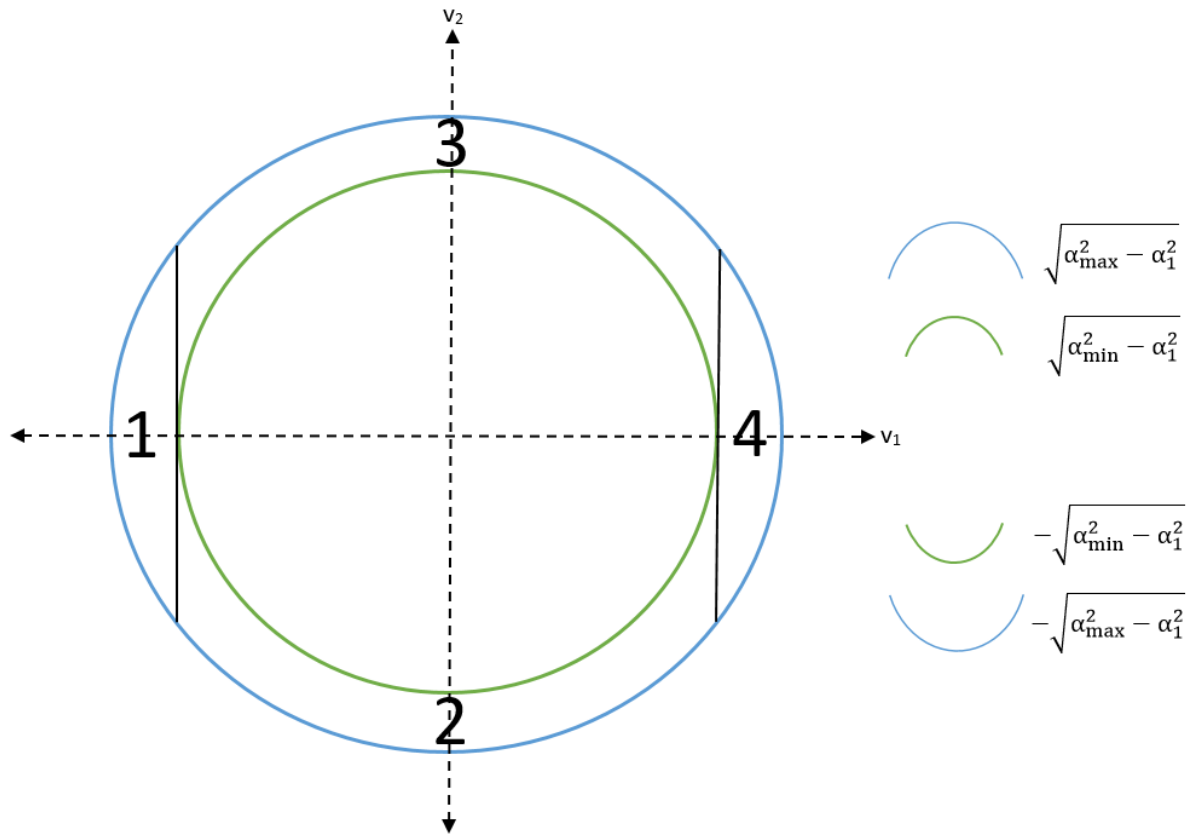


Figure 2.13: Four pieces of the thin ring code corresponding to Equations (2.54), (2.55), (2.56), and (2.57). Again, green denotes the Earth's surface and blue denotes the top of the atmosphere, not to scale. The expressions on the right describe the α_2 part of the aforementioned equations; note that they are rearranged versions of the inner (green) and outer (blue) circles. Inner: $\alpha_{\min}^2 = \sqrt{\alpha_1^2 + \alpha_2^2}$. Outer: $\alpha_{\max}^2 = \sqrt{\alpha_1^2 + \alpha_2^2}$.

2.3. Model Outputs

Although different in the number of light rays in the system, each of the above outlined codes is propagated in the same way and yields the same result. They vary in data output, but in total, they are capable of giving the following:

- **Final Angle:** final angle at which light ray exits the atmosphere
- **Bending angle:** total angle bent by light ray from entrance to exit of atmosphere
- **Minimum altitude:** lowest point in the atmosphere traveled by light ray
- **Coherence Length:** measure of resolution of rays entering the detector
- **Survival Probability after Rayleigh Scattering:** chance that the light ray will reach the detector after bouncing off particles in the atmosphere
- **Survival Probability after Ozone Absorption:** chance that the light ray will reach the detector after being absorbed by ozone layer particles in the atmosphere
- **Point Spread Function:** measure of usefulness of light rays (in terms of amplification and resolution) once they reach the detector

The last four outputs will be expanded upon in Chapter 3.

3

Atmospheric Effects

In order to correctly assess the usefulness of the Terrascope, we must make the atmosphere through which light passes as realistic as possible. Or, if inputting all characteristics of the atmosphere is not feasible, we strive to implement those which will affect the light the most. Thus, if our results are overwhelmingly positive even in the "worst-case scenario", then we can be confident that the Terrascope is a potentially useful tool for astronomical observations. In the section below, we describe the atmospheric effects which we imposed on the light in our Terrascope model and their results on the quality of the apparatus.

This chapter is divided into five sections, of which the first is an overview of the Earth's atmosphere. The following three sections detail three different ways in which the atmosphere effects light. The fifth section combines the effects to look at the overall state of the light which reaches the detector. Of underlying importance in this last section is the amount the light has been amplified and the degree to which it is still coherent despite the effects. All sections, with the exception of the first, are split into three subsections:

1. **Theory:** theoretical background about the effect; governing equations; relevant literature
2. **Implementation:** how the effect is modeled by our Terrascope; from analytical equations to numerical simulation
3. **Results:** graphical representation of how the light is affected with accompanying description and analysis

In the Results subsection, many of the graphs are parameterized on L (distance between Earth and detector) and λ (wavelength), meaning that results are measured in terms of these variables. These two parameters were chosen because they are the two major adjustable variables—adjustable because humans can choose detector distance and observation wavelength—upon which the effects and Terrascope outcome depend. The ranges chosen for L and λ were based on the values chosen by Kipping and also based on available relevant data. In each Results subsection, we show three graphs: (1) effect versus minimum altitude reached by a

light ray, parameterized on λ (2) effect versus L , parameterized on λ , and (3) effect versus λ , parameterized on L .

3.1. Earth's Atmosphere

The premise of the Terrascope lies in the propagation of light through the Earth's atmosphere; thus, an understanding of the make-up and properties of the atmosphere is essential. Earth's atmosphere extends about 100km above the surface and consists of mostly N_2 and O_2 . Other substances include: Argon (Ar), Carbon Dioxide (CO_2), Neon (Ne), Helium (He), Methane (CH_4), Krypton (Kr), and water vapor (H_2O) [21]. In the above section on refraction, it was stated that the atmosphere becomes less dense as it increases in altitude. Density is an important parameter for determining how light behaves in the atmosphere—two others are temperature and pressure. All three parameters are dependent upon the others. Air pressure is caused by the weight of the molecules above it and decreases with increasing altitude. Density has a similar scaling to pressure because they are proportional [7]. The decrease is also due to the ground being the main absorber of sunlight and then emitter of heat energy via infrared (IR) light back into the air. With one exception (the stratosphere), the farther from the ground, the colder it is. Figure (3.1) shows more detail about how temperature, pressure, and height scale in the atmosphere.

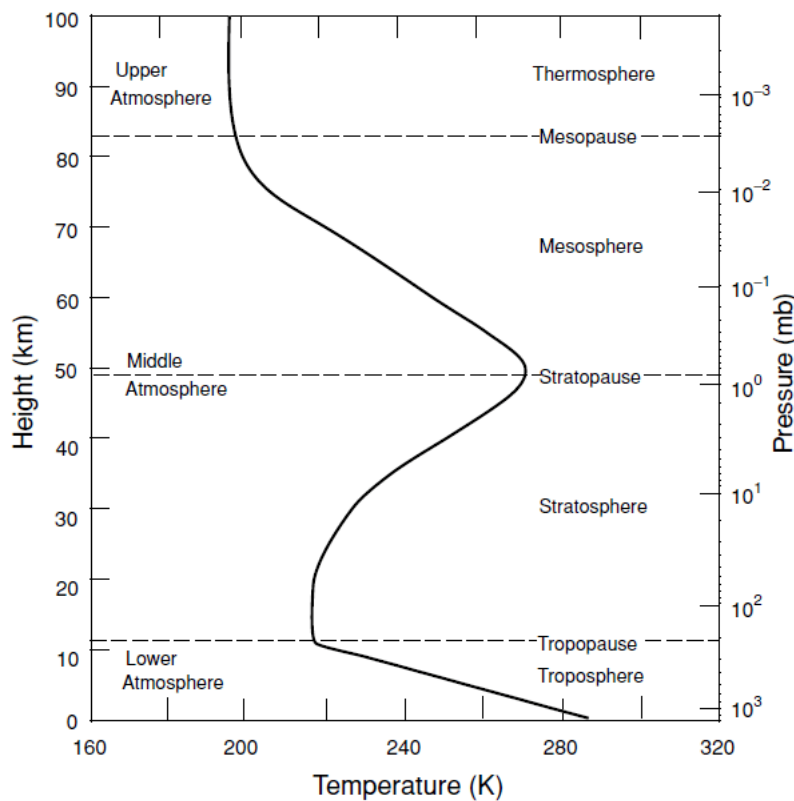


Figure 3.1: Relationship between altitude, temperature, and pressure. Density scales as pressure. Pressure units shown are millibars; one bar is defined as the pressure at sea-level. [42].

Note that the atmosphere is divided into subsections called "spheres" with the boundaries called "pauses". These are briefly described below [38].

- **Troposphere:** It is warmed by visible light from the Sun, convection, and IR light emitted from the surface, but temperature decreases with increasing altitude. This is where weather occurs and where most clouds are, due to the highest proportion of water vapor. The maximum height of this section varies with location, with it increased over warmer areas and lower over colder ones. The tropopause holds the jet stream and is the highest point for weather.
- **Stratosphere:** Visible and ultraviolet (UV) light from the Sun reach here. Temperature decreases with increasing altitude in the lower part and increases with increasing altitude in the upper part. This is due to the ozone layer in the upper part. The ozone layer holds ozone molecules (O_3) which absorb UV light and turn it into heat, heating the layer. The stratosphere is less turbulent than the troposphere, so airplanes fly in the lower part.
- **Mesosphere:** Visible, UV, and X-Ray light reach here. Temperature decreases with increasing altitude. The coldest atmospheric temperatures are at the top of this layer. Most meteors burn up in this layer.
- **Thermosphere:** Visible, UV, and X-Ray light reach here and ionize gases. The temperature increases with increasing altitude because it is heated by the Sun's light. Temperature varies with the light (energy) coming from the Sun. Aurorae occur here.
- **Exosphere** (not pictured): Similar to the thermosphere in terms of light and temperature. This is where the Earth's atmosphere gradually turns into outer space.

These layers are important to keep in mind in the following sections because light from celestial objects enter, travel through, and emerge from the Earth's atmosphere at different altitudes. The properties of the atmosphere vary with these heights, and thus the lights' passage and interaction will also vary.

On a smaller scale, there are interactions with atoms, molecules, and particles in the atmosphere. While the majority of these components are completely gaseous, others are aerosols, liquids and solids suspended in gas. It is important to know the chemical make-up, size, concentration, and other properties of these materials in order to determine how they influence the propagation of light in the atmosphere [6]. Table (3.1) lists the gases by percentage in the atmosphere; Table (3.2) lists the gases by atmospheric height.

In addition to the chemical make-up of Earth's atmosphere, clouds exist which influence the light passing through. Clouds form when air rises, expands, and cools. The initial rising air can be air heated by the Earth's surface, air forced upward by elevation, air forced upward by an area of low pressure, or weather fronts (when large masses of cold and hot air collide). When the cooled air drops to and falls below the dew point, the water vapor in the air condenses—changes into a liquid—on condensation nuclei [6]. These nuclei are actually particles of dust, pollen, salt or other materials which make it easier for the water vapor to turn into a water

Name	Chemical Formula	Concentration (% by volume)
Nitrogen	N ₂	78.08
Oxygen	O ₂	20.95
Water Vapor	H ₂ O	$2 \times 10^{-6} - 3 \times 10^{-2}$
Argon	Ar	9.34×10^{-3}
Carbon Dioxide	CO ₂	3.45×10^{-4}
Neon	Ne	18.2×10^{-6}
Helium	He	5.24×10^{-6}
Methane	CH ₄	1.72×10^{-6}
Krypton	Kr	1.14×10^{-6}
Hydrogen	H ₂	5.0×10^{-7}

Table 3.1: List of ten gases in the atmosphere with the highest volumetric concentration.

Altitude (km)	Concentration (% by volume)					
	N ₂	O ₂	O	He	Ar	H
100	77	19	3.4	<0.05	0.8	<0.05
150	61	5.6	24	<0.05	0.1	<0.05
200	42	3.0	55	0.01	<0.05	<0.05
300	17	0.8	81	0.8	<0.05	<0.05
400	6.0	0.2	91	2.7	<0.05	<0.05
500	1.9	<0.05	90	8.2	<0.05	0.2
700	0.1	<0.05	55	43	<0.05	1.6
1000	<0.05	<0.05	5.7	88	<0.05	6.7

Table 3.2: How the concentration of certain gases in the atmosphere vary with altitude.

droplet. In addition to liquid water, ice crystals can form on the particles. The particles are small enough in size and therefore have a small enough mass to remain suspended [4]. Liquid and solid matter contained in the atmosphere are called aerosol particles. They differ by size, chemical composition, water content, and fall velocity. Different types of clouds are made of different particles and have different properties (mass/amount of particles, temperature, ratio of liquid to solid particles, and number density), thus each type affects light in its own way. Figure (3.2) shows a graph of clouds by altitude and temperature.

The composition of the Earth's atmosphere determines how light interacts as it passes through. Depending on the particle with which a light ray interacts and the circumstances of the interaction, the light can scatter (bounce), diffract (bend), be absorbed, or be transmitted. In our Terrascope, we consider diffraction due to turbulence, which can occur around clouds or elsewhere; scattering due to small particles in the atmosphere, like those listed in Tables (3.1) and (3.2) and absorption due to the ozone layer seen in the stratosphere of Figure (3.1). The the-

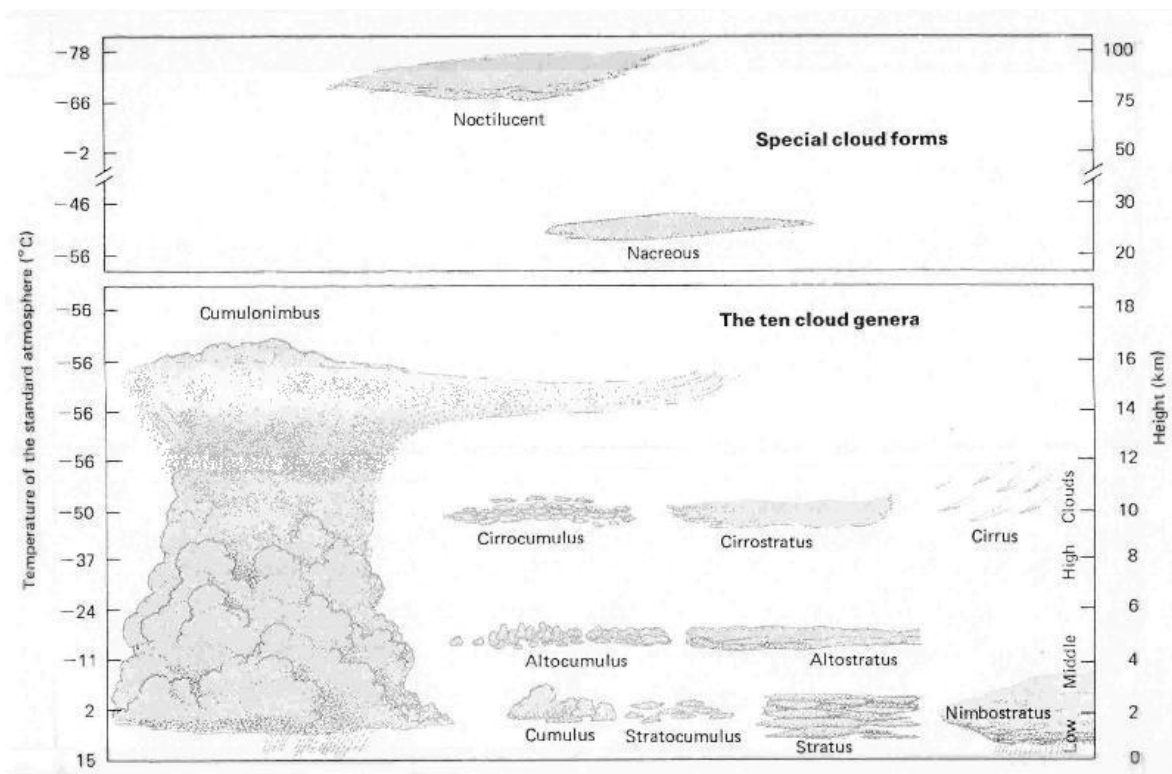


Figure 3.2: Different types of clouds, their altitudes, and the temperature at that altitude [30]. Clouds at higher altitudes are made of ice crystals, whereas clouds at lower altitudes are made of liquid water droplets. The transparency of the cloud reveals how full of moisture it is; the more transparent, the less moisture. In particular, cirrostratus, altostratus, stratocumulus, and nimbostratus hold large amounts of moisture.

ory behind these phenomena, how we incorporated them into our Terrascope, and our findings are outlined in the following sections.

3.2. Turbulence

3.2.1. Theory

Greek philosopher scientist Aristotle noticed the effects of turbulence on the appearance of stars, and referred to their twinkling as stellar "scintillation". Tycho Brahe in the 16th century was the first person to suggest that the cause was at least partly atmospheric. When telescopes were invented, astronomers noticed that telescopic observations were more distorted (less clear) than theoretical calculations predicted. When observations were made at certain locations, such as mountain tops, these detrimental affects decreased. It was not until 1665 that Robert Hooke introduced the refraction theory of scintillation, citing "moving regions of atmosphere [with] different refracting powers which act like lenses" as the cause of the turbulent motions which had been observed for thousands of years [12].

Turbulence can have a multitude of effects on the appearance of an object, including: varying brightness, displacement from actual position, smearing out, continuous motion about an approximate center, long lasting/far moving oscillations, changing size, and pulsating irregular changes in illumination [34]. These effects are caused by fluctuations in the index of refraction of the air, which causes the light to bend differently, and chaotically. Turbulence is the cause of these fluctuations, and can be viewed as instability in a fluid flow which occurs at a high Reynold's number, Re , defined as [19]:

$$Re = \frac{L_0 u}{\nu} = \frac{L_0 u \rho}{\mu} \quad (3.1)$$

Where:

- L_0 : characteristic length, which defines the scale of the system
- u : characteristic velocity, which defines the flow speed of the fluid
- ν : kinematic viscosity, the ratio of viscosity to density $\left(\frac{\mu}{\rho}\right)$
- ρ : density
- μ : viscosity

Additional properties of turbulence include: (1) irregularity and randomness, (2) diffusivity (causes increased momentum, heat, and mass transfer rates), (3) fluctuating vorticity (spinning motions), and (4) dissipation if not continually supplied with outside energy (kinetic energy of turbulence is transferred to the internal energy of the fluid) [41].

Turbulence in the atmosphere is caused by wind over obstacles and by differences in pressure, temperature, humidity, and velocity in the air. Laminar—"smooth"—air becomes turbulent, characterized by swirling eddies, as seen in Figure (3.3) [36]. These eddies are at first large, on the scale of tens of meters, but then break down into smaller and smaller eddies, on the scale of millimeters, seen in Figure (3.4). The larger scale, L_0 , is called the outer scale, while the smaller scale, l_0 , is called the inner or damping scale. The varying scales in the middle are called spatial scales, l [35]. The phenomena of this progressive down-scaling is called a "tur-

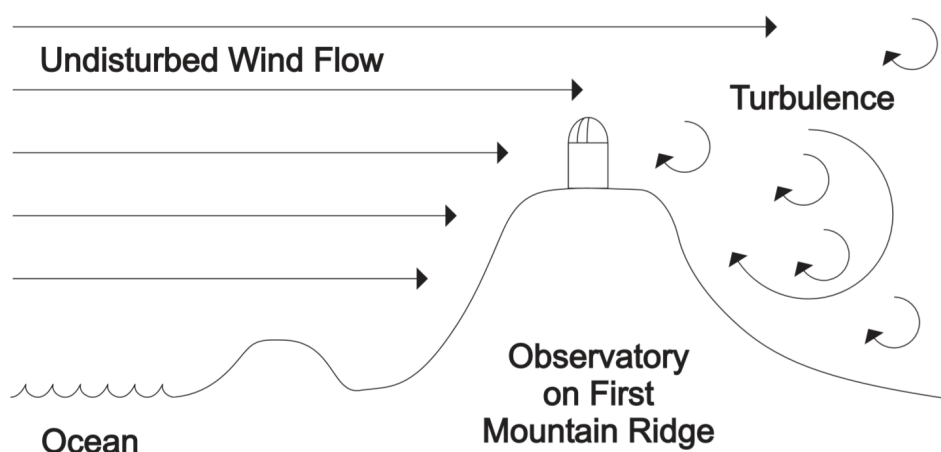


Figure 3.3: Undisturbed, or laminar, flow comes off the ocean and becomes turbulent once it encounters the mountain. To decrease seeing, observatories are placed not only on high altitudes (in order to look through less atmosphere), but on the first mountain ridge near the ocean (in order to get the undisturbed ocean winds) [36].

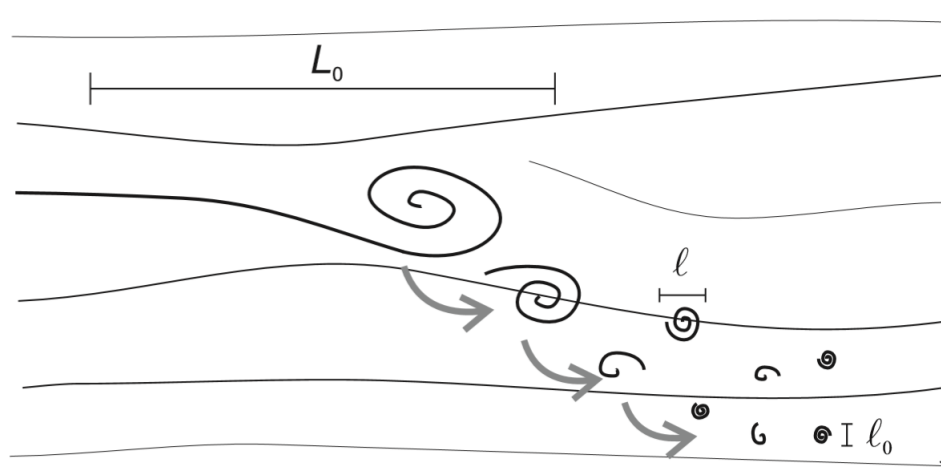


Figure 3.4: From the largest scale eddy, $L_0 \sim 10\text{m}$, down to the smallest, $l_0 \sim 1\text{mm}$ [35].

bulent cascade” [13]. The kinetic energy of the large scale motions transfers into the energy of the many small scale motions, until the viscosity of the fluid prevents successive break-downs. At this length, called the dissipation scale L_v , since the eddies cannot break down further, the energy begins converting into internal energy. The cascade of eddies can be defined in terms of an energy dissipation or flow rate, called Kolmogorov’s law for turbulence [13]:

$$E(k) = C\varepsilon^{2/3}k^{-5/3} \quad (3.2)$$

Where:

- $E(k)$: energy stored in each k-mode per gram of gas
- k : in units of $\frac{1}{\text{length}}$, this defines a new space, called k-space, which enables describing the eddy cascade from small to large k
- C : constant, approximately equal to one
- ε : energy flow

This definition stems from Kolmogorov's theory of turbulence which will be used in the formalism that follows. From Equation (3.2), it can be determined that the time scale of eddy motions is proportional to the size of the eddies, with the relationship:

$$\tau_{eddy} = \varepsilon^{-1/3} l^{2/3} \quad (3.3)$$

Additionally, the equation for the dissipation scale becomes:

$$L_v = \left(\frac{v^3}{\varepsilon} \right)^{1/4} \quad (3.4)$$

To continue into the theory of how turbulence affects light waves (the effects are, in fact, due to the wave characteristics of light), the notion of a structure function must be introduced. These are used to describe the spatial structure of a random process. In general, a structure function, $D_x(R_1, R_2)$, is defined as [36]:

$$D_x(R_1, R_2) = \langle |x(R_1) - x(R_2)|^2 \rangle \quad (3.5)$$

Where:

- R_1 : position one
- R_2 : position two
- x : variable which is being considered and measured at the two positions

This equation yields the expected value of the difference between x as it is measured at R_1 and at R_2 . The fluctuating variables considered here in turbulence calculations are velocity and refractive index. Their structure functions are given in Equations (3.6) and (3.7) [36].

$$D_u(R_1, R_2) = C_u^2 \cdot |R_1 - R_2|^{2/3} \quad (3.6)$$

$$D_n(R_1, R_2) = C_n^2 \cdot |R_1 - R_2|^{2/3} \quad (3.7)$$

Where:

- C_u^2 : velocity structure constant defining the turbulence strength, $C_u^2 = k\varepsilon^{2/3}$
- C_n^2 : refractive index structure constant, $C_n^2 = \frac{7.8 \times 10^{-5} P}{T^2} C_T^2$

Turbulence causes differences in temperature which alters density, and which in turn alters the refractive index. When light waves travel through turbulent regions, specifically one of thickness δh , they undergo a phase shift. This can be defined using a structure function as well:

$$D_\phi(R_2 - R_1) = 2.914 \left(\frac{2\pi}{\lambda} \right)^2 \delta h C_n^2 (R_2 - R_1)^{5/3} \quad (3.8)$$

Note that the phase structure function depends on the refractive index structure constant. We can define how turbulence affects an image also using the refractive index structure constant.

This is called the Fried parameter, r_0 [13]:

$$r_0 \equiv \left(0.423 \left(\frac{2\pi}{\lambda} \right)^2 \sec \xi \int_0^\infty C_n^2(z) dz \right)^{-3/5} \quad (3.9)$$

Where:

- ξ : zenith angle
- z : altitude
- $C_n^2(z)$: altitude dependent refractive index structure constant

This definition of r_0 describes the length for which errors in the wave phase are on the order of one radian. If the seeing conditions are characterized by r_0 and a long exposure image is taken, the image quality is approximately equal to the image taken by a telescope with diameter r_0 . For the purposes of Terrascope research, the definition of r_0 would have to be adjusted to integrate along a light ray, rather than its current form along the entire atmosphere at some angle to the zenith. Adjustments include: taking out the secant of the zenith angle, changing z to be the position (independent variable for the structure constant), and dz to the path length. These changes are necessary because the Fried parameter is an important variable in turbulence calculations and the remainder of the definitions rely on it. The phase structure function can be redefined in terms of the Fried parameter, as seen in Equation (3.10). Additionally, the coherence function of the wave front is introduced as Equation (3.11), also in terms of the Fried parameter. Wave coherence is essential for production of a clear image, and many times, turbulence is the cause of decoherence [36], [13].

$$D_\phi(R_2 - R_1) = 6.88 \left(\frac{R_1 - R_2}{r_0} \right)^{5/3} \quad (3.10)$$

$$B_\psi(R_1 - R_2) = \exp \left[-3.44 \left(\frac{R_1 - R_2}{r_0} \right)^{5/3} \right] \quad (3.11)$$

Equation (3.9) suggests that the Fried parameter is wavelength dependent. It has the following scaling law:

$$r_0 \propto \lambda^{6/5} \quad (3.12)$$

Thus, longer wavelengths yield better quality images. Lastly, this analysis only holds for turbulent layers smaller than the Fresnel length, d_F :

$$d_F = \frac{r_0^2}{\lambda} \quad (3.13)$$

When the layers are optically thicker, which typically occurs at short wavelengths, large zenith angles, and poor observing sites, the light is heavily diffracted (bent). One consequence of this diffraction is scintillation, the twinkling of stars that was initially observed and led to theories of turbulence.

3.2.2. Implementation

As seen in the previous section, there are multiple ways to measure the turbulence and its effects on light in the atmosphere. For the purposes of our Terrascope, we chose to calculate the Fried parameter in order to have a sense of image quality. Our modified version of Equation (3.9) is:

$$r_0 = \frac{1}{k} \left(0.423k^{1/3} \int_{z_{\text{start}}}^{z_{\text{end}}} C_n^2(z) dz \right)^{-3/5} \quad (3.14)$$

Where

- k : wavenumber, $k = \frac{2\pi}{\lambda}$
- z : altitude
- dz : step size along the z -axis path

Note that we have made the necessary adjustments from Equation (3.9) in order to fit our situation. The integration is performed along the ray of light from z_{start} , calculated in Equation (2.38), to z_{end} , calculated when the ray exits the atmosphere via Equation (2.40). Integration is simulated by using a Riemann sum inside the z -loop. Each step, representing the ray's position along the z -axis, $C_n^2(z)dz$ is calculated and added to the previous step. At the end of the z -loop, after the ray has finished its journey, the final value is multiplied by the remaining values in Equation (3.14). We are able to execute this multiplication outside of the loop because only C_n^2 is inside the integration, while the rest of the terms are outside. This final value yields our coherence length.

For C_n^2 , we chose a best-fit model rather than a table of experimentally derived values— this is for ease of discretization and calculation. The integral in Equation (3.14) depends on altitude and the step size of the z -loop. Thus, if we were to use a table of values for C_n^2 , we would need an interpolation function to interpolate between altitudes based upon the step size. Instead, we use an existing model— created to fit experimentally obtained data— which has altitude as its input and C_n^2 as its output. We wrote the model as a function and called it every z -step. It is called "Clear I Night Model" and is given by Equation (3.15) [2]. Figure (3.5) shows the plot of Clear I Night.

$$\log_{10}(C_n^2) = \begin{cases} -10.7025 - 4.3507z + 0.8141z^2 & \text{for } 1.23 < z \leq 2.13 \\ -16.2897 + 0.0335z - 0.0134z^2 & \text{for } 2.13 < z \leq 10.34 \\ -17.0577 - 0.0449z - 0.0005z^2 \\ \quad + 0.6181 \exp\left(-0.5 \left(\frac{z-15.5617}{3.4666}\right)^2\right) & \text{for } 10.34 < z \leq 30 \end{cases} \quad (3.15)$$

A higher C_n^2 value indicates more turbulence and a lower coherence length of light. After coherence length is calculated from C_n^2 , we then calculate by what amount the reduced coherence length causes the light ray to diffract (bend). We consider diffraction in terms of the how much the original light spreads out, which is measured as a cone of angular size $\frac{2\pi}{\lambda} \alpha_{\text{diffrac}}$.

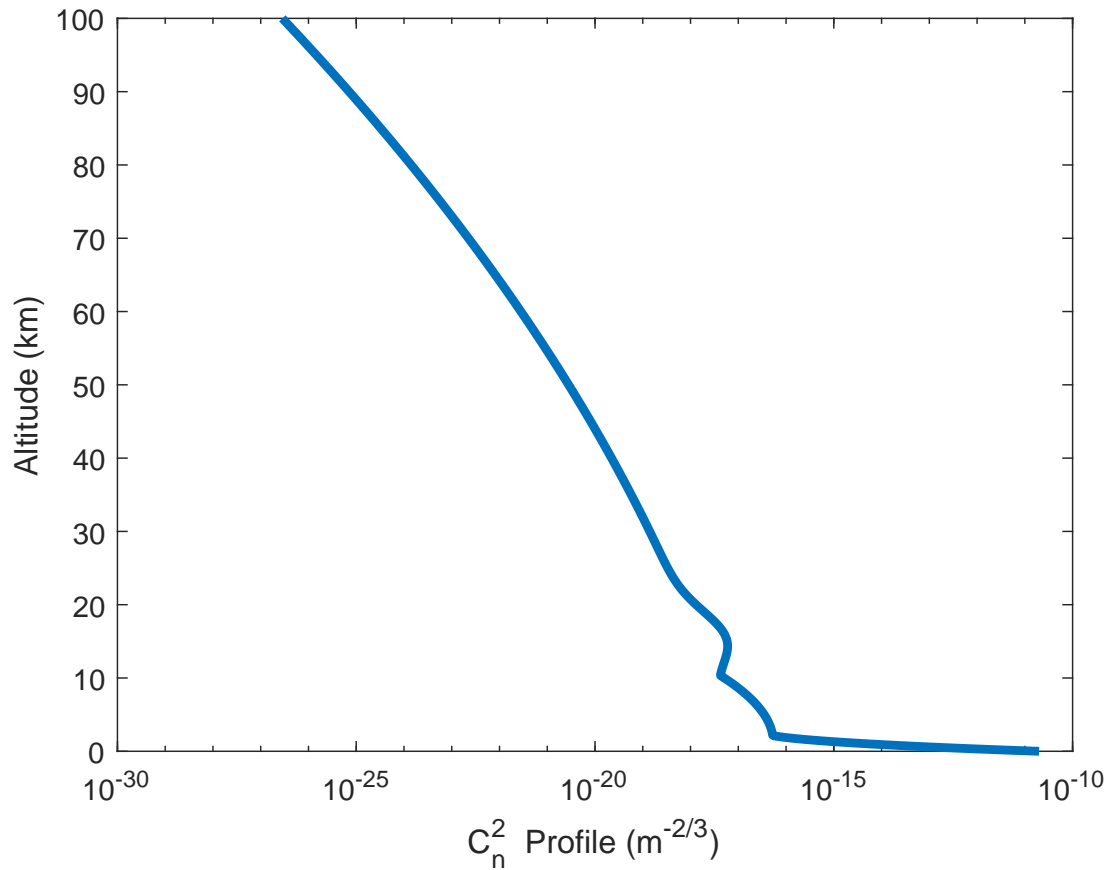


Figure 3.5: Profile of a refractive index structure constant. This model is called Clear I Night, so-called because it was based on measurements taken in the desert night of New Mexico in 1993. We used the nighttime measurements because the detector would only detect light from the night side of the Earth; the day side has too much bounced light from the Sun. The model measurements were "made under fairly homogeneous meteorological conditions" [2]. These measurements and their corresponding model, compared to the other models made by the creator of Clear I Night, have more turbulence in the lower part of the atmosphere, specifically below 10km. As stated in the text, we implemented our Terrascope with elements that would be the most disruptive to test its abilities in the worst-case, yet still realistic, scenarios.

To see how this spreading affects the total intensity of light reaching the detector, we broaden the light of the ray by a two-dimensional Gaussian. The two dimensions are for the x and y direction and we call the resulting broadening the deflection angles $\Delta\alpha_1$ and $\Delta\alpha_2$. They are calculated by [37]:

$$\Delta\alpha_1 = \frac{1}{kr_0} \sqrt{-2 \ln(1-q)} \cos(2\pi p) \quad (3.16)$$

$$\Delta\alpha_2 = \frac{1}{kr_0} \sqrt{-2 \ln(1-q)} \sin(2\pi p) \quad (3.17)$$

Where:

- p : random number between 0 and 1
- q : random number between 0 and 1

Finally, the total diffraction– light bending– due to turbulence is calculated as:

$$\alpha_{1\text{diffrac}} = \alpha_{1\text{final}} + \Delta\alpha_1 \quad (3.18)$$

$$\alpha_{2\text{diffrac}} = \alpha_{2\text{final}} + \Delta\alpha_2 \quad (3.19)$$

3.2.3. Results

In this section, we present and interpret results of coherence length from runs of our Terrascope model.

Figure (3.6) shows that the coherence length is dependent upon both the minimum altitude and the wavelength of the light ray. Both variables have a proportional relationship to the coherence length, seen numerically in Equation (3.14). We can interpret the results in the following way: the higher the minimum altitude, the less deep into the atmosphere the light travels, the less turbulent the air it passes through, the longer the coherence length, and thus the sharper the image. For the wavelength: the higher the wavelength, the smaller the phase shift it undergoes in a turbulent medium (Equation (3.8)), the longer the coherence length, and thus the sharper the image. Figure (3.6) is useful for showing how the path of a light ray through the atmosphere effects the coherence length, but ultimately, we want to know how the coherence length changes with a variable which we can control. Thus, we use the minimum altitude measurements to calculate the corresponding L values, and evaluate the coherence length's dependence on that variable.

Figure (3.7) shows that coherence length also has a proportional relationship to L . This is not surprising, considering Figure (2.8) shows that minimum altitude and L are proportional (this relationship can also be seen in Appendix A). Thus, if longer coherence lengths are present for high minimum altitudes, they will also be present for large L values. For the largest L tested here, which is almost four times the distance to the Moon, the coherence length for our highest wavelength is about .13m or 13cm. For comparison, the ground-based European Extremely Large Telescope (E-ELT), which will be 42m in diameter, when observing at wavelength of 1000nm, will have a coherence length of .2m or 20cm in good condition [46].

Finally, Figure (3.8) is the inverse of Figure (3.7). It provides a more detailed view of the coherence length's dependency on λ , confirming that the relationship is proportional. The trend lines suggest that as the wavelength continues to increase beyond the values we tested, the coherence length would increase as well. It is beginning to appear that in terms of coherence length, which determines image resolution, our Terrascope is not suitable for the visible light range. Rather, it is better put to use at higher wavelengths, such as infrared, microwaves, and radiowaves. However, we must first assess what effect scattering and absorption have on the Terrascope.

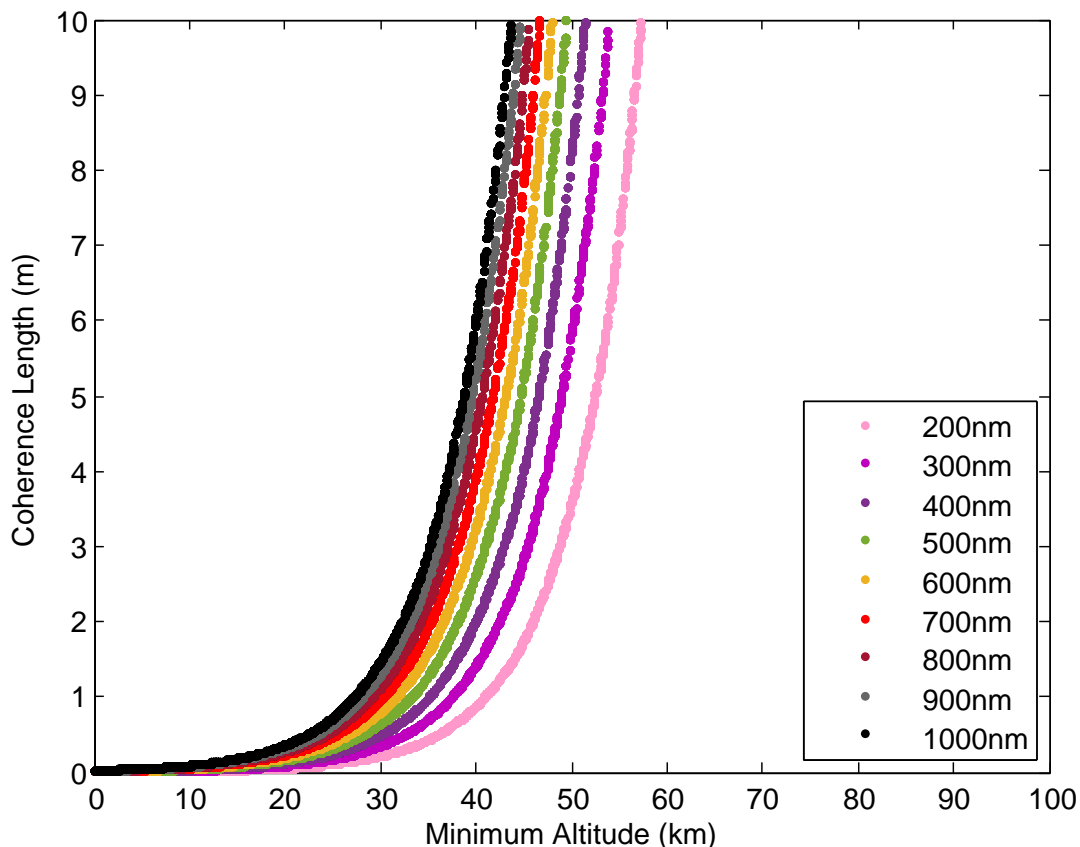


Figure 3.6: Plot of coherence length versus the lowest height that each light ray reaches in the atmosphere, for nine different wavelengths. This graph was made using the 'Angle Array' code. The lower the ray reaches in the atmosphere, the shorter the coherence length. This is because there is more turbulence in the lower atmosphere, as shown in Figure (3.5). Thus, when light reaches lower levels, it goes through more areas where it is bent due to the constantly changing indices of refraction. It is also because rays which reach lower in the atmosphere have a longer path through the atmosphere, so the light travels through a higher amount of turbulent air. This is shown in Figure (2.8). Additionally, for longer wavelengths, there is a weaker proportional relationship between minimum altitude and coherence length. For example, the 1000nm light rays have a longer coherence length at a lower minimum altitude than the light rays at 200nm. This relationship can be seen in Equations (3.14) and (3.12), where coherence length is proportional to wavelength. As the wavelength increases, so does the coherence length.

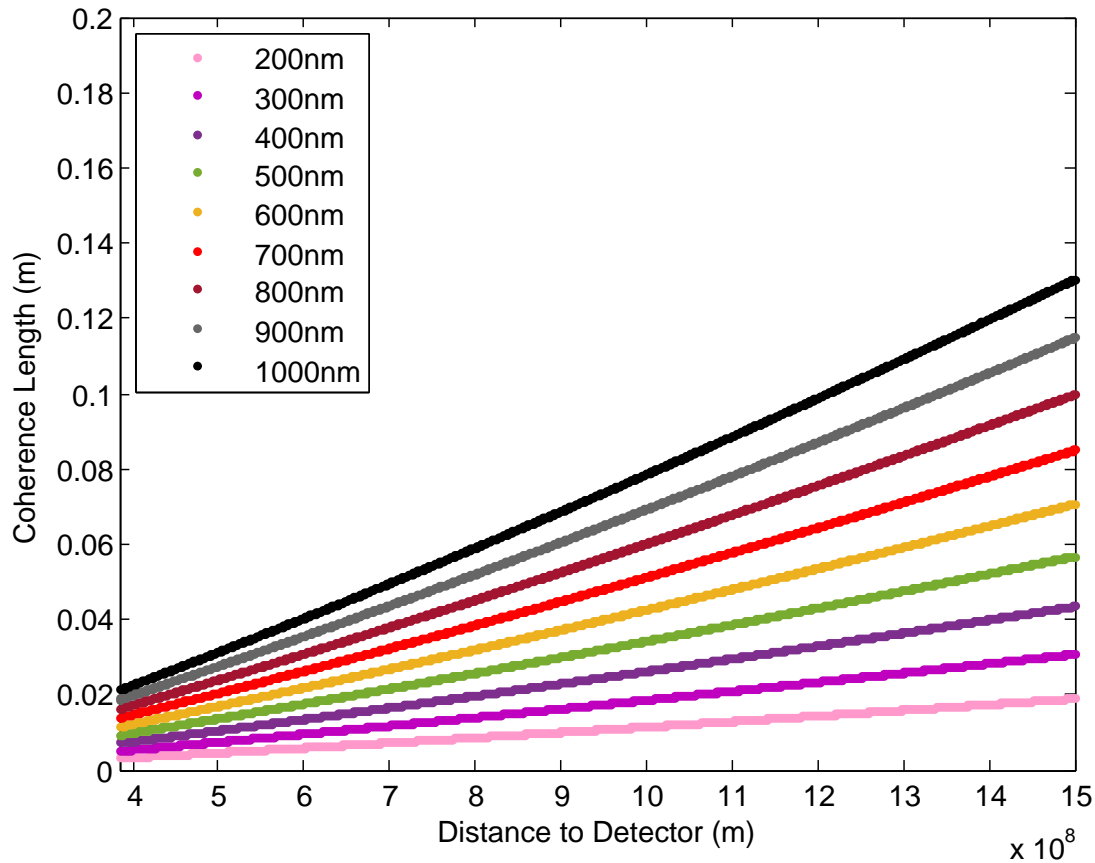


Figure 3.7: Plot of coherence length versus the distance from Earth's center to the detector, L , for nine different wavelengths. This graph was made using the 'Single Ray' code. The minimum value is the distance to the Moon and the maximum is one Hill radius. This is a stationary location between the gravitational pulls of the Sun, Earth and the Moon. This figure is consistent with Figure (3.6) because, as seen in Figures (2.8), (A.1) and (A.2), the smaller the L , the lower the minimum altitude. Thus, the same behavior observed for coherence length vs. minimum altitude would be observed for coherence length vs. L . The larger the L , the larger the coherence length, and thus the image of the celestial object behind the Earth will be higher resolution.

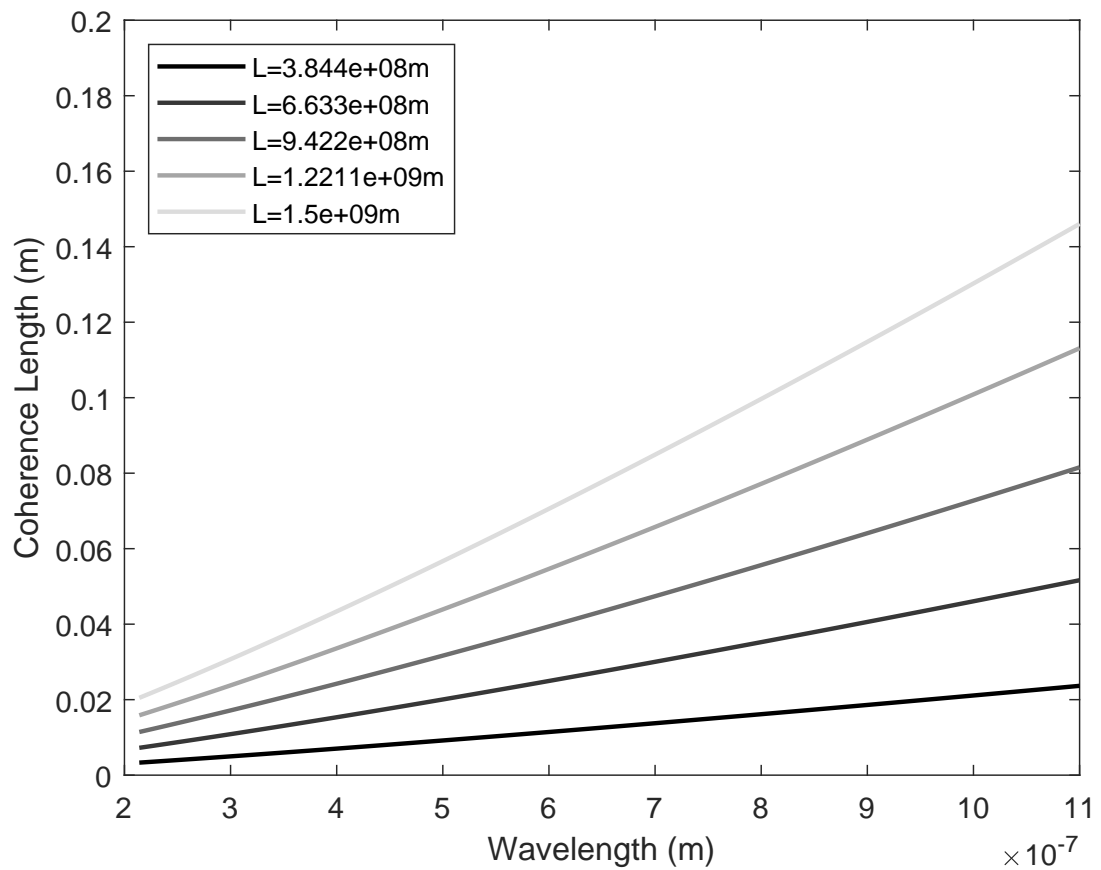


Figure 3.8: Plot of coherence length versus light wavelength, for five different L values. This graph was made using the 'Single Ray' code. It contains the same information as Figure (3.7), but is shown in a different way. Figure (3.7) is useful for continuous detailed behavior of coherence length as a function of L ; this one has the same usefulness as a function of λ . Following the trend lines on this graph, if we were to use even higher wavelengths, the coherence length would continue to increase.

3.3. Rayleigh Scattering

3.3.1. Theory

Scattering is the phenomenon of light interacting with an obstacle and being redirected onto new paths which can go in different directions. This process has two parts: (1) the excitation of the charges in the obstacle by the photon and (2) the subsequent reradiation of a photon by the charges [3]. The type of scattering depends upon the ratio of the radius, r , of the molecule to the incoming light's wavelength, λ [26]. This ratio is called the size parameter, s :

$$\begin{aligned} s &= \frac{2\pi r}{\lambda} \\ &= kr \end{aligned} \tag{3.20}$$

Scattering can be broken down into the following categories:

- **Elastic Scattering:** the photon's kinetic energy is conserved, thus the wavelength of the scattered light is the same as the wavelength of the incident light
 - **Mie Scattering:** Light wavelength is same size as the particles, $s \sim 1$. Only for spherical particles. Occurs mostly in the low atmosphere and when clouds are abundant. Examples of the particles are dust, pollen, smoke, and water vapor. Scattering intensity is mostly independent of wavelength, but dependent on particle size (the larger the particle, the more forward scattering).
 - **Rayleigh Scattering:** Light wavelength is much larger than the particles, $s \ll 1$. For spherical and non-spherical particles. Examples of the particles are small dust particles and nitrogen and oxygen molecules. Scattering intensity is inversely proportional to the wavelength's fourth power.
- **Inelastic (Raman) Scattering:** the photon's kinetic energy is not conserved, thus the wavelength of the scattered light is different than the wavelength of the incident light

Additionally, there is a distinction between single scattering and multiple scattering. The former is defined as a photon scattering once and is common in optically thin media; the latter is defined as photon scattering more than once and is common in optically thick media. Single scattering is an important departure point for understanding the mechanics of scattering. However, the atmosphere is optically thick enough to produce multiple scattering as well.

In our Terrascope, we only use Rayleigh scattering because it is less localized and weather variable. Furthermore, we can consider the Rayleigh scattering by a few specific molecules rather than the particles which constitute the complex, heterogeneous make-up of clouds.

To consider the impact of Rayleigh scattering on light, we will use the optical depth, which measures the ability of a substance to block or let through light. Substances with a small optical depth are called optically thin and allow particles to easily pass through; substances with a large optical depth are called optically thick and do not easily allow particles to pass through.

In the current case, we want to determine the optical thickness of the Earth's atmosphere at a given altitude and chemical composition, so that we can measure the chances of a light ray being Rayleigh scattered. In general, optical depth is calculated by Equation (3.21) [9].

$$\tau_{\text{scatt}} = \int_{z_{\text{start}}}^{z_{\text{end}}} N \sigma dz \quad (3.21)$$

Where:

- N : molecular number density
- σ : scattering cross section

For Rayleigh scattering, N and σ are given by [2]:

$$N = N_0 e^{-z/H} \quad (3.22)$$

$$\sigma = \frac{2k^4}{3\pi} \frac{\eta^2}{N^2} F_k(k) \quad (3.23)$$

Where:

- N_0 : molecular number density at $z=0$
- η : refractivity, a material's ability to refract
- $F_k(k)$: King correction factor, accounts for non-spherical nature of particles

Using Equations (3.22) and (3.23) to evaluate the equation for optical depth, (3.21):

$$\tau_{\text{scatt}} = \int_{z_{\text{start}}}^{z_{\text{end}}} N_0 e^{-z/H} \frac{2k^4}{3\pi} \frac{\eta^2}{N^2} dz \quad (3.24)$$

$$= \int_{z_{\text{start}}}^{z_{\text{end}}} N_0 e^{-z/H} \frac{2k^4}{3\pi} \frac{\eta^2}{(N_0 e^{-z/H})^2} dz \quad (3.25)$$

We can describe η the same as N , namely, $\eta = \eta_0 e^{-z/H}$. Using this to proceed with our equation for τ :

$$\tau_{\text{scatt}} = \int_{z_{\text{start}}}^{z_{\text{end}}} N_0 e^{-z/H} \frac{2k^4}{3\pi} \frac{(\eta_0 e^{-z/H})^2}{(N_0 e^{-z/H})^2} dz \quad (3.26)$$

$$= \int_{z_{\text{start}}}^{z_{\text{end}}} \frac{2k^4}{3\pi} \frac{\eta_0^2 e^{-z/H}}{N_0} dz \quad (3.27)$$

Once we have calculated the optical depth of the atmosphere through which the light passes, we calculate the survival probability of the light as:

$$p_{\text{scatt}} = e^{-\tau_{\text{scatt}}} \quad (3.28)$$

3.3.2. Implementation

Since modeling the scattering effects of all particles in the atmosphere is computationally intensive, we chose the three gaseous molecules with the highest concentration in the atmosphere: N_2 , O_2 , and Ar. Each of these has a different refractivity and, consequently, a different scattering cross-section. Additionally, N_2 and O_2 are not perfectly spherical, so we must introduce the King correction factor to account for this. This is because the "scattering cross section will always be larger for non-spherical particles compared to spherical particles with the same refractive index" [40]. The refractivities of each molecule – which are wavelength dependent— are given by Equations (3.29), (3.31), and (3.33). Each has an accompanying King correction factor— also wavelength dependent— given by (3.30), (3.32), and (3.34). Finally, Figure (3.9) is a plot of their scattering cross-sections.

N_2

$$\eta_{N_2} = \begin{cases} 5677.465 \times 10^{-8} + \frac{318.81874 \times 10^4}{14.4 \times 10^9 - \frac{1}{100\lambda}^2} & 254\text{nm} < \lambda < 468\text{nm} \\ 6498.2 \times 10^{-8} + \frac{307.43305 \times 10^4}{14.4 \times 10^9 - \frac{1}{100\lambda}^2} & 468\text{nm} < \lambda < 2059\text{nm} \end{cases} \quad (3.29)$$

$$F_{N_2} = 1.034 + 3.17 \times 10^{-12} \left(\frac{1}{\lambda \times 10^5} \right)^2 \quad (3.30)$$

O_2

$$\eta_{O_2} = \begin{cases} 20546.8 \times 10^{-8} + \frac{24.80899 \times 10^4}{4.09 \times 10^9 - \frac{1}{100\lambda}^2} & 288\text{nm} < \lambda < 546\text{nm} \end{cases} \quad (3.31)$$

$$F_{O_2} = 1.096 + 1.385 \times 10^{-11} \left(\frac{1}{\lambda \times 10^5} \right)^2 + 1.448 \times 10^{-20} \left(\frac{1}{\lambda \times 10^5} \right)^2 \quad (3.32)$$

Ar

$$\eta_{Ar} = \begin{cases} 6432.135 \times 10^{-8} + \frac{286.06021 \times 10^4}{14.4 \times 10^9 - \frac{1}{100\lambda}^2} & 303\text{nm} < \lambda < 2000\text{nm} \end{cases} \quad (3.33)$$

$$F_{Ar} = 1 \quad (3.34)$$

To calculate the optical depth of a part of the atmosphere, we combine the scattering cross-sections from the three molecules. Equation (3.27) becomes:

$$\tau = \int \frac{2k^4}{3\pi} \frac{f_{N_2} \eta_{N_2}^2 F_{N_2} + f_{O_2} \eta_{O_2}^2 F_{O_2} + f_{Ar} \eta_{Ar}^2}{N_{air}} e^{-z/H} dz \quad (3.35)$$

Where

- $f_{molecule}$: fraction of the molecule in the Earth's atmosphere (see Table (3.1))
- $\eta_{molecule}$: refractivity of molecule at the given wavelength
- $F_{molecule}$: King Correction Factor at the given wavelength
- N_{air} : Total number density of air, taken as 2.69×10^{25} and used for the number density of each molecule, (f/N_{air})

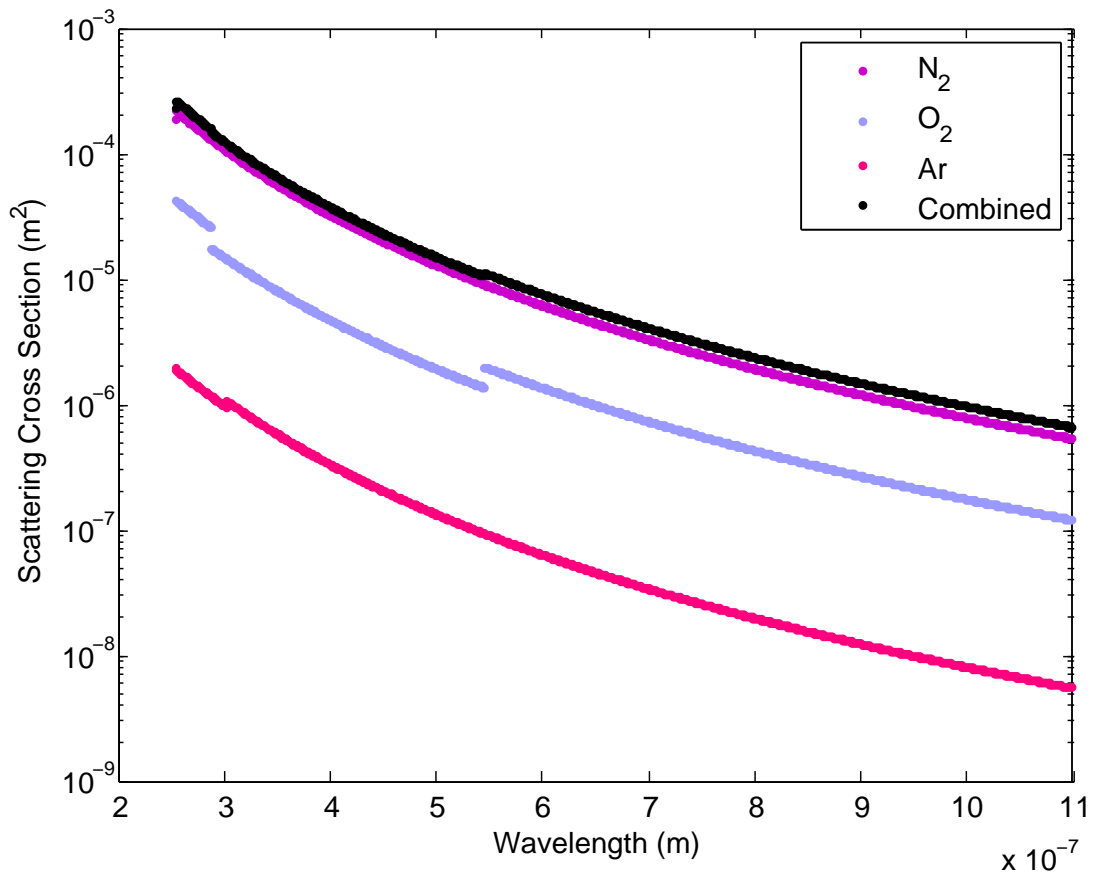


Figure 3.9: Plot of scattering cross section versus light wavelength, shown for three different gasses and their combined effect. The higher the cross section, the more likely light will scatter off of the molecule. Shorter wavelengths of light have higher cross sections because their periods are shorter and therefore more likely to collide with a particle. This relationship is seen in Equation (3.23). N₂ and O₂ have larger cross sections than Ar because they are made of two atoms as opposed to one. The combined effect, which is made up of the other three, is mostly dominated by N₂. The broken lines are where we used a function to estimate the wavelength ranges not covered by the literature we used.

Since the wavelength and molecular terms are independent of z , we can take them outside of the integral:

$$\tau = \frac{2k^4}{3\pi} \frac{f_{N_2}\eta_{N_2}^2 F_{N_2} + f_{O_2}\eta_{O_2}^2 F_{O_2} + f_{Ar}\eta_{Ar}^2}{N_{air}} \int_{z_{start}}^{z_{end}} e^{-z/H} dz \quad (3.36)$$

Similar to the coherence length calculation in Chapter 3.2, Equation (3.14), the integral in Equation (3.36) is calculated inside the z -loop as a Riemann Sum. At the end of the light ray propagation, the coefficient in front of the integral is calculated and multiplied by the integrand. Then, Equation (3.28) is used to calculate the survival probability.

3.3.3. Results

In this section, we present and interpret results of molecular scattering from runs of our Ter-
rascope model.

Figure (3.10) shows the dependence of Rayleigh scattering on minimum height of the light ray. Similar to coherence length, the survival probability increases with increasing minimum height. The reasons are somewhat similar, too. Light rays which pass through less of the Earth's atmosphere have a lower chance of hitting and scattering off of a particle. Unlike in the graph of coherence length versus minimum height (Figure (3.6)), the probability of survival does not increase at an increasing rate. Rather, it increases at a decreasing rate, flattening out as it nears the maximum survival probability of 1 (no more than 100% of light can survive).

In Figure (3.11), we again see a proportional relationship between scattering survival probability and the x -axis variable, L . The reason is the same as it was for coherence length. Minimum height and L are proportional to each other, so if scattering survival probability is proportional to one, it is also proportional to the other. As in Figure (3.10), the probability tends toward 1 as the distance increases, and this trend is the same for all wavelengths. Additionally, the longer the wavelength, the higher the probability the light has of surviving, for all values of L . However, note how when the wavelength is below 400nm, it is always scattered for all values of L that we modeled. This complete lack of survival is not well seen in Figure (3.10) because as shown in Figures (2.8) and (A.1), for the largest L we tested, the minimum altitude is only 13.7km. For even 50% of the 200nm light to pass through,— corresponding to a minimum altitude of 50km— the detector would have to be at a distance of 1.15×10^{11} m, which is 3/4 the distance to the Sun.

Figure (3.12) is again an inverse of its predecessor, showing how increasing λ and L increase a light ray's probability of passing through the atmosphere without scattering away from the detector. This graph shows that for the four largest L values, as the light wavelength increases, the difference between the survival probability of each L value decreases as they all approach 1. However, it will take a longer wavelength for the smallest L value, which is the distance to the Moon, to reach a survival probability of 1.

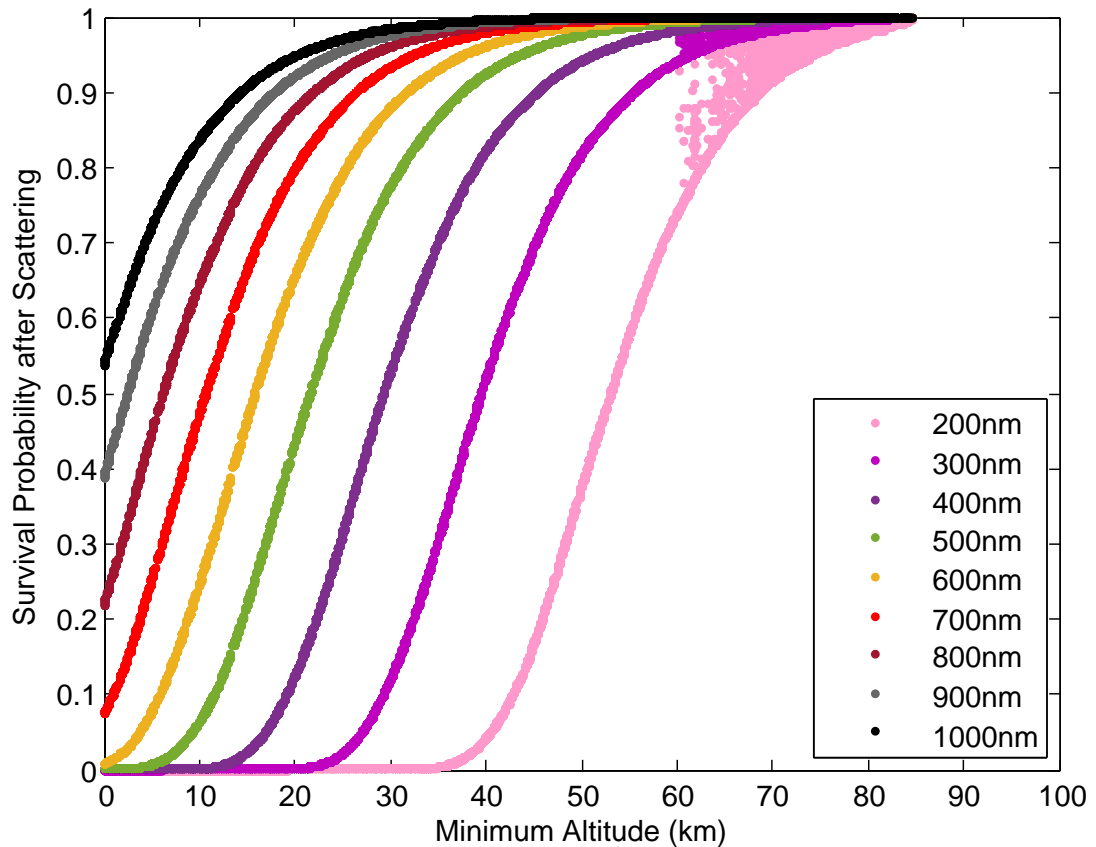


Figure 3.10: Plot of survival probability after scattering versus the lowest height that each light ray reaches in the atmosphere, for nine different wavelengths. Graph was made using the 'Angle Array' code. The results are consistent with the pattern shown in Table (3.2), that the higher the altitude, the fewer the particles in the atmosphere. It follows that a light ray which passes through a higher minimum altitude collides with fewer particles and therefore has a higher chance of surviving its path through the atmosphere towards the detector. The relationship with respect to wavelength is consistent with that seen in the coherence length graphs; the longer the wavelength, the less likely the light ray is to scatter off a particle and the higher it's survival probability. The points in the top right of the graph are numerical artifacts due to the light rays reaching close to the artificially imposed atmosphere at $10H \sim 80\text{km}$.

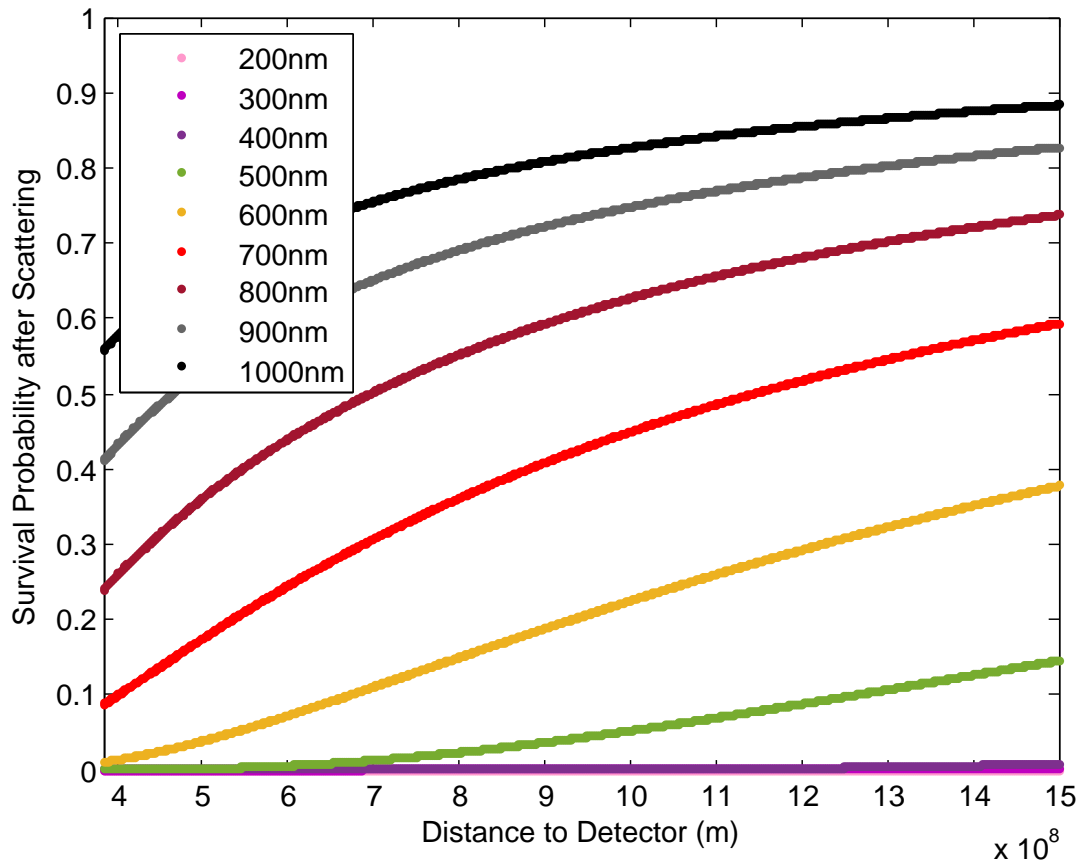


Figure 3.11: Plot of survival probability after scattering versus the distance from Earth's center to the detector, L , for nine different wavelengths. This graph was made using the 'Single Ray' code. Recall how the coherence length graphs, Figures (3.7) and (3.6), are related. A smaller minimum altitude corresponds to a shorter coherence length, and since a smaller L has a smaller minimum altitude, a smaller L also corresponds to a shorter coherence length. The same is relationship is true of Figure (3.10) and this graph. A smaller minimum altitude means a lower chance of survival after scattering, and since a smaller L has a smaller minimum altitude, a smaller L also means a lower chance of survival after scattering.

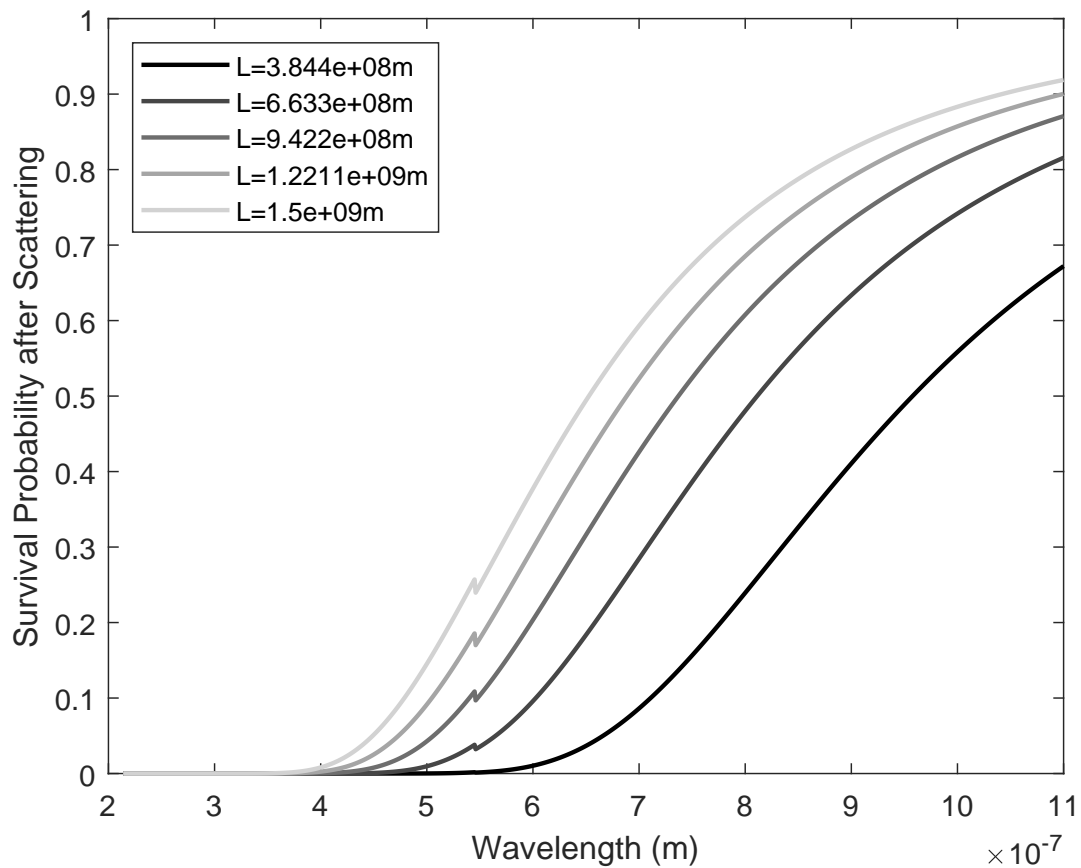


Figure 3.12: Plot of survival probability after scattering versus light wavelength, for five different L values. This graph was made using the 'Single Ray' code. It better illustrates the lack of surviving rays below 400nm than Figure (3.11). The larger L and wavelength values have a higher probability of reaching the detector, similar to the trend in the coherence length plots. It appears that for larger L and wavelength, the quality of our Terrascope improves. The dip at 550nm is due to the change in O_2 scattering cross-section function seen as the broken line in Figure (3.9).

3.4. Absorption

3.4.1. Theory

Absorption is the phenomena of light being taken into a molecule and the molecule gaining energy equal to the energy in the amount of light. When materials absorb light their electrons are excited to higher energy levels, where the change in energy is proportional to the frequency of the light (inversely proportion to wavelength). The exact relationship is given by the Planck-Einstein equation:

$$E = h\nu = \frac{hc}{\lambda} \quad (3.37)$$

Where:

- E : energy
- h : Planck's constant, defined by this equation
- c : speed of light in a vacuum
- ν : frequency
- λ : wavelength

The energy of the incoming photon must exactly match the difference in energy level in the material in order for the photon to be absorbed and the electron to become excited [24]. As seen in Equation (3.37), this energy excitation corresponds to a specific wavelength, thus absorption is wavelength dependent. Each material has a unique absorption spectrum in which the energy dips at these specific wavelengths. Figure (3.13) shows the accumulated absorption spectrum of the atmosphere; Figure (3.14) shows the IR window of the absorption spectrum for specific gases.

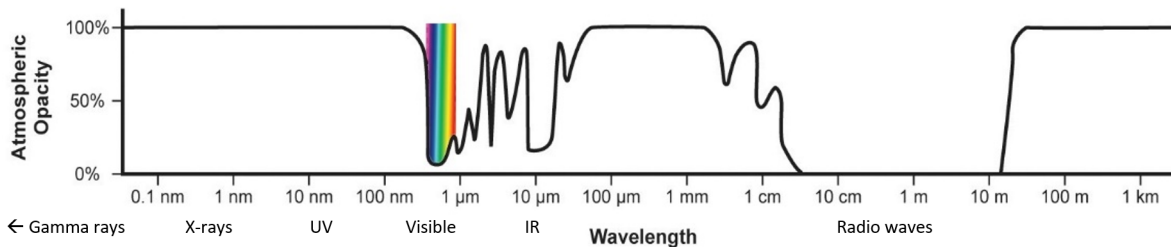


Figure 3.13: Absorption spectrum for the Earth's entire atmosphere. Gamma rays, X-rays, UV rays, mid-IR, far-IR, and long radio waves are all blocked out in the upper atmosphere. Nitrogen gas, for example, is responsible for much of the UV absorption in the 80-100nm range [47]. There is a "window" where visible and near-IR light get through and are observed from Earth: see Figure (3.14) [44]

As can be seen in Figure (3.14), the absorption lines are not strictly lines of infinitesimal width, rather, they are wider due to "broadening" affects. These are listed below [24]:

- **Natural line broadening:** due to the uncertain nature of quantum energy states; homogeneous widening in Lorentzian shape; the broadening (defined as change in frequency) is:

$$\Delta\nu \geq \frac{32\pi^2\nu^3}{(4\pi\epsilon_0)3hc^3}|R^{nm}|^2, \quad R^{nm} \text{ is the transition moment}$$

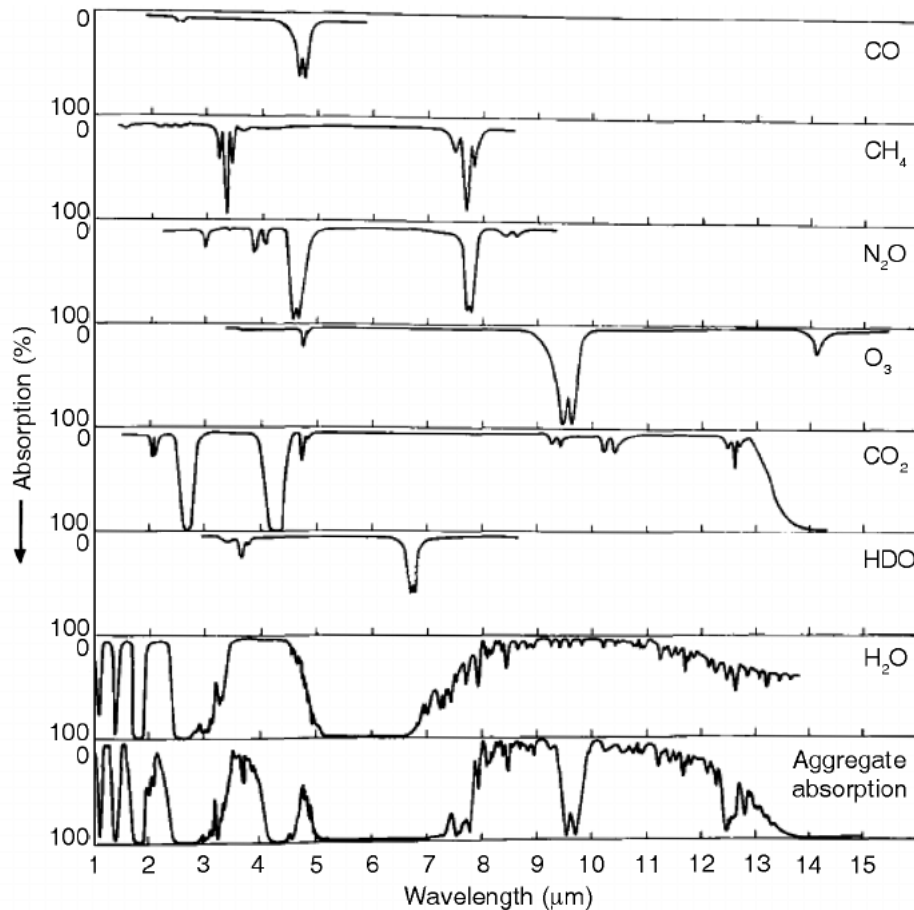


Figure 3.14: Absorption spectra for gases found in Earth's atmosphere, with a focus on the near-IR part of the electromagnetic spectrum. The vertical axis indicates percentage of radiation absorbed [8].

- **Doppler broadening:** due to the Maxwell velocity distribution of the gas atoms/molecule relative to the detector; homogeneous widening in Gaussian shape; the broadening is:

$$\Delta\nu = \frac{v}{c} \left(\frac{2kT \ln 2}{m} \right)^{1/2} \quad m \text{ is the mass of the atom/molecule}$$

- **Pressure broadening:** due to collisions between atoms/molecules; homogeneous widening in Lorentzian shape, except at low frequencies; the broadening is:

$$\Delta\nu = (2\pi\tau)^{-1} \quad \tau \text{ is the mean time between collisions}$$

- **Power/saturation broadening:** due to increased intensity of incident light; homogeneous widening in Lorentzian shape [49]

Similar to scattering, we describe the effects of atmospheric absorption in terms of optical depth. The equation is very similar to the one used before, Equation (3.21), but different in its dependencies:

$$\tau_{\text{absorb}} = \int_{z_{\text{start}}}^{z_{\text{end}}} N(z)\sigma(z)dz \quad (3.38)$$

- $N(z)$: molecular number density
- $\sigma(z)$: absorption cross section

Because of the z dependencies, we calculate $N(z)\sigma(z)$ inside the z -loop as a Riemann Sum. Then, Equation (3.39) is used to calculate the survival probability of the light.

$$p_{\text{absorb}} = e^{-\tau_{\text{absorb}}} \quad (3.39)$$

3.4.2. Implementation

Similarly as for scattering, we do not model the absorption effects of all molecules in the atmosphere. Rather, for our Terrascope, we choose to only include O_3 because of its effects in the wavelength range of interest and because it mostly appears in only one band of the atmosphere (the stratosphere). The latter reason should make it easy to see the effects of O_3 over a certain range of altitudes. We use Equation (3.40) for the molecular number density:

$$N_{\text{O}_3}(z) = 4.75 \times 10^{18} e^{-\frac{(z-23)^2}{1000}} \quad (3.40)$$

For $\sigma(z)$, the z -dependence comes from a dependence on temperature. Temperature and altitude are related by the following equation, also shown in Figures (3.1) and (3.15):

$$T = \frac{(z-3)|z-50|(z-116)}{1000} \quad (3.41)$$

$\sigma(z)$ is also dependent on wavelength. Thus, for our model calculations, we used a table of values sorted by temperature (row) and wavelength (column) [39]. Figures (3.16) and (3.17) show a plot of the table values, one parameterized on temperature and the other on wavelength. Using Equation (3.41), the relationship shown in Figures (3.16) and (3.17) can be represented in terms of altitude instead of temperature. This is shown in Figure (3.18).

The wavelength discretization in the data was on the order of fractions of nanometers, small enough that we could pick the row which corresponded to our current wavelength of interest. However, the temperature (and therefore altitude) contained in the data had a discretization larger than that of our Terrascope. The temperature discretization was every ten degrees Celsius, while our temperature discretization was proportional to the altitude, which is then proportional to the step size of the z -loop. This step size can change, so we created a method to linearly interpolate between the table's given temperature values. To do this, we first call the temperatures which are closest to our desired value in terms of their column numbers:

$$T_{\text{col}}^- = -\left\lfloor \frac{T}{10} \right\rfloor + 3 \quad (3.42)$$

$$T_{\text{col}}^+ = -\left\lceil -\frac{T}{10} \right\rceil + 2 \quad (3.43)$$

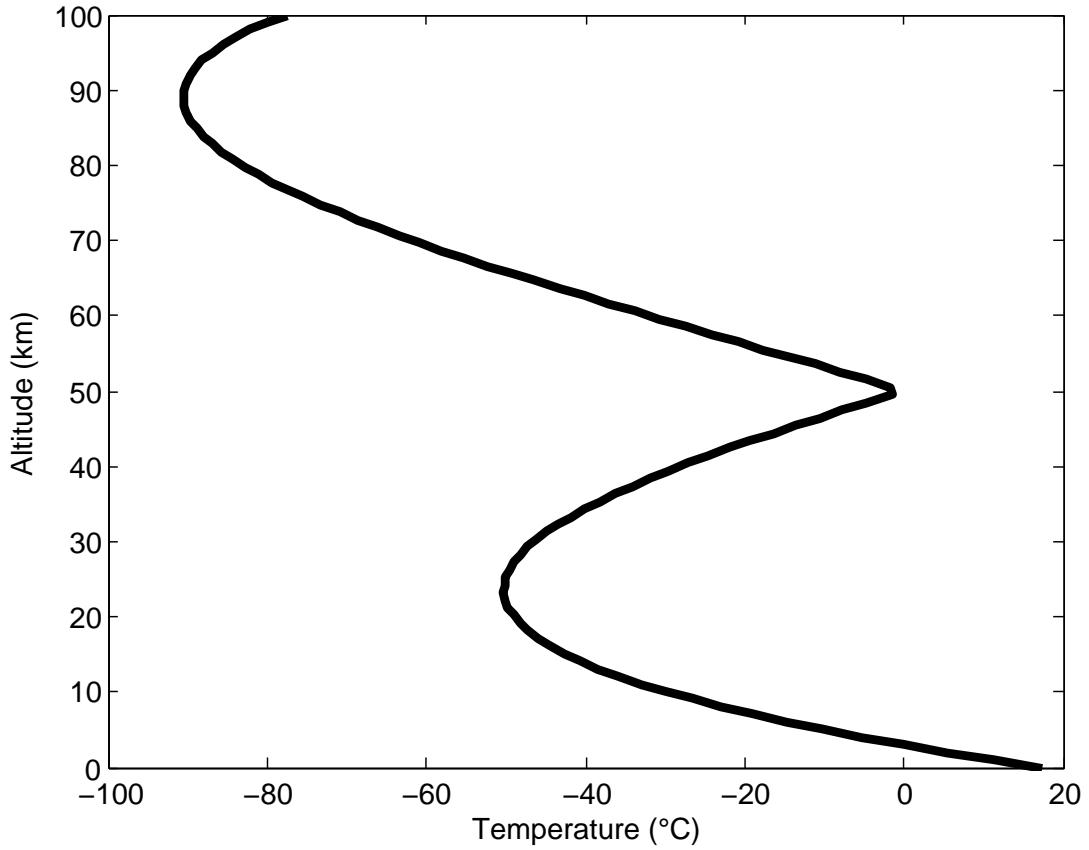


Figure 3.15: How temperature varies with altitude, modeled using Equation (3.41). As mentioned in the beginning of Chapter 3, the ozone layer (consisting of O_3 molecules) absorbs UV light and heats up the atmosphere. This causes the temperature to increase with increasing altitude, rather than decrease with increasing altitude. This change in the function's direction is seen in the graph around 25km.

If the left (high) column temperature goes outside the range, set it to the left most (highest) column:

$$\text{if } T_{\text{col}}^- < 1 \Rightarrow T_{\text{col}}^- = 1 \quad (3.44)$$

$$\text{if } T_{\text{col}}^- > 11 \Rightarrow T_{\text{col}}^- = 11 \quad (3.45)$$

If the right (low) column temperature goes outside the range, set it to the right most (lowest) column:

$$\text{if } T_{\text{col}}^+ < 1 \Rightarrow T_{\text{col}}^- = 1 \quad (3.46)$$

$$\text{if } T_{\text{col}}^+ > 11 \Rightarrow T_{\text{col}}^- = 11 \quad (3.47)$$

Call the corresponding cross section values, where the wavelength is the row and temperature is the column:

$$\sigma^- = \sigma(\lambda, T_{\text{col}}^-) \quad (3.48)$$

$$\sigma^+ = \sigma(\lambda, T_{\text{col}}^+) \quad (3.49)$$

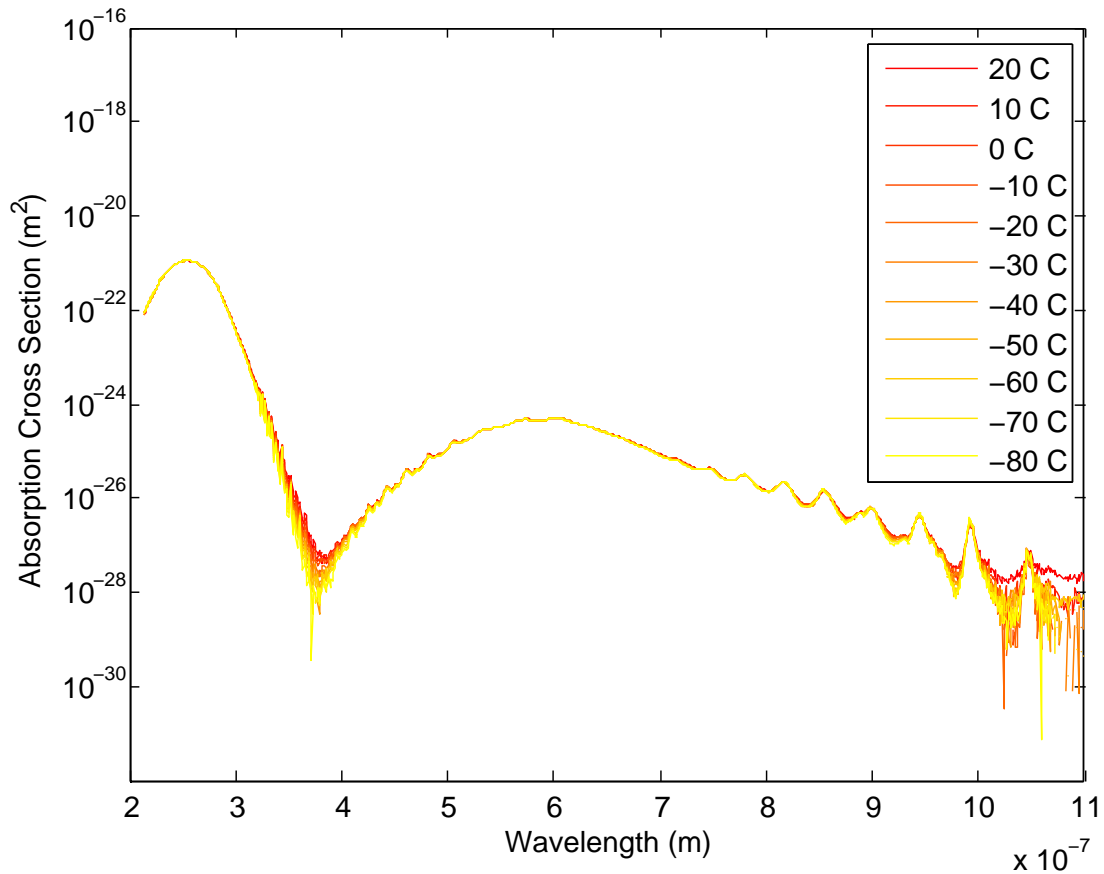


Figure 3.16: Plot of O_3 absorption cross section table values versus wavelength. Each cross section is based on the wavelength of light and temperature of the system. The variation with wavelength is based on the structure of the molecule. The overall trend in this wavelength range of increasing cross section with increasing temperature means that at higher temperatures, light rays are more likely to collide with an O_3 molecule. This is due to Doppler broadening. Around 400nm and 1000-1100nm, note the widened absorption in the higher temperatures; this is an example of such broadening.

Perform linear interpolation to get the sigma value in between the desired columns:

$$\sigma = \sigma^- + (T_{\text{model}} - T_{O_3}) \frac{\sigma^+ - \sigma^-}{10} \quad (3.50)$$

As for coherence length and scattering, we calculate the appropriate integral, Equation (3.38) as a Riemann Sum. Then, Equation (3.39) is used to calculate the survival probability.

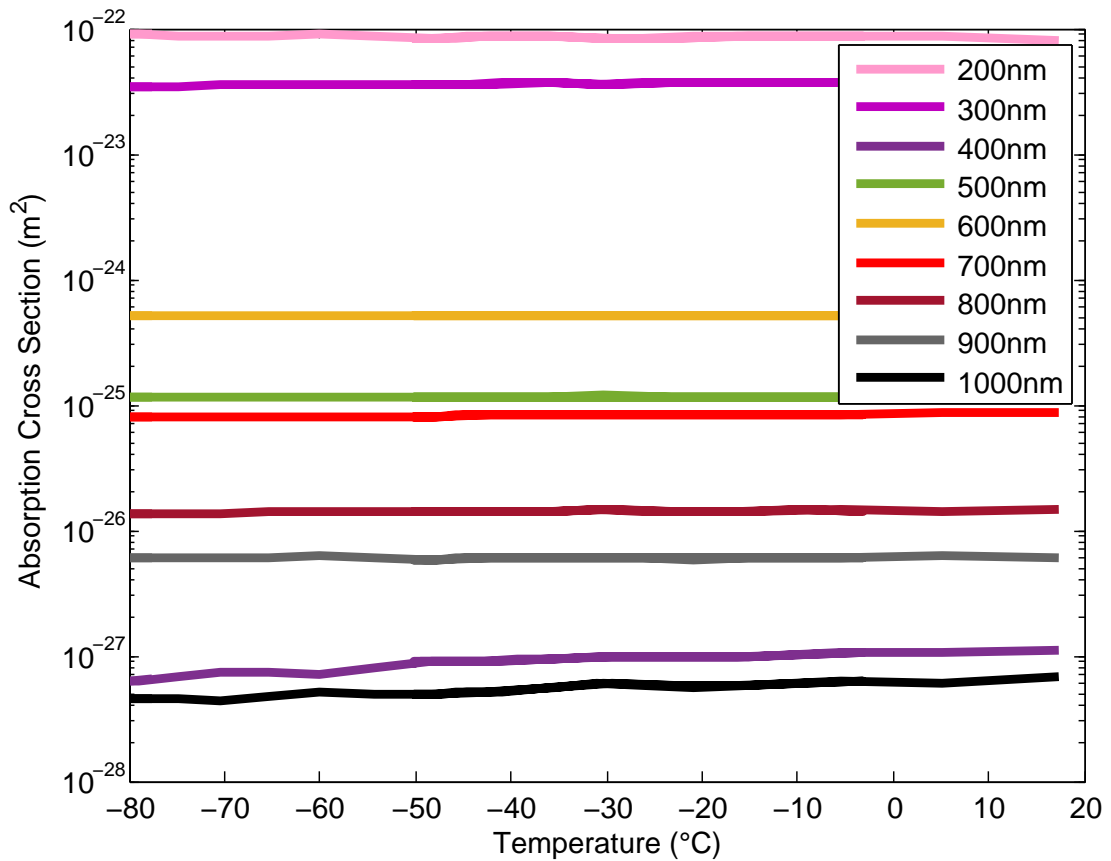


Figure 3.17: Similar to Figure (3.16), this is a plot of O₃ absorption cross section table values. However, in this figure, temperature is the horizontal axis and the wavelength is parameterized. This plot confirms that the higher wavelengths have a larger cross section. It also shows that the temperature variation is not large, but is slightly more significant for 1000nm and 400nm. Note that these two lines are the lowest cross section, and are the dips seen in Figure (3.16).

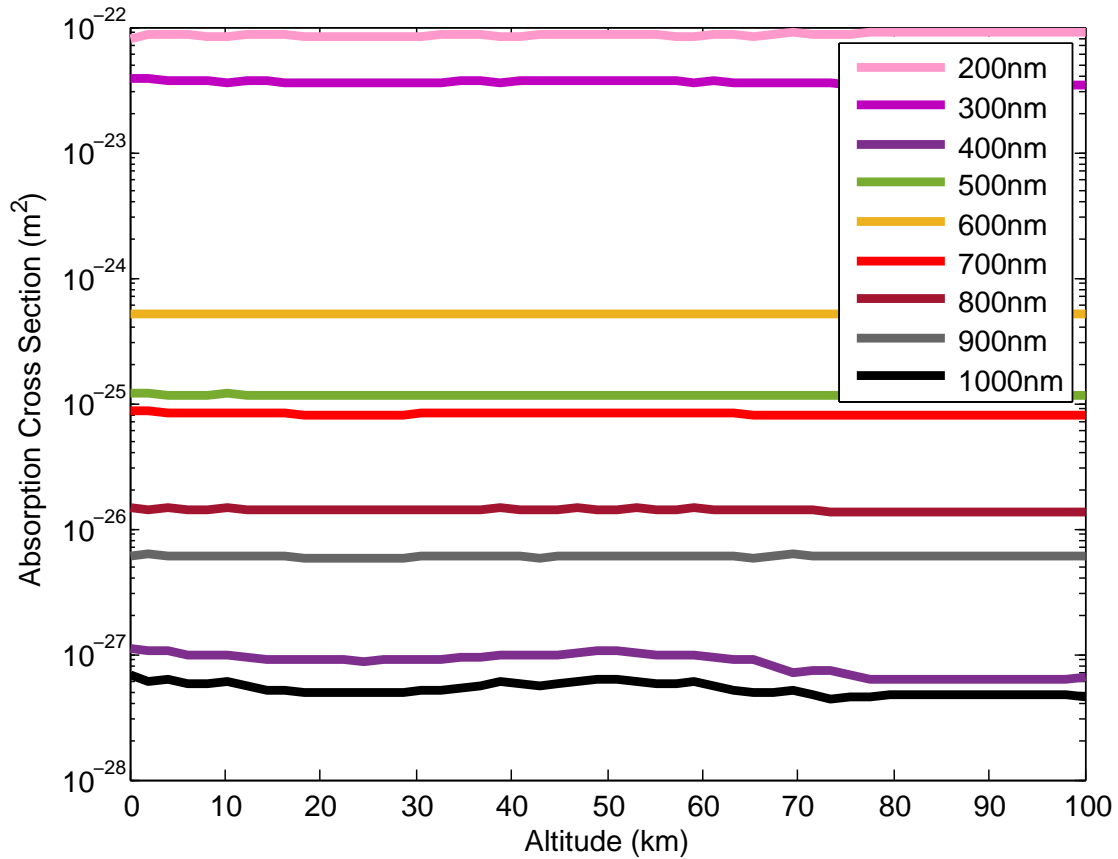


Figure 3.18: Similar to Figure (3.17), but using the altitude values in Equation (3.41) in place of the temperature. This gives a visual of how the cross sections vary with different variables. The variation is small over the atmosphere and more pronounced for different wavelengths.

3.4.3. Results

In this section, we present and interpret results of O_3 absorption from runs of our Terrascope model.

Figure (3.19) is similar to Figure (3.10) in that the highest minimum altitudes correspond to the highest survival probability. However, unlike for scattering survival probability, the absorption survival probability has a dip around 20km and does not continuously increase with increasing wavelength. The former phenomenon is explained by the existence of the ozone layer around 20km; the many O_3 molecules in that layer have a large chance of absorbing light, and thus the survival probability for light rays there is lower. The latter phenomenon is explained by the effect of wavelength on the absorption cross section seen in Figure (3.18). This plot shows that 400nm has one of the smallest cross sections while 600nm has one of the largest. Smaller cross sections lead to a smaller probability of absorption and thus to a higher probability of survival, so it makes sense that 400nm light has one of the highest survival probabilities after absorption. Larger cross sections leads to a larger probability of absorption and thus to a lower probability of survival, so it makes sense that 600nm light has one of the lowest survival probabilities after absorption.

Figure (3.20) gives a view of how the absorption survival probability varies with detector placement, also dependent upon wavelength. The wavelength order is the same as in Figure (3.19). It appears that as the distance to the detector increases, the survival probability decreases. This is because the L values in our graph correspond to the ozone-induced dip from 0 – 20km in Figure (3.19). We have seen that minimum altitude and L are proportional, so we can extrapolate beyond this graph. For L values greater than those corresponding to 20km, the absorption survival probability will increase with increasing distance from the detector. A minimum altitude of 20km corresponds to $L = 3.4 \times 10^9$ m.

Figure (3.21) shows clearly the dips in survival probability due to high absorption at wavelengths of 200nm, 300nm, and 600nm. It also exhibits that 600nm light has the largest difference in survival probability due to different L values. At other wavelengths, the L value does not have much of an effect on the probability of survival. Comparing this graph to Figure (3.9), we see that despite the aforementioned dips at certain wavelengths, survival probability is closer to 1 for absorption than it is for scattering. Absorption seems to have a smaller effect on the light rays than scattering.

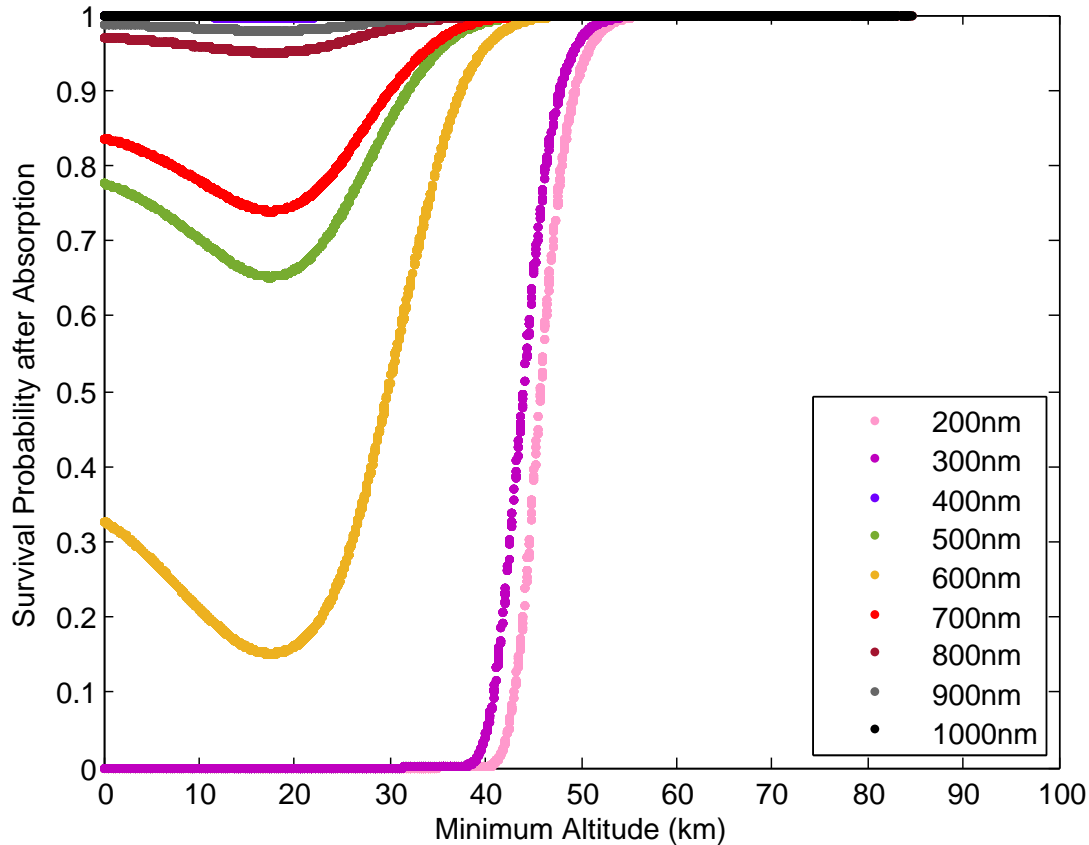


Figure 3.19: Plot of survival probability after absorption versus the lowest height that each light ray reaches in the atmosphere, for nine different wavelengths. This graph was made using the 'Angle Array' code. Note that a dip occurs in most wavelengths around 20km, as dictated by Equation (3.40). This is due to the high concentration of O_3 in the Ozone layer around that altitude. The change in temperature function– the inflection point– seen in Figure (3.15) occurs at a higher altitude because it takes a sufficient amount of O_3 molecules before the behavior of the system changes. Note how, unlike for scattering survival probability, the curves for different wavelengths are not in order. That is, 600nm light (yellow) has a higher overall survival probability than 300nm light (magenta), but lower probability than 500nm light (green). This is because 600nm light has a lower absorption cross section than 300nm light, but a higher absorption cross section than 500nm light. The lower the absorption cross section, the higher the probability of survival. Following the trend of cross section dictating the wavelength order, the 400nm light (purple) can be seen near the top, just below that 1000nm light (black).

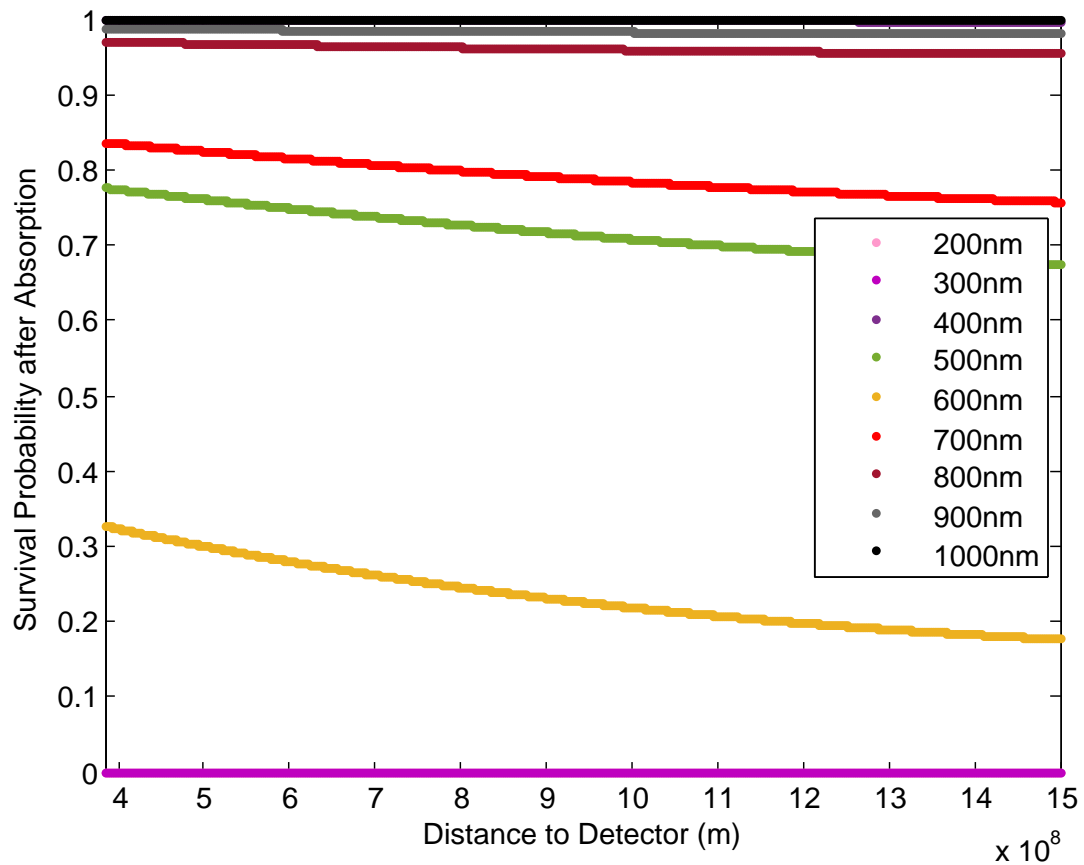


Figure 3.20: Plot of survival probability due to absorption versus the distance from Earth's center to the detector, L , for nine different wavelengths. This graph was made using the 'Single Ray' code. Similar to the corresponding scattering survival probability graph, Figure (3.11), below a certain wavelength threshold, all light is absorbed for any values of L we modeled. For scattering this is at 400nm, for absorption it is 300nm. For absorption, the 400nm light has the highest survival probability along with 1000nm light. Both of these lines are at the top of the graph. Overall, the survival probability after absorption is higher than after scattering, indicating that scattering is the stronger affect in our Terrascope scenario.

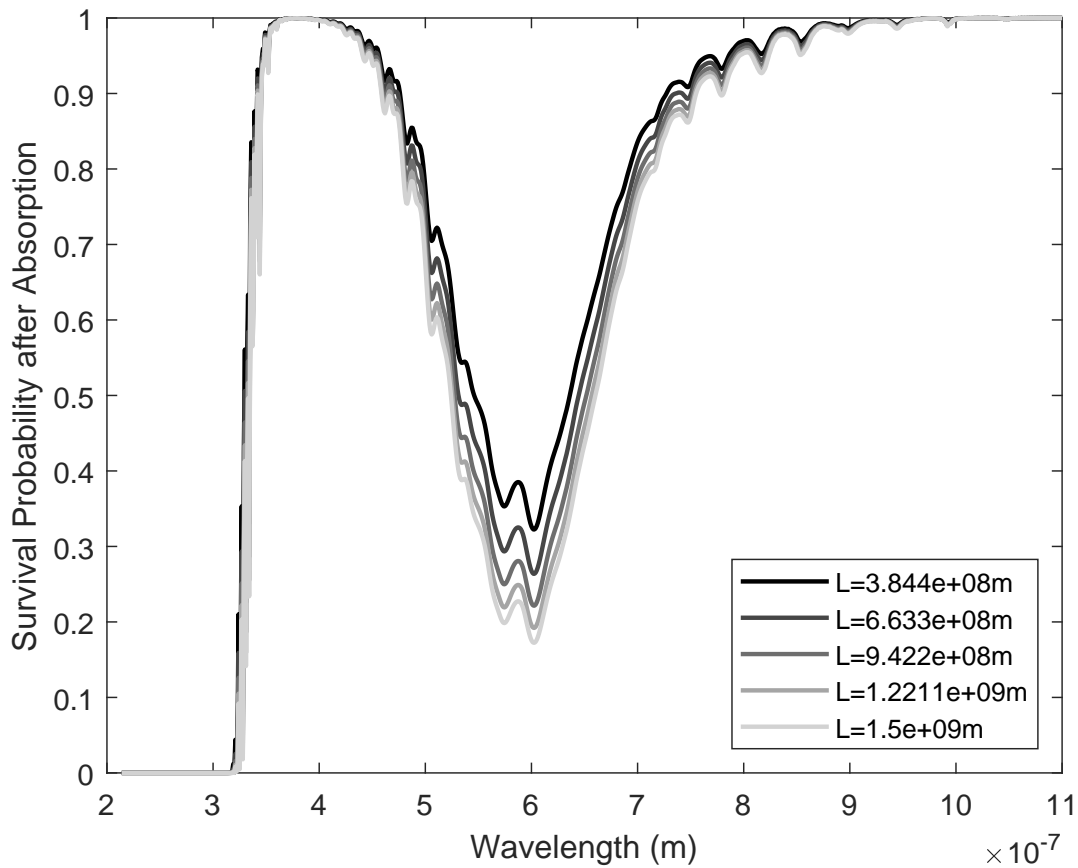


Figure 3.21: Plot of survival probability after absorption versus light wavelength, for five different L values. This graph was made using the 'Single Ray' code. It has the opposite x -axis and parameterization as Figure (3.20) to better show the detailed dependence of absorption survival probability on wavelength. In this graph, the "out of order" wavelengths in Figures (3.19) and (3.20) are seen as a dip at 600nm. The parameterized black lines also confirm what was seen in the above graph, namely, that the larger L values correspond to a lower survival probability. The wavy lines throughout are due to the absorption cross section fluctuations with temperature (and therefore with altitude and L), originally seen in Figure (3.16).

3.5. Transmittance

The total effect of particles on light rays moving through Earth's atmosphere is captured in our Terrascope model by combining the Rayleigh scattering and O₃ absorption. Until this point, we have measured each of their effects in terms of the probability of light surviving through the atmosphere. We could call their combined effect the total survival probability, but instead we call it the total transmittance. This makes it more clear that it is the amount of light transmitted from the celestial object through the atmosphere into the detector. Equation (3.51) is how total transmittance is calculated.

$$p_{\text{transmit}} = e^{-\tau_{\text{scatt}} - \tau_{\text{absorb}}} \quad (3.51)$$

Figures (3.22), (3.23), and (3.24) are a combination of the scattering and absorption survival probability graphs. The transmittance line shapes are dominated by the scattering line shapes because the scattering is stronger, seen when we compare the molecular number density and cross sections of scattering and absorption. The molecular number density of N₂, O₂, and Ar are 2.1×10^{25} , 5.6×10^{24} , and 2.5×10^{23} respectively; the molecular number density of O₃ is at maximum 4.75×10^{18} . Scattering dominates here. The scattering cross section, σ_{scatt} , varies from $10^{-8.5}$ to $10^{-3.7}$; the absorption cross section, σ_{absorb} , varies from $10^{-27.5}$ to 10^{-22} . Scattering dominates here as well. Thus, overall, the scattering effects dominate transmittance. However, the sharp dips in the absorption can still be seen, and thus effect the light entering the detector.

In the next section, we investigate the light which has entered the detector, looking at overall amplification and resolution due to all of the effects covered here.

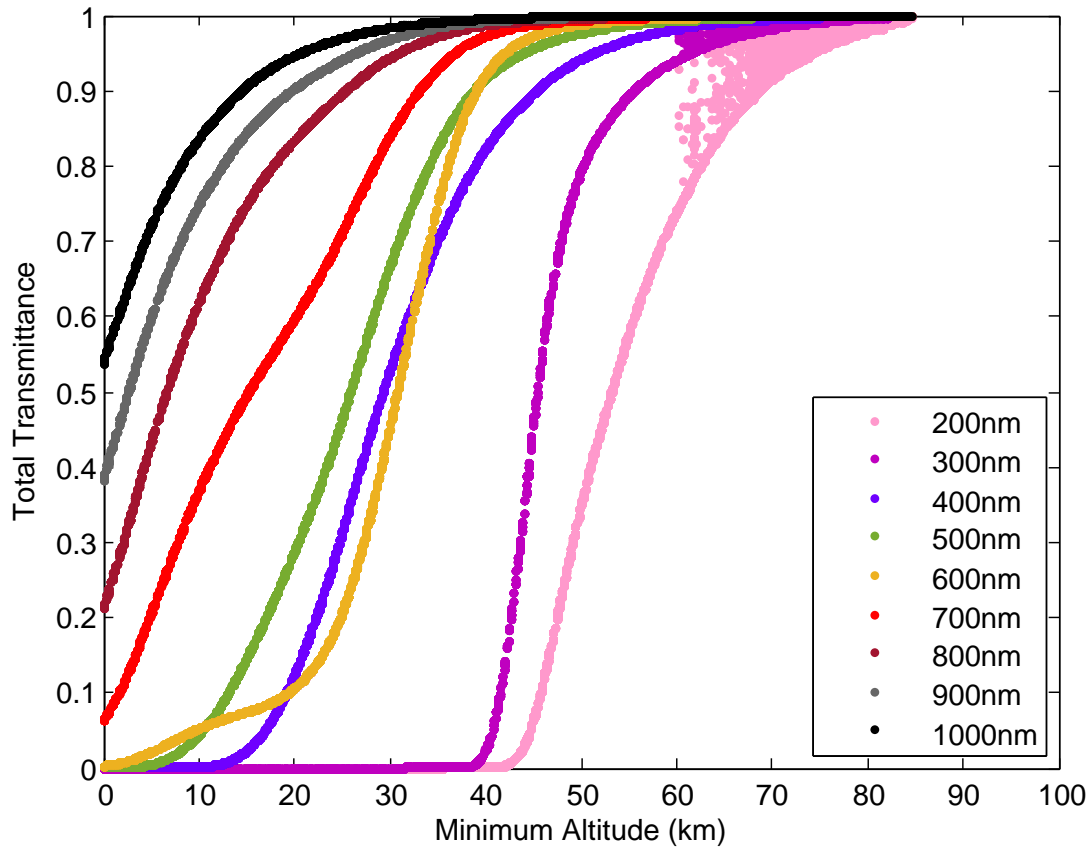


Figure 3.22: Plot of total transmittance versus the lowest height that each light ray reaches in the atmosphere, for nine different wavelengths. Graph was made using the 'Angle Array' code. Combining the graphs of scattering and absorption yields the line shape of former and the Ozone layer dips of the later. The 600nm (yellow) line drops the most around 22km because it begins to be strongly absorbed at that altitude. Overall, the longer wavelengths appear to transmit the most light into the detector.

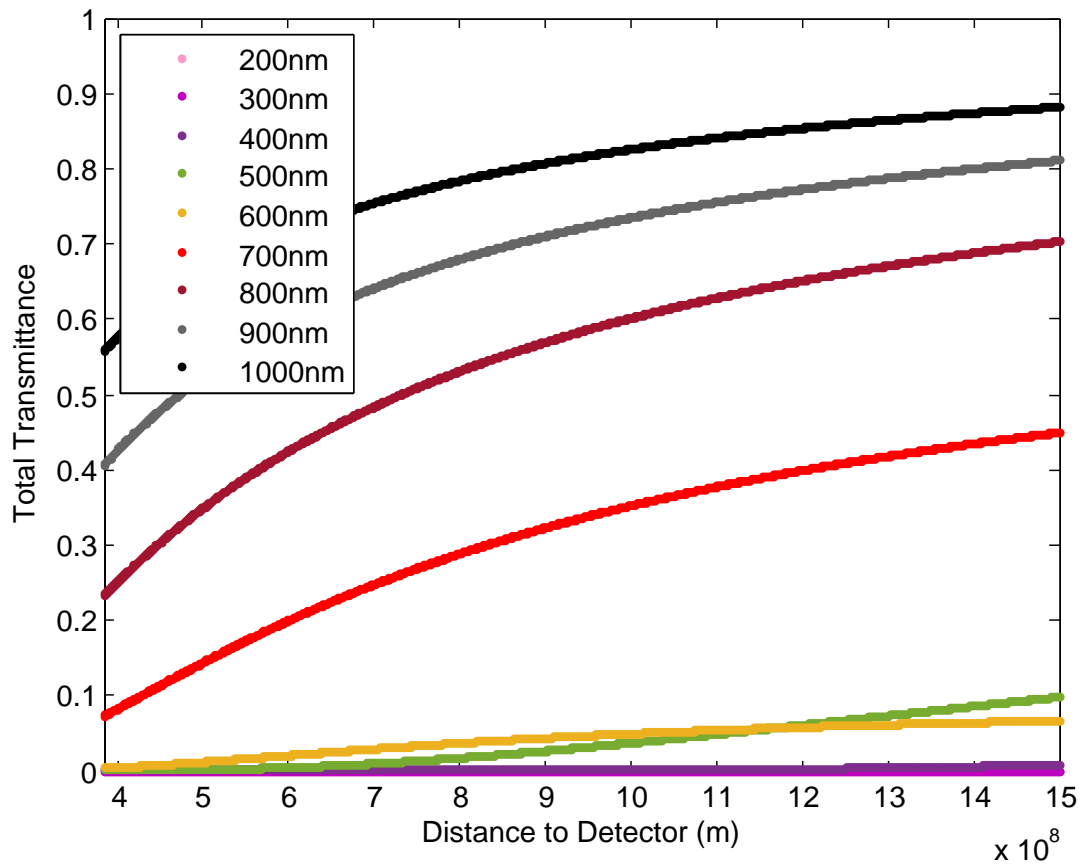


Figure 3.23: Plot of survival probability after absorption versus the distance from Earth's center to the detector, L , for nine different wavelengths. This graph was made using the 'Single Ray' code. Here, the 600nm (yellow) line crosses the 500nm (green) line at around $L = 1.17 \times 10^9$ m. This corresponds to the minimum height where they crossed in Figure (3.22), 11km. The 600nm line will cross the 400nm (purple) line for around $L = 4.3 \times 10^9$ m.

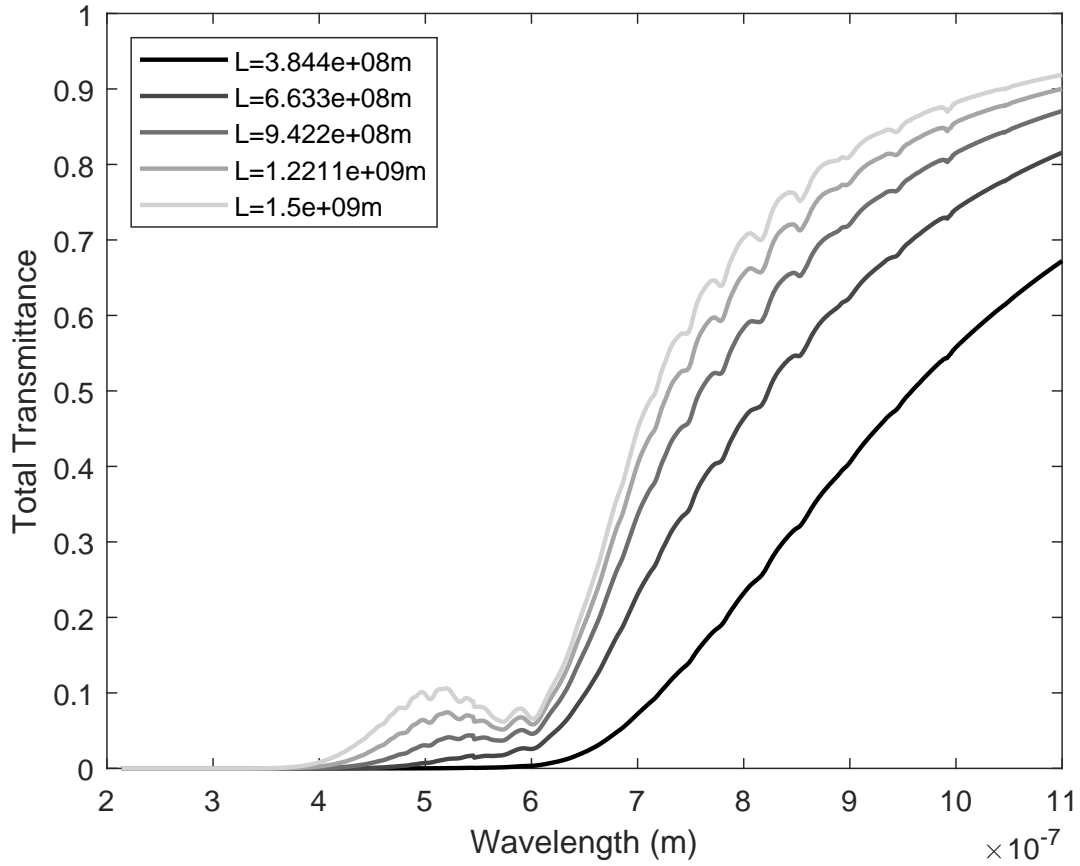


Figure 3.24: Plot of total transmittance versus light wavelength, for five different L values. Graph was made using the 'Single Ray' code. As before, the general shape mirrors that of the corresponding scattering survival probability plot, but with added Ozone layer dips and wavy lines due to absorption cross section temperature fluctuations.

3.6. Combining Effects: Point Spread Function

3.6.1. Theory

The ultimate goal of our Terrascope is to determine the quality of the light which reaches from a celestial object to the detector. To analyze the quality, we want to know how much the light was amplified and how much it was spread out from the point source of its original object. A point spread function (hereby abbreviated as 'PSF') measures this and thus characterizes how a point source is imaged by an optical instrument. Our calculation of a PSF is different from the literature, but the name and general goals were used because they accurately describe what we compute.

The amplification of an optical instrument, in our case a telescope, is defined as the ratio of the intensity of the light from the viewed object with and without the telescope. Since a telescope receives light proportional to its area and the light emitted from the object is also calculated per area, one can define this ratio in terms of area. Kipping defines this as:

$$A = \epsilon \frac{\pi (b_+^2 - b_-^2)}{\pi ((a/2)^2)} \quad (3.52)$$

Where:

- A : amplification
- ϵ : loss parameter due to extinction from absorption and scattering in the atmosphere
- b_+ : place where light ray that hits the top of the detector
- b_- : place where light ray that hits the bottom of the detector
- a : diameter/aperture of the detector

In Equation (3.52), the numerator represents the area of the circular ring of lensed light which the Earth's atmosphere produces; the denominator is the area of the detector. After a number of approximations, Kipping arrives at the following amplification equation:

$$A \sim \frac{8H\epsilon}{a} \quad (3.53)$$

We will define our results in terms of Equation (3.53) to best compare them to Kipping's results. In order to do this, we must translate this amplification in terms of our numerical model, which is in terms of brightened pixels. This will be expounded upon in the next subsection.

In addition to the amplification, we qualify the spread of the point light source. The spread is best quantified by the coherence length, calculated in Chapter 3.2, but we can use a PSF to plot the image blur. We want to see how a decrease in coherence length leads to a slower amplification drop off from the center point as the point source is spread into a larger area.

The following subsection will explain how we incorporated the three atmospheric effects from earlier in the chapter – turbulence, scattering, absorption– into our final image analysis. We

endeavor to qualify and quantify how the atmosphere will change what our Terrascope detector will observe from a celestial object.

3.6.2. Implementation

Since our Terrascope model begins at the detector and traces rays through the atmosphere back to the celestial object, the final rays which emerge are a simulation of what the object would look like as its original point source. As explained in Chapter 2, we used three different types of codes. For calculating the PSF, we only used two of these: Angle Array and Thin Ring. This is because we want to trace as many arrays as possible to simulate the bright incoming light from the source object. Recall that there is an α_1 and α_2 direction; each has N rays. Thus, if $N = 10^4$, the array contains $N^2 = 10^8$ rays which must be initialized, traced individually through the atmosphere, and their final positions plotted. This becomes too computationally expensive after around $N = 5 \times 10^4$ and as a result, the Thin Ring code is adopted for all higher values. Runtimes of a few hours can still be achieved up to $N = 10^6$, which creates $N^2 = 10^{12}$ total rays.

Each ray has a unique initial position defined by its α_1 and α_2 values. It is propagated by the equations of motion until it exits the atmosphere at an angle parallel to the z -axis, simulating light coming from a far away object. Light emanates from a spherical celestial object in all directions, but by the time the light reaches Earth, the rays traveling towards Earth will be approximately parallel to each other (and to our z -axis). When each light ray emerges from the atmosphere, it is in a different place than where it entered, but we can also define this new position by the α_1 and α_2 directions. We call these final angles $\alpha_{1\text{final}}$ and $\alpha_{2\text{final}}$. Using the final angles as coordinates, we place a point (a counter) on a grid for each light ray at the position. If we want to include an atmospheric effect in the PSF, we add an appropriately scaled counter. For turbulence, we add $\alpha_{1\text{difffrac}}$ and $\alpha_{2\text{difffrac}}$ from Equations (3.18) and (3.19). For scattering, we add the scattering survival probability $e^{\tau_{\text{scatt}}}$ from Equation (3.28). For absorption, we add the absorption survival probability $e^{\tau_{\text{absorb}}}$ from Equation (3.39).

To focus on where the most light is, we choose a smaller angular size for the PSF so that we are effectively "zooming into" the center peak. This angular size is defined as $\alpha_{\text{peak}} \times \alpha_{\text{peak}}$. However, even after this adjustment, if we were to simply look at this resulting grid, it would be difficult to see the concentration of light from the object. Small numerical differences would result in few (if any) points having the exact same value, so the resulting image, the PSF, would not appear as a point source. Additionally, it would be computationally expensive to plot a grid of 10^6 -by- 10^6 points.

We introduce larger bins to hold all light rays which fall into a certain area. M defines the length of a new grid size, making M^2 the area of the new grid and the number of bins, each occupying a larger area than in the original grid. This means that $\frac{N^2}{M^2}$ rays will be condensed into one bin. For example, if $N = 10^3$, the number of rays is $N^2 = 10^6$. Set $M = 10$, meaning the new grid

consists of $M^2 = 10 \times 10 = 10^2$ bins. If there are $N^2 = 10^6$ rays which must be condensed into $M = 10^2$ bins, then there are $\frac{N^2}{M^2} = \frac{10^6}{10^2} = 10^4$ possible rays per bin. Each small bin does not have to hold $\frac{N^2}{M^2}$ rays, rather, this means that the $\frac{N^2}{M^2}$ rays in the area of that one bin all add one counter to the bin. This will make the bin counter higher and the area appear brighter than if the rays were all split into individual smaller bins with a counter of one. At the end of the binning process, the PSF is multiplied by the factor $\frac{M^2}{N^2}$ to re-adjust the brightness. We want the bins to appear brighter, but we do not want to incorrectly measure the resulting image as brighter than it is in reality.

The M value in our PSF can be used to calculate an effective aperture size, effectively translating pixel length to aperture length. This detector diameter can then be related to Kipping's detector diameter and his resulting amplification calculation. To measure aperture size, we imagine that a ray comes into the detector from two different places in the sky— as will happen while the Earth revolves around the Sun— hitting the detector in two different places. At one place, the ray is on-axis, meaning that the object's light enters the atmosphere at an angle parallel to the z -axis. At the other place, the ray is off-axis, meaning that the object's light enters the atmosphere at an angle to the z -axis. The z axis represents the imaginary line extending from the Earth to the detector. Figure (3.25) shows the light ray traveling from the two different places, with on-axis in light red and off-axis in dark red. These two rays hit the

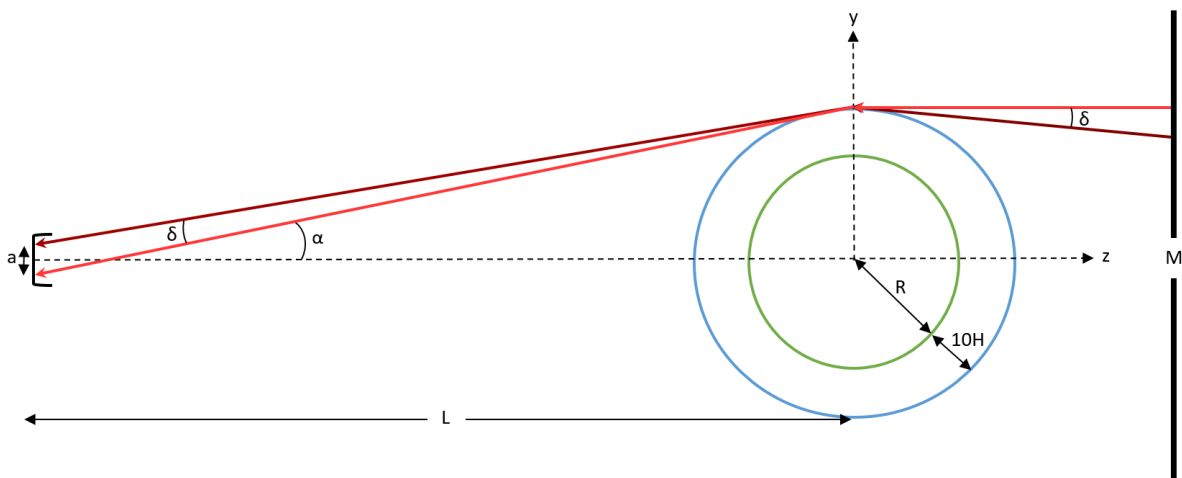


Figure 3.25: Our Terrascope set-up showing the relationship between aperture, a , and pixel size, $\frac{z\alpha_{\text{peak}}}{M}$, through the angle δ . Green and blue circles show the Earth's surface and atmosphere, respectively. Light red and dark red lines show on- and off- axis light rays, respectively. By drawing how the light shifts by δ on each side, we can calculate how the size of the detector and the size of a resolved pixel are related. From this, we estimate an effective aperture size of our Terrascope.

detector at a different location in space (along the y -axis), but each is in the same location relative to the many other light rays emitted from the celestial object. The whole front of light is shifted by the same distance. We call this distance— between where the on- and off- axis light rays hit the detector— the aperture, a . It is the length over which light is gathered to create an image of the object. The on- and off- axis rays each create a distinct image, which we can

call resolved. A concept called angular resolution can be described as the minimum angle possible between two distinct incoming sources traveling through an opening such that the sources can be distinguished as separate [5]. The opening here is the part of the atmosphere through which the rays pass. We call the angle between where the rays hit δ . On the other side of our Terrascope and Figure (3.25) is the grid of size M in which we are collecting these light rays. Each bin is a pixel wide and denotes the smallest distance over which light rays can be resolved. In a way, it too is the minimum required separation of two light sources in order for them to be perceived as distinguishable. The angle opening onto this pixel can then also be seen as δ . We can relate the aperture size to pixel size through this variable. On the detector side, we use the small angle approximation to define it as:

$$\delta = \frac{a}{L} \quad (3.54)$$

On the grid side, we define it as the angular range of the PSF divided by the number of bins:

$$\delta = \frac{2\alpha_{\text{peak}}}{M} \quad (3.55)$$

$2\alpha_{\text{peak}}$ is the angle from one side of the grid to the other, from $\frac{-10H}{L}$ to $\frac{10H}{L}$. It was originally from $\frac{-(R+10H)}{L}$ to $\frac{R+10H}{L}$, but we chose to focus on the small center part of the grid where the most light is, which we called the "peak". We set Equations (3.54) and (3.55) for δ equal to each other, plug in the chosen value for α_{peak} , and solve for a :

$$\frac{a}{L} = \frac{2\alpha_{\text{peak}}}{M} \quad (3.56)$$

$$a = \frac{2\alpha_{\text{peak}}L}{M}$$

$$a = \frac{2\left(\frac{10H}{L}\right)L}{M}$$

$$a = \frac{20H}{M} \quad (3.57)$$

This is our equation for effective aperture. Note that the equation depends on M which we can change, but changing M also changes the resulting amplification of our PSF proportionally. Now, if we plug in $M = 100$ (which we will use in the next section), we can calculate our effective aperture:

$$a = \frac{20H}{M} = \frac{20(8.5 \times 10^3)}{100} = 1.7 \times 10^3 \text{m} \quad (3.58)$$

From this, we conclude that using a grid size of $M = 100$ translates to an effective detector aperture of 1,700m or 1.7km. When Kipping used his Equation (3.53) with $a = 1$, he calculated an amplification of 55,000 (omitting the extinction for now). To see how our results compare

to those of Kipping, we will use Equation (3.53) the same equation for our $a = 1.7 \times 10^3$:

$$A \sim \frac{8H\epsilon}{a} \sim \frac{8(8.5 \times 10^3)}{(1.7 \times 10^3)} \sim 40 \quad (3.59)$$

So, when extinction effects are omitted, Kipping's amplification equation predicts that an aperture of 1,700m (or, in pixel terms, $M = 100$) will yield an amplification of 40. We turn to our PSF results in the next section to see if our simulation is close to Kipping's prediction.

3.6.3. Results

In this section, we have chosen $L = 1.5 \times 10^9$ m (the Hill radius) because it leads to the least amount of turbulence of all the L values we tested. First we show two 2D PSFs: (1) $\lambda = 1000$ nm, which is the best suited for use in our Terrascope and (2) $\lambda = 600$ nm, which shows interesting absorption behavior. Then we show 1D PSFs for all nine wavelengths in our simulation. Each PSF has eight subfigures including the three atmospheric effects, plus one without any effects. The 2D PSFs are what the celestial object would look like as a reconstructed image; the 1D PSFs measure the amplification behavior and compare the different wavelengths. Finally, Table (3.3) contains the numerical values shown in the 1D PSFs. With eight rows and nine columns, it lists the peak amplification value for all three effects for each wavelength. All figures and the table use $N = 10^6$ and $M = 100$.

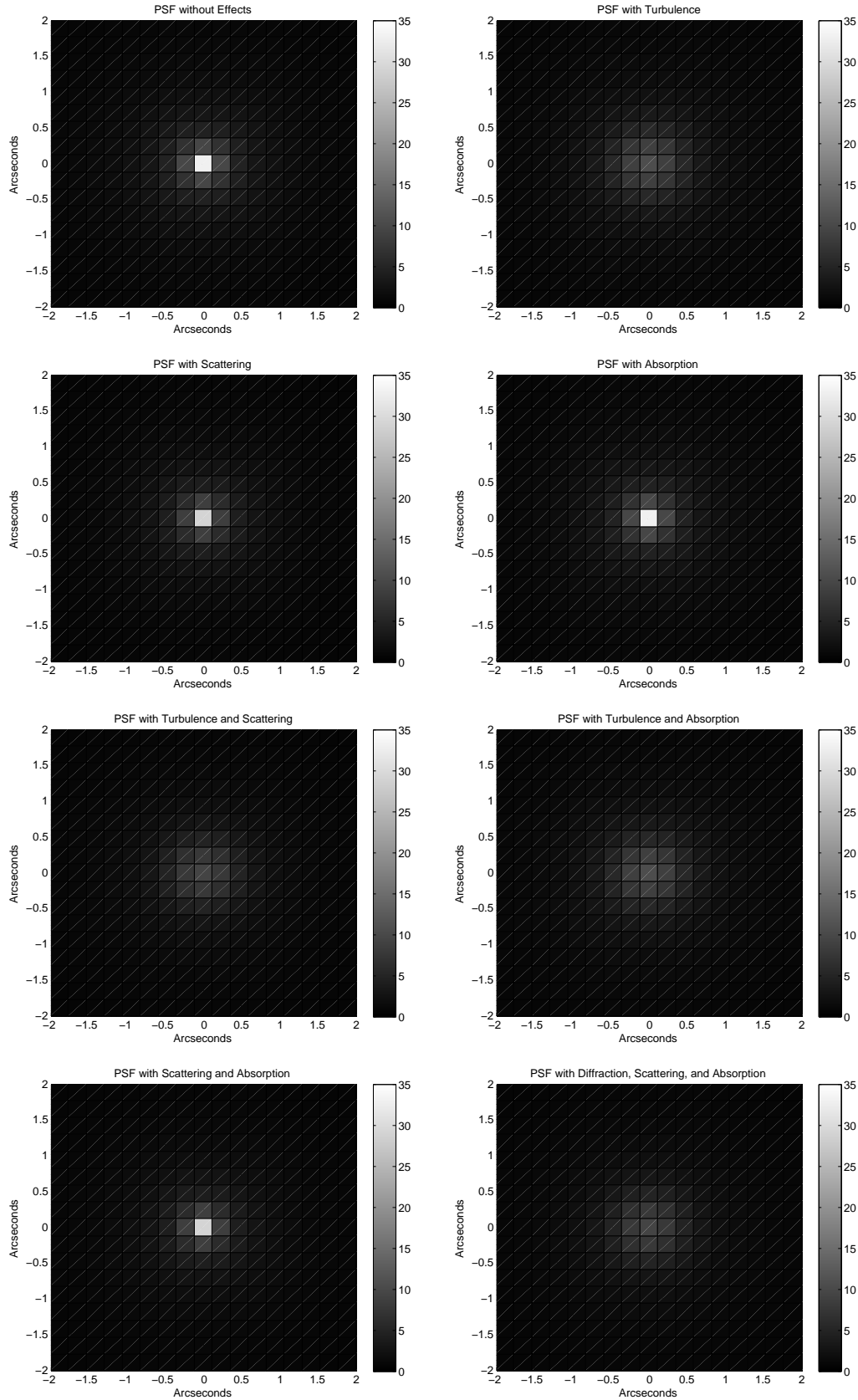


Figure 3.26: Eight different combinations of effects showing their influence on the PSF for $\lambda = 10^{-6}m = 1000nm$. Of all the wavelengths we tested in our simulations, 1000nm has the highest probability of survival and longest coherence length; hence, it is expected to also have the highest amplification after the light is subjected to all three atmospheric effects. Without effects, the amplification is approximately 35; with all affects, the amplification is approximately 10.

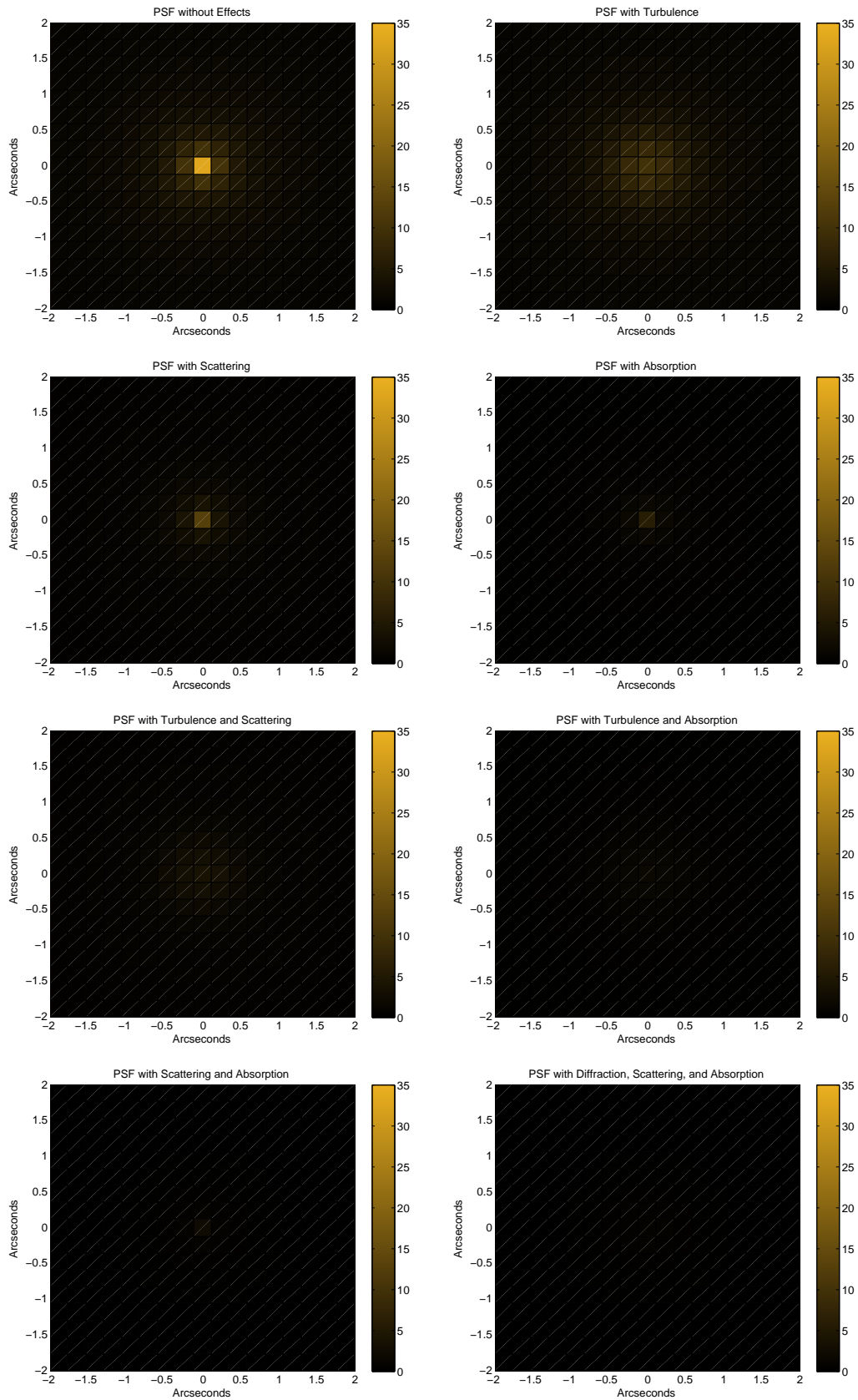


Figure 3.27: Eight different combinations of effects showing their influence on the PSF for $\lambda = 6 \times 10^{-7} \text{m} = 600 \text{nm}$. Of note in these plots is that the amplification after scattering is higher than the amplification after absorption. This was predicted by the survival probability plots in which 600nm light had a higher chance of survival after scattering than absorption (for $L = 1.5 \times 10^9 \text{m}$). Similar to the plots of 1000nm, when 600nm light is subjected to none of the effects, the amplification is 30. However, unlike the 1000nm plots, when 600nm light is subjected to all three effects, the amplification is effectively zero.

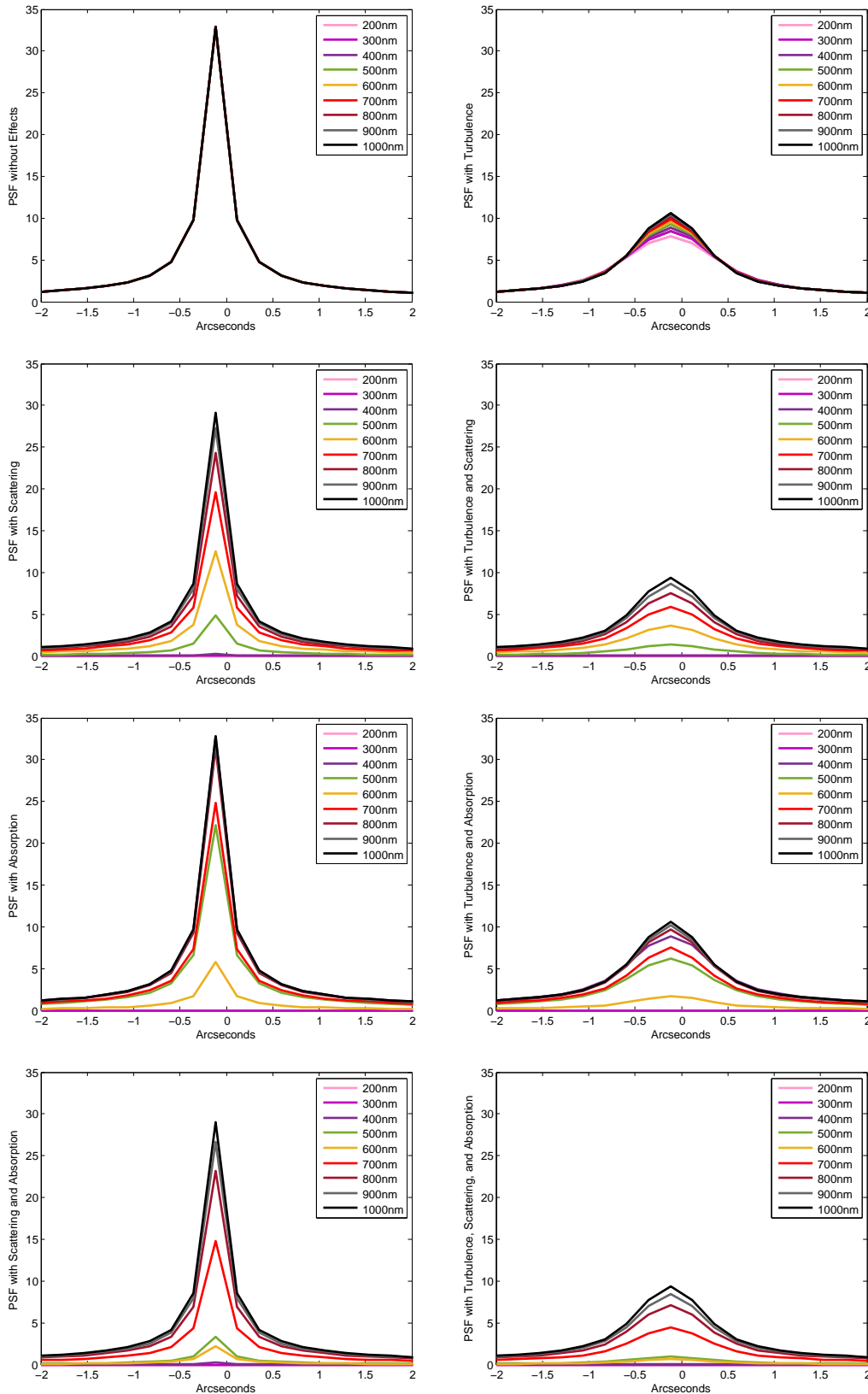
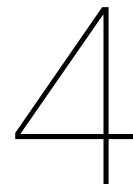


Figure 3.28: These are plots of the PSF for different combinations of effects for varying wavelengths. On the left are the PSFs without turbulence; on the right are those with turbulence. Note how on the right, the peaks are both much lower and wider. The widening effect is due to light being spread out. This spread also causes a lower peak height. Turbulence causes the greatest decrease in intensity, followed by scattering and then absorption. For scattering and absorption, this change in intensity depends heavily on the wavelength, but for turbulence, it does not.

Effect(s)	Wavelength (nm)									
	200	300	400	500	600	700	800	900	1000	
None	32.87	32.87	32.87	32.87	32.87	32.87	32.87	32.87	32.87	32.87
Turb	7.83	8.40	8.87	9.27	9.60	9.90	10.15	10.38	10.59	
Scatt	6.51×10^{-33}	4.23×10^{-6}	0.28	4.88	12.54	19.61	24.32	27.25	29.07	
Absorb	3.37×10^{-124}	2.51×10^{-52}	32.77	22.12	5.75	24.86	31.33	32.21	32.81	
Turb+Scatt	1.55×10^{-33}	1.08×10^{-6}	0.08	1.38	3.66	5.91	7.51	8.61	9.37	
Turb+Absorb	8.05×10^{-124}	6.41×10^{-53}	8.84	6.24	1.68	7.49	9.68	10.17	10.58	
Scatt+Absorb	6.69×10^{-158}	3.23×10^{-59}	0.28	3.28	2.19	14.83	23.18	26.70	29.02	
All	1.59×10^{-158}	8.25×10^{-60}	0.08	0.93	0.64	4.47	7.16	8.43	9.35	

Table 3.3: Peak PSF amplification for all combinations of effects, by wavelength. For $N = 10^6$, $M = 100$, $L = 1.5 \times 10^9$ m.

Our simulations showed that the highest amplification without any effects is around 35. Equation (3.59) determined that Kipping's calculations for our data predict an amplification of 40. This is close enough to say that our results are consistent with Kipping's and we can therefore use his estimates for amplification before extinction. However, we still have to take into account the extinction due to our atmospheric effects. The final estimate for our Terrascope amplification must include these effects. In the next chapter, we discuss these final estimates, how our process and results compare to Kipping's work, and examine the possible flaws and missing parts to our work.



Discussion

4.1. Amplification

At the conclusion of his work, Kipping shows that for an ideal, quiet atmosphere, when using a 1 meter wide detector, $\lambda = 1000\text{nm}$, and $L = 1.5 \times 10^9\text{m}$ (the Hill radius), his Terrascope configuration makes the light of a celestial object to 55,000 times as bright as it would normally appear from Earth. In the previous chapter, we calculated Kipping's amplification had he used our effective aperture, and it was on par with our PSF amplification. If our PSF amplification is similar to Kipping's, then we estimate that our celestial object amplification is also similar. We conclude that our Terrascope yields an amplification of 55,000. However, this is without turbulence or extinction due to scattering and absorption. Figure (3.28) shows that the PSF amplification without any effects is 35; with extinction effects, it is about 30. If we scale down our Terrascope amplification by the same amount, we arrive at a 47,300. Now we want to take turbulence into account. However, when including turbulence, our previous equation for calculating amplification (Equation (3.53)) is no longer valid. This is because when turbulence is included, we do not have ideal ray tracing. The turbulence causes the light rays to spread out, a spread which we model according to a 2D Gaussian. The detector is only a small part of this larger range where light rays end up. This causes rays to miss the detector, so the manner in which Equation (3.53) uses the aperture to calculate amplification is not suitable in the turbulent regime. For an estimate of amplification including turbulence, we use our PSF results. When varying the number of rays (N) and the number of bins (M), the amplification with turbulence stayed at a constant value of 10. Thus, our on-axis amplification estimate for our Terrascope with a detector aperture of 1m, at $L = 1.5 \times 10^9\text{m}$, observing $\lambda = 1000\text{nm}$ wavelength light has an amplification of 10 when including turbulence. When we also include Rayleigh scattering and ozone absorption, this amplification further decreases to 8.6.

4.2. Comparison to Kipping's Work

Our work and Kipping's agree on the effect of extinction (scattering and absorption). We show that it depletes the light by 14%; Kipping shows that it depletes by 20%. Most of his research is in the infrared, where there is less extinction. However, we both test 1000nm light, which he shows has the same amplification values as longer wavelengths. To model scattering and absorption, Kipping used a transmittance and radiance package (lowtran7) while we used specific scattering and absorption data. Both provide a suitable rough estimate of the effects. The explanation for our large difference in amplification depletion is that Kipping's model does not account for turbulence effects. As our results of Chapter 3 show, when compared to turbulence, scattering and absorption are minimal effects on the PSF and resulting amplification. Turbulence spreads out the light (the peak width in our PSFs), causing a decrease in the amplification intensity (the peak height). In addition to the spread causing a loss of light, it also results in the image being blurred.

Another difference in amplification is that Kipping suggests that for certain off-axis positions, the amplification is larger than for the on-axis situation. This is due to the shape of the thin light ring. When off-axis, it becomes more ovalar, and there is more light received by the detector. Our results do not match that finding. Instead, we find that off-axis light is amplified less than on-axis light, and the intensity falls off according to the following equation:

$$A \sim \frac{2H}{L\alpha} \quad (4.1)$$

Our finding actually agrees with that of the research conducted by W.B. Hubbard during the occultation of a star by Mars. Inspired by the observation of a bright central spot due to Mars' atmospheric lensing, Hubbard calculated the theoretical amplification of an apparatus similar to the Terrascope. He concluded that there would be a "sharp central peak [with] broad wings which fall off" according to Equation (4.1) [25]. Hubbard also noted that actual amplification would differ from the calculated ideal due to a turbulent atmosphere.

Although the amplification results differ, many of our Terrascope findings agree with those of Kipping. Both investigations found a proportional relationship between the minimum altitude a light ray travels into the atmosphere and the distance between the Earth and the detector. Our model indicates that for best case results, we should increase these two as much as is feasible. We agree that the best wavelengths to use are in the infrared because that light is much less hindered by absorption and scattering in the Earth's atmosphere than optical light.

4.3. Errors

In this discussion of our results and comparison to Kipping's work, we have not yet considered shortcomings and possible mistakes in our Terrascope. We believe the following should be given attention:

- When using the Thin Ring code, not hitting the targeted ring shape exactly can be the difference between no collected light rays and the PSFs seen in Chapter 3. The necessary precision is on the order of a hundred-thousandth of a radian.
- We adjust the PSF after our calculations so that our results should not depend on the bin size. However, the extremely small precision means that adjusting the N and M values can change the outcome, and then our results are not independent of ray count and bin size.
- The extra points in Figures (3.10) and (3.22) are numerical round off errors due to cutting off the atmosphere at $10H$.
- Our strategies when cross-section data was not available could have lead to errors. For scattering, we estimated wavelengths outside the given ranges, seen as a broken line in Figure (3.9). For absorption, we had to interpolate between temperature values.
- Our amplification estimate is not thorough enough and requires a more rigorous calculation.

5

Conclusion

5.1. Research Answers

We now restate the research questions and endeavor to answer them based on the research covered in this report:

- Can the Terrascope be a useful telescope, and if so, to what extent?
 - What kind of numerical model is suitable for studying the Terrascope?
 - What physical effects will diminish the quality of the Terrascope?

In Chapter 2, we described our Terrascope model which uses ray tracing and gradient-index optics. Tracing each ray was effective for viewing its path through the atmosphere and enacting individual effects on it. Gradient-index optics was used to describe the way that light interacts in the atmosphere via the refractive index. All codes used these fundamentals, but we varied the type of code by changing the shape of the angle array. Each type was suited for certain simulations, for example, generating an accurate PSF is best done using the Thin Ring code. All codes were spherically symmetric for simplicity. They could be made non-spherically symmetric by adding variable atmospheric effect profiles, without computational cost. It is useful to have a model which examines different wavelengths and distances to the detector, because these will influence the results.

In Chapter 3, we tested the consequences of three different atmospheric effects on our Terrascope. It appears that they adversely effect the Terrascope's performance from most to least in the following order: turbulence, Rayleigh scattering, and ozone absorption. Turbulence spreads out the image, thereby reducing the amplification by 99.98%. Rayleigh scattering has the largest consequences for shorter wavelengths. Ozone absorption has the largest consequences for rays which pass through the ozone layer at 15-35km. Unfortunately, this height range corresponds to L values all beyond 1.5×10^9 m (Hill radius).

In Chapter 4, we combined our findings to address the overall question of the Terrascope's feasibility. We measured this in terms of the final amplification of light that the Terrascope provides, while keeping in mind that angular resolution (image sharpness) is another important parameter for astronomical observation.

Here we state that despite the decrease in amplification mainly caused by turbulence, the Terrascope could prove useful and is definitely an interesting concept for additional study. Experimenting with different L values, longer wavelengths, and other planetary (or lunar) atmospheres may be particularly fruitful. We must keep in mind that our calculated amplification is only valid when an object is on-axis. When it is off-axis, meaning that celestial object does not pass directly through the z -axis, the amplification falls off according to Equation (4.1). Additionally, the turbulence will severely hinder the sharpness of the image. In terms of the practicality of the Terrascope, the following issue must be seriously considered. The Terrascope has all the problems of both a ground- and space- based telescope combined. For the former, the Earth's atmosphere must be accounted for in calculations. Local weather effects and global climate will effect the atmosphere and therefore the light passing through into the Terrascope detector. For the latter, the cost increases because the detector must be launched into space. Once in position, it must face the Earth while blocking out direct and reflected light from the Sun. As Kipping mentions, the Terrascope is also bound to observing the objects that happen to pass behind the Earth, rather than purposefully aiming at a target. In the next section, we propose types of research for which the Terrascope would be useful.

5.2. Astronomical Uses

We propose astronomical research that requires highly amplified, long wavelength, and possibly low angular resolution light. In addition, because of the short time scale during which observing targets pass behind Earth (on the scale of days or weeks for reasonably close L values), we cannot choose objects that must be observed for long periods of time, such as the cycles of orbiting exoplanets. The following research focuses may be suitable:

- Low temperature objects, such as red dwarf stars and brown dwarfs
- Objects at high redshift
- Objects very distant in space and time
- Look through dust at newborn stars
- Look through dust at galaxies
- First identification of exoplanets based on infrared signature due to planet's thermal radiation
- Microwave sources (such as the cosmic microwave background)
- Radio quasars (active galactic nuclei)
- Radio galaxies
- Studying Earth's atmosphere

5.3. Future Work

Our Terrascope set forth in this work is only a second step after Kipping's research. There are many ways in which we can, and hope, to improve upon the model. This includes:

- Different refractive index function, $n(\mathbf{r})$
- Different C_n^2 profiles for different places and times
- Additional types of scattering (Mie, inelastic)
- Additional molecules for scattering and absorption
- Wider wavelength range (especially 1000nm and above)
- Use the atmosphere of other planets or moons (for example, Titan)
- Expand research to include work of Hubbard, Elliot, and others who wrote about the "bright central spot" or "central flash" during their studies of occultations
- Additional effects:
 - Oblateness of the Earth (Earth is not a perfect sphere) due to rotation
 - Sunlight shining behind the Earth for half of the observing time, necessitating an occulting disk on the detector (Kipping's theory and our rudimentary models show that it cuts the light in half)
 - Sunlight bouncing off the Earth and into the detector
 - City lights emanating from the Earth and going into the detector
 - Airglow, which is light absorbed by the Earth's atmosphere during the day and released hours later at night, during the time the detector would be collecting [11]

If more advanced Terrascope simulations show that it is useful, then we could proceed with research into construction and launching.

Bibliography

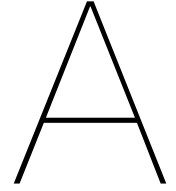
- [1] Sean M. Andrews, Jane Huang, Laura M. Pérez, Andrea Isella, Cornelis P. Dullemond, Nicolás T. Kurtovic, Viviana V. Guzmán, John M. Carpenter, David J. Wilner, Shangjia Zhang, Zhaohuan Zhu, Tilman Birnstiel, Xue-Ning Bai, Myriam Benisty, A. Meredith Hughes, Karin I. Öberg, and Luca Ricci. The disk substructures at high angular resolution project (DSHARP). I. motivation, sample, calibration, and overview. *The Astrophysical Journal*, 869(2):L41, Dec 2018. doi: 10.3847/2041-8213/aaf741. URL <https://doi.org/10.3847>.
- [2] Robert R. Beland. Propagation through atmospheric turbulence. In Fred G. Smith, Joseph S. Accetta, and David L. Shumaker, editors, *The Infrared & Electro-Optical Systems Handbook: Vol 2. Atmospheric Propagation of Radiation*, chapter 3, pages 157–232. Infrared Information Analysis Center and SPIE Optical Engineering Press, 1993.
- [3] C. Bohren and D. Huffman. *Absorption and Scattering of Light by Small Particles*. WILEY-VCH Verlag GmbH & Co. KGaA, Weinheim, 1 edition, 1983. ISBN 978-0-471 -29340-8.
- [4] Nadine Borduas and Neil M. Donahue. Chapter 3.1 - the natural atmosphere. In Béla Török and Timothy Dransfield, editors, *Green Chemistry*, pages 131 – 150. Elsevier, 2018. ISBN 978-0-12-809270-5. doi: <https://doi.org/10.1016/B978-0-12-809270-5.00006-6>. URL <http://www.sciencedirect.com/science/article/pii/B9780128092705000066>.
- [5] Max Born and Emil Wolf. *Principles of optics: electromagnetic theory of propagation, interference and diffraction of light*. Elsevier, 2013.
- [6] O. Boucher, D. Randall, P. Artaxo, C. Bretherton, G. Feingold, P. Forster, V.-M. Kerminen, Y. Kondo, H. Liao, U. Lohmann, P. Rasch, S.K. Satheesh, S. Sherwood, B. Stevens, and X.Y. Zhang. Clouds and aerosols. Technical report, Intergovernmental Panel on Climate Change, Cambridge, United Kingdom and New York, NY, USA, 2013.
- [7] Robert Boyle. New experiments physico-mechanical, touching the air: Whereunto is added a defence of the authors explication of the experiments, against the obiections of franciscus linus and thomas hobbes. *Oxford*, 1662.
- [8] Michele Brunetti and F. Prodi. The climate system. *EPJ Web of Conferences*, 98:02001, 01 2015. doi: 10.1051/epjconf/20159802001.
- [9] Anthony Bucholtz. Rayleigh-scattering calculations for the terrestrial atmosphere. *Applied Optics*, 34(15):2765–2773, May 1995. doi: 10.1364/AO.34.002765. URL <http://ao.osa.org/abstract.cfm?URI=ao-34-15-2765>.

- [10] Luis Caffarelli and E. Weinan. *Hyperbolic equations and frequency interactions*, volume 5. American Mathematical Society, Institute for Advanced Study, Providence, Rhode Island, 1 edition, 1999. ISBN 0821805924. Lecture notes from a summer program held in Park City, Utah, July 9-29, 1995.
- [11] L. L. Christensen, S. Noll, and P. Horálek. Light Phenomena over the ESO Observatories I: Airglow. *The Messenger*, 163:40–42, Mar 2016. URL <https://ui.adsabs.harvard.edu/abs/2016Msngr.163...40C>.
- [12] C. E. Coulman. Fundamental and applied aspects of astronomical “seeing”. *Annual Review of Astronomy and Astrophysics*, 23:19–57, September 1985. doi: <https://doi.org/10.1146/annurev.aa.23.090185.000315>.
- [13] Roy van Boekel C.P. Dullemond and Andreas Quirrenbach. Atmospheric turbulence: “seeing”, 2010. URL http://www.ita.uni-heidelberg.de/~dullemond/lectures/obsastro_2010/Chapter_Turbulence.pdf. Lecture for Observational Astronomy course at Ruprecht-Karls-Universität Heidelberg.
- [14] J. Elliot, Richard French, E. Dunham, Peter Gierasch, J. Veverka, C. Church, and C. Sagan. Occultation of epsilon geminorum by mars. ii - the structure and extinction of the martian upper atmosphere. *Astrophys. J.*, 217, November 1977. doi: 10.1086/155612.
- [15] James E. Faller and E. Joseph Wampler. The lunar laser reflector. *Scientific American*, 222(3):38–49, 1970. ISSN 00368733, 19467087. URL <http://www.jstor.org/stable/24925752>.
- [16] Richard Feynman. The Feynman lectures on physics, volume i chapter 27: Geometrical optics, 1961.
- [17] Richard Feynman. The Feynman lectures on physics, volume i chapter 26: Optics: The principle of least time, 1961.
- [18] D. Frenkel and B. Smit. *Understanding Molecular Simulation: From Algorithms to Applications*. Academic Press, 2001. ISBN 978-0-12-267351-1. doi: 10.1016/B978-0-12-267351-1.X5000-7. URL <http://www.jstor.org/stable/j.ctt7t8hg>.
- [19] Uriel Frisch. *Turbulence: The Legacy of A.N. Kolmogorov*. Cambridge University Press, 11 1995. ISBN 978-0521457132. doi: 10.1017/CBO9781139170666.
- [20] George E. Hale. The Yerkes observatory of the university of Chicago. IV. the forty-inch telescope, dome, and rising floor. *The Astrophysical Journal*, 6:37–46, June 1897. doi: 10.1086/140369.
- [21] William M Haynes. *CRC handbook of chemistry and physics*. CRC press, 2014.

- [22] Albert Van Helden. The invention of the telescope. *Transactions of the American Philosophical Society*, 67(4):1–67, 1977. ISSN 00659746. URL <http://www.jstor.org/stable/1006276>.
- [23] Sir John Frederick William Herschel. *The Telescope*. Adam and Charles Black, 1861.
- [24] J. Michael Hollas. *Modern Spectroscopy*. John Wiley & Sons Ltd., 1 edition, 1987. ISBN 0 470 84416 7.
- [25] W. B. Hubbard. Wave optics of the central spot in planetary occultations. *Nature*, 268 (5615):34–35, December 1977. ISSN 0028-0836. doi: 10.1038/268034a0.
- [26] Hendrik Christoffel Hulst and Hendrik C van de Hulst. *Light scattering by small particles*. Courier Corporation, 1981.
- [27] Andrea Isella, Greta Guidi, Leonardo Testi, Shangfei Liu, Hui Li, Shengtai Li, Erik Weaver, Yann Boehler, John M. Carperter, Itziar De Gregorio-Monsalvo, Carlo F. Manara, Antonella Natta, Laura M. Pérez, Luca Ricci, Anneila Sargent, Marco Tazzari, and Neal Turner. Ringed structures of the hd 163296 protoplanetary disk revealed by alma. *Phys. Rev. Lett.*, 117:251101, Dec 2016. doi: 10.1103/PhysRevLett.117.251101. URL <https://link.aps.org/doi/10.1103/PhysRevLett.117.251101>.
- [28] David Kipping. The “terrascope”: On the possibility of using the earth as an atmospheric lens. *Publications of the Astronomical Society of the Pacific*, 131(1005):114503, Oct 2019. doi: 10.1088/1538-3873/ab33c0. URL <https://doi.org/10.1088%2F1538-3873%2Fab33c0>.
- [29] V. Lakshminarayanan, A. Ghatak, and K Thyagarajan. *Lagrangian Optics*. Springer, 2002. ISBN 978-0-7923-7582-1. doi: 10.1007/978-1-4615-1711-5.
- [30] D. Lamb. Cloud types ii, 2004. URL <https://personal.ems.psu.edu/~lno/Meteo437/Cldtyps2.jpg>. Figure from Lecture for Physics and Chemistry of Clouds course at Penn State College.
- [31] A level physics tutor. A-level physics tutor: Optics, telescopes, 2016. URL <https://www.a-levelphysics tutor.com/optics-telescopes.php>.
- [32] A. I. Mahan. Astronomical refraction—some history and theories. *Applied Optics*, 1 (4):497–511, Jul 1962. doi: 10.1364/AO.1.000497. URL <http://ao.osa.org/abstract.cfm?URI=ao-1-4-497>.
- [33] Erich W. Marchand. Ray tracing in gradient-index media. *Journal of the Optical Society of America*, 60(1):1–7, Jan 1970. doi: 10.1364/JOSA.60.000001. URL <http://www.osapublishing.org/abstract.cfm?URI=josa-60-1-1>.
- [34] S. S. R. Murty. Laser beam propagation in atmospheric turbulence. *Proceedings of the Indian Academy of Sciences Section C: Engineering Sciences*, 2(1):179–195, 1979. doi: <https://doi.org/10.1007/BF02845031>.

- [35] J. B. Pors. *Entangling light in high dimensions*. PhD thesis, Leiden University, 2011.
- [36] Andreas Quirrenbach. The effects of atmospheric turbulence on astronomical observations, 2004. URL http://cfao.ucolick.org/aosummer/book/pdf/3.1_quirrenbach.pdf. Center for Adaptive Optics: IV Adaptive Optics for Astronomy.
- [37] F. Roddier. The effects of atmospheric turbulence in optical astronomy. *Progress in Optics*, 19:281–376, Jan 1981. doi: 10.1016/S0079-6638(08)70204-X.
- [38] Kshudiram Saha. *The Earth's Atmosphere: Its Physics and Dynamics*. Springer-Verlag Berlin Heidelberg, 1 edition, 2008. ISBN 978-3-540-78427-2.
- [39] A. Serdyuchenko, V. Gorshelev, M. Weber, W. Chehade, and J. P. Burrows. High spectral resolution ozone absorption cross-sections –; part 2: Temperature dependence. *Atmospheric Measurement Techniques*, 7(2):625–636, 2014. doi: 10.5194/amt-7-625-2014. URL <https://amt.copernicus.org/articles/7/625/2014/>.
- [40] Maarten Snee and Wim Ubachs. Direct measurement of the rayleigh scattering cross section in various gases. *Journal of Quantitative Spectroscopy and Radiative Transfer*, 92(3):293–310, May 2005. doi: 10.1016/j.jqsrt.2004.07.025.
- [41] H. Tennekes and John Lumley. *A First Course in Turbulence*. The MIT Press, 1972. ISBN 978-0262200196.
- [42] Ugot Tricoli. *Electromagnetic scattering with the GDT-matrix method: an application to irregular ice particles in cirrus*. PhD thesis, Universität Heidelberg, Jan 2015.
- [43] S. G. Turyshv and B-G. Andersson. The 550-au mission: a critical discussion. *Monthly Notices of the Royal Astronomical Society*, 341(2):577–582, May 2003. ISSN 1365-2966. doi: 10.1046/j.1365-8711.2003.06428.x. URL <http://dx.doi.org/10.1046/j.1365-8711.2003.06428.x>.
- [44] Humboldt State University. Introduction to remote sensing: Atmospheric absorption & transmission, 2019. URL http://gsp.humboldt.edu/OLM/Courses/GSP_216_Online/lesson2-1/atmosphere.html.
- [45] Gerard Theodore van Belle, Aden Baker Meinel, and Marjorie Pettit Meinel. The scaling relationship between telescope cost and aperture size for very large telescopes. In Jacobus M. Oschmann Jr., editor, *Ground-based Telescopes*, volume 5489, pages 563 – 570. International Society for Optics and Photonics, SPIE, 2004. doi: 10.1117/12.552181. URL <https://doi.org/10.1117/12.552181>.
- [46] M. Verhaegen, R. Franje, C. Keller, and N. Doelman. Fast and high performance adaptive optics for the e-elt, 2001. URL <https://www.dcsc.tudelft.nl/~mverhaegen/n4ci/esfri.htm>. Description for a PhD/PostDoc vacancy.

- [47] M.O. Vieitez, T.I. Ivanov, W.M.G. Ubachs, B.R. Lewis, and C.A. de Lange. On the complexity of the absorption spectrum of molecular nitrogen. *Journal of Molecular Liquids*, 141:110–117, 2008. ISSN 0167-7322. doi: 10.1016/j.molliq.2008.01.014.
- [48] P. M. Visser, S. E. Alpert, and D. M. Stam. On the optical seeing of the terrascope. forthcoming, 2020.
- [49] N.V. Vitanov, B.W. Shore, L. Yatsenko, K. Böhmer, T. Halfmann, T. Rickes, and K. Bergmann. Power broadening revisited: theory and experiment. *Optics Communications*, 199(1):117 – 126, 2001. ISSN 0030-4018. doi: [https://doi.org/10.1016/S0030-4018\(01\)01495-X](https://doi.org/10.1016/S0030-4018(01)01495-X). URL <http://www.sciencedirect.com/science/article/pii/S003040180101495X>.
- [50] Wilson Wall. *A History of Optical Telescopes in Astronomy*. Springer, Gewerbestrasse 11, 6330 Cham, Switzerland, 1 edition, 2018. ISBN 978-3-319-99087-3.
- [51] Andrew T. Young. San Diego state university: Atmospheric refraction, astronomical refraction, 2012. URL https://aty.sdsu.edu/explain/atmos_refr/astr_refr.html.
- [52] Andrew T. Young. San Diego state university: Atmospheric refraction, cassini's model, 2012. URL https://aty.sdsu.edu/explain/atmos_refr/models/Cassini.html.



Appendix

Here we derive an analytical formula for the minimum height, h_0 and use it to graph its relationship to the detector distance, L [48].

To determine h_0 , we bend an incoming on-axis light ray towards the detector. We do this by setting the starting angle equal to the bending angle. Recall, the ray which enters the detector is considered the starting ray because we model our Terrascope the opposite of the physical scenario. The starting angle is:

$$\alpha_{\text{start}} = \frac{R + h_0}{L} \quad (\text{A.1})$$

The bending angle is:

$$\Delta\alpha(h) = 2\eta_0 \frac{R + h}{H} e^{R/H} K_0 \left(\frac{R + h}{H} \right) \quad (\text{A.2})$$

Where K_0 is the modified Bessel function of the second kind. Setting Equations (A.1) and (A.2) equal and solving for h_0 , we arrive at:

$$h_0 = \frac{H}{2} \left(1 - \frac{H}{2R} \right) \log \frac{2\pi\eta_0^2 L^2}{RH} - \frac{9H^2}{8R} + (\sqrt{2} - 1) \sqrt{\frac{HR}{2\pi} \frac{R}{L}} \quad (\text{A.3})$$

We graph the relationship between h_0 and L in Figures (A.1) and (A.2). The first is the range of values of L used in this research, from $L = 3.844 \times 10^8$ (the distance from Earth to Moon), to $L = 1.5 \times 10^9$ (the Hill radius). The highest minimum height reached for this range is just below 14km. In order for a ray of light to barely skim below the atmosphere for a minimum height of 90km, we look at the second plot. This shows that the corresponding L value is approximately 10^{13} m. For comparison, this is double the distance from Earth to Pluto.

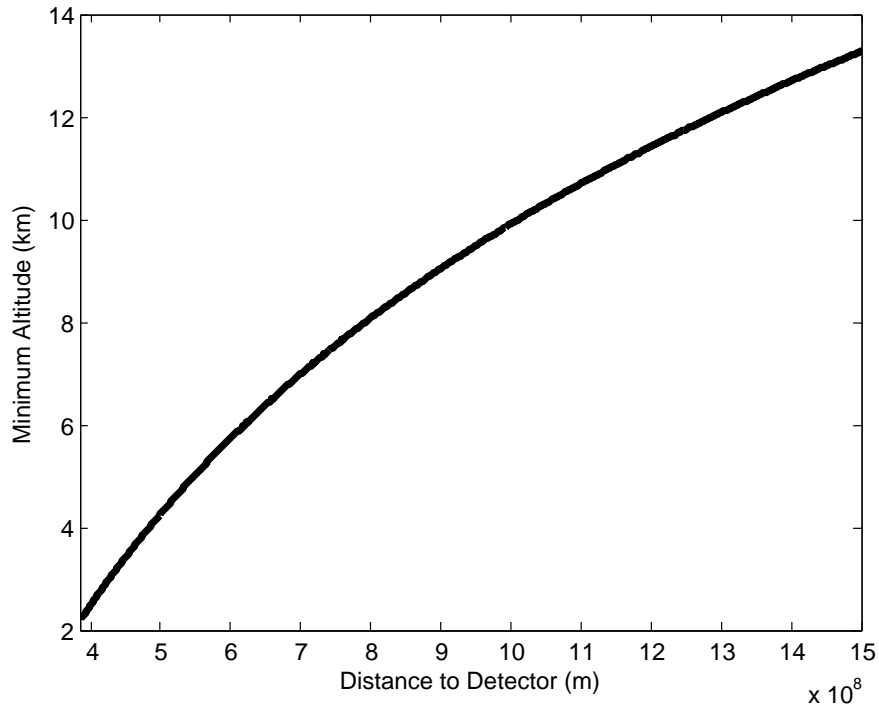


Figure A.1: Graph of minimum height that a light ray travels versus the L value of that light ray. This range is the one used for all of the simulations in our research. As shown and referenced throughout this report, there is a proportional relationship between the two variables, but it is not linear.

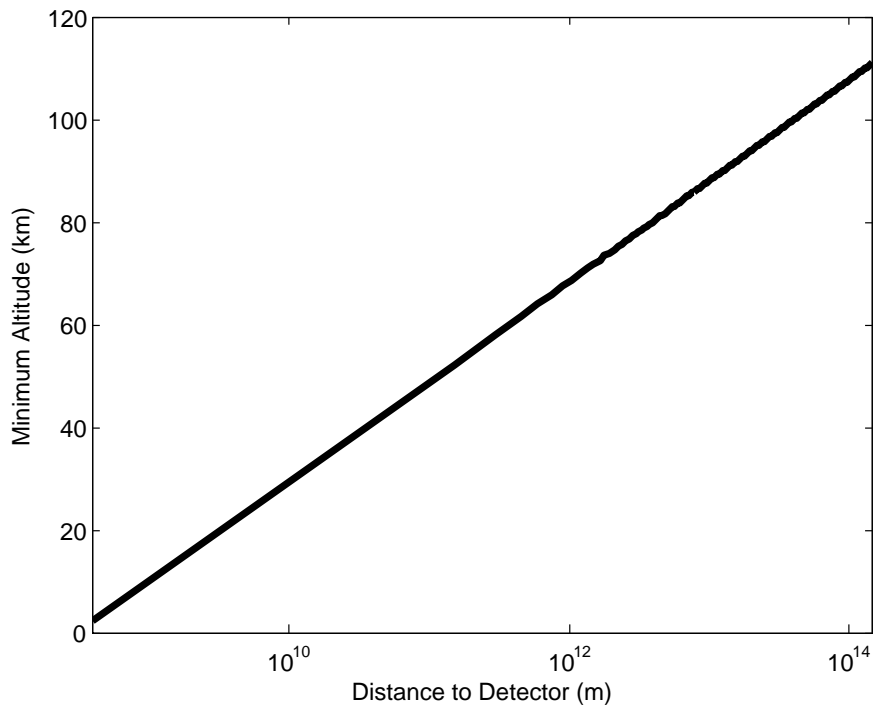


Figure A.2: Graph of minimum height that a light ray travels versus the L value of that light ray, shown for a \log_{10} x -axis. The linear trend of this graph shows that there is a semi-log relationship between the variables h_0 and L . To reach higher values of h_0 takes much larger values of L . For example, rays with $h_0 = 80\text{km}$ correspond to $L = 10^{12}$ while rays with $h_0 = 90\text{km}$ correspond to $L = 10^{13}$.